DESIGN AND CONSTRUCTION OF AN INTERFEROMETRIC SETUP FOR DYNAMIC MEASUREMENT OF CLEARANCES INSIDE PLAIN BEARINGS

A THESIS SUBMITTED TO
THE GRADUATE SCHOOL OF NATURAL AND APPLIED SCIENCES
OF
MIDDLE EAST TECHNICAL UNIVERSITY

BY

ATAE JAFARI-TABRIZI

IN PARTIAL FULFILLMENT OF THE REQUIREMENTS
FOR
THE DEGREE OF MASTER OF SCIENCE
IN
MECHANICAL ENGINEERING

DECEMBER 2017

Approval of the thesis:

DESIGN AND CONSTRUCTION OF AN INTERFEROMETRIC SETUP FOR DYNAMIC MEASUREMENT OF CLEARANCES INSIDE PLAIN BEARINGS

submitted by **ATAE JAFARI-TABRIZI** in partial fulfillment of the requirements for the degree of **Master of Science in Mechanical Engineering Department, Middle East Technical University** by,

Prof. Dr. Gülbin Dural Ünver ______________
Dean, Graduate School of **Natural and Applied Sciences**

Prof. Dr. M. A. Sahir Arıkan ______________
Head of Department, **Mechanical Engineering**

Prof. Dr. Zafer Dursunkaya ______________
Supervisor, **Mechanical Engineering Department, METU**

Examining Committee Members:

Prof. Dr. Metin Akkök
Mechanical Engineering Department, METU ______________

Prof. Dr. Zafer Dursunkaya
Mechanical Engineering Department, METU ______________

Prof. Dr. F. Suat Kadıoğlu
Mechanical Engineering Department, METU ______________

Assist. Prof. Dr. Gökhan O. Özgen
Mechanical Engineering Department, METU ______________

Prof. Dr. Ömer Anlağan
Mechanical Engineering Department, İ. D. Bilkent University ______________

Date: ______________

I hereby declare that all information in this document has been obtained and presented in accordance with academic rules and ethical conduct. I also declare that, as required by these rules and conduct, I have fully cited and referenced all material and results that are not original to this work.

Name, Last Name: ATAE JAFARI-TABRIZI

Signature :

ABSTRACT

DESIGN AND CONSTRUCTION OF AN INTERFEROMETRIC SETUP FOR DYNAMIC MEASUREMENT OF CLEARANCES INSIDE PLAIN BEARINGS

Jafari-Tabrizi, Atae
M.S., Department of Mechanical Engineering
Supervisor : Prof. Dr. Zafer Dursunkaya

December 2017, 151 pages

In this work with the help of fiber optic interferometry an experimental framework is designed and constructed to dynamically measure micron-level clearances inside main journal bearing of an engine crankshaft, and the trajectory of its shaft. For this purpose, the crankshaft is rotated at lower speeds than its operating speeds. An electric motor is used to rotate the crankshaft, and there are no pistons and connecting rods connected to the crankpins. Measured clearances from multiple points of the bearing are used to generate an estimate of the trajectory that the journal follows during a cycle. Experiments are performed both with and without lubricant inside bearing. Effect of lubricant, different rotating speeds, and repeatability of the measurement and estimation procedures are all investigated.

Keywords: Fiber optic interferometry, micron-level clearances, journal bearing, plain bearing, tribology

ÖZ

GİRİŞİMÖLÇÜM YÖNTEMİ İLE KAYMALI YATAKLARDAKİ BOŞLUKLARIN DİNAMİK ÖLÇÜMÜ İÇİN DÜZENEK TASARIMI VE GELİŞTİRİLMESİ

Jafari-Tabrizi, Atae
Yüksek Lisans, Makina Mühendisliği Bölümü
Tez Yöneticisi : Prof. Dr. Zafer Dursunkaya

Aralık 2017 , 151 sayfa

Bu çalışmada fiber optik girişimölçer kullanılarak araba motoru krankında bulunan kaymalı yatağın içinde oluşan mikron ölçeğindeki boşlukların dinamik ölçümü, ve bu ölçümlerden yola çıkarak yatağın içindeki milin hareketinin tahmini için deneysel bir sistem tasarlanıp üretilmiştir. Bunun için motor bloğuna yataklar vasıtası ile bağlı olan krank kendi çalışma hızından daha yavaş döndürülmüştür. Krankın döndürülmesi için elektrik motor kullanılmıştır, ve kranka pistonlar ve krank kolları bağlı değildir. Yatağın birden fazla noktasından ölçülen boşluklar kullanılarak milin yatak içinde bir döngü içinde takip ettiği yörünge hesaplanmıştır. Deneyler yatağın içinde yağ ve yağ olmadan ayrı ayrı gerçekleşmiştir. Yağın, farklı dönme hızlarının etkileri gibi birçok etken ile beraber, ölçüm ve ondan sonraki işlemlerin tekrarlanabilirliği irdelenmiştir.

Anahtar Kelimeler: Fiber optik girişimölçer, mikron seviyesindeki boşluklar, kaymalı yatak, triboloji

To My Family:
Nadereh, Elham, Fereidoun, Elnaz, and Elina

ACKNOWLEDGMENTS

First and foremost, I would like to express my deepest gratitude to my advisor Prof. Dr. Zafer Dursunkaya, for his never-ending support, and his immense inspiration and motivation. I consider myself lucky to have the honor of being his student.

Special thanks to Assist. Prof. Dr. Gökhan Özgen who generously shared his instruments to be used in this research.

I would also like to thank Mr. Mustafa Yalçın, for his massive help in constructing the experimental setup. It would be impossible to finish this work without his smart and practical solutions. I would like to extend my thanks to Mr. Servet Şehirli, for generously providing instruments and machines of metrology laboratory.

Many thanks to Dr. Ali Aslan Ebrinç, and Ford Otosan company, for providing us an engine block and crankshaft assembly.

Finally, I cannot describe how thankful I am to my grandmother Nadereh Tabatabai, my parents Elham and Fereidoun Jafari-Tabrizi, and my sister Elnaz Manzarzadeh for their endless love, inspiration and support, both in hard times and good times.

This research was partially supported by BAP.

The thesis was typeset in LaTeX.

TABLE OF CONTENTS

CHAPTERS

APPENDICES

LIST OF TABLES

TABLES

LIST OF FIGURES

FIGURES

CHAPTER 1

INTRODUCTION

Mechanical machinery which has surfaces interacting with each other make up an important part of today's industry. Tribology is the field that deals with these interacting surfaces. Friction, wear, and lubrication between these surfaces are the main focus of tribology. It is a fact that one of the most vital points in designing new machinery is its energy efficiency. Machines which consume less energy are both desirable from the aspect of protecting the natural environment, and also reducing the overall cost of operation and maintenance. Since in almost any mechanical machinery there are interacting surfaces, therefore tribological considerations are also a part of the design process.

One important assembly, in this case, is piston and cylinder. This assembly is composed of a cylinder (the piston) sliding reciprocally inside a relatively larger cylindrical chamber (the cylinder). During operation of a piston inside the cylinder (in a compressor, or an engine) its primary motion is reciprocating along the cylinder axis. However, piston at high speeds and (as a consequence of high speed) at high temperatures may also have another type of motion called "secondary" motion, which reduces the overall efficiency of the assembly. In [8], it is stated than in internal combustion engines secondary motion of the piston constitutes the 30-50 percent of overall mechanical losses. Another very important component of mechanical machines is the journal bearing, an essential part of rotating machinery. It is composed of a shaft (the journal) rotating inside a cylindrical hole (the bearing). Purpose of the journal bearing is to both support the rotating component and enable a frictionless rotation for it. Therefore depending on the type of load, in order to make it last for a virtually infinite time, it must be designed properly. In both piston and cylinder assembly and journal bearings, there is lubricant between two surfaces. Lubrication is necessary to minimize friction and wear, and also to help carry the load. Different states of lubrication can be explained by Stribeck curve (Figure 1.1), which schematically shows the onset of each state.

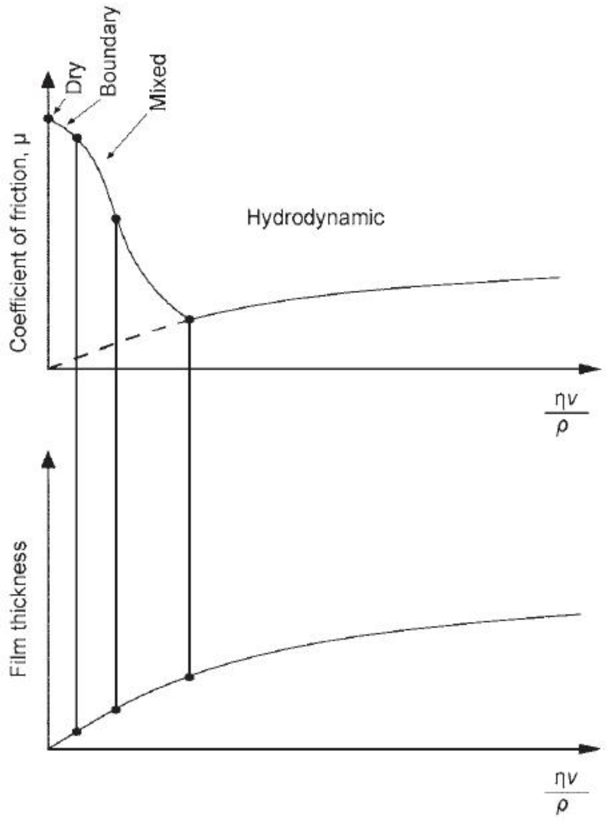

Figure 1.1: *Stribeck curve [1]*

Where η is lubricant viscosity, v is sliding velocity, p is normal pressure, and μ is coefficient of friction. According to this curve, lubricant states are

- Dry condition: there is no lubricant between sliding surfaces,
- Boundary lubrication: despite the presence of lubricant, there is contact between surfaces,
- Mixed-film lubrication: in addition to lubricant in between, there is contact

between asperities of sliding surfaces,

- Hydrodynamic lubrication: there is no direct contact between surfaces.

Lubrication state happening in journal bearings is mixed and hydrodynamic lubrication. With lubricant and type of load acting on the bearing, the pressure acting on the journal is variable in each cycle of motion. Knowledge of how film thickness changes would help to improve the bearing design. This is also true for piston and cylinders. Being able to measure how clearance changes between piston and cylinder, would make it possible to estimate the secondary motion of piston, and re-design it accordingly.

In this research, a fiber optic interferometer is designed and used to investigate the change of clearances inside a journal bearing and based on these measurements it is tried to see what kind of trajectory the journal inside bearing follows. In order to realize this task, fiber optic laser and other necessary peripherals are utilized since these components are easily accessible laser equipment. The reason for this is that the fiber optic components are at widespread use in communications technologies. The wavelength of light used in fiber optics is at 850, 1300, and 1550 nm, which is in the infrared region. Light having these wavelengths has much less attenuation in the fiber. Using this method to measure clearances inside the bearing, and to estimate the motion of the shaft is a novel approach to this problem. With addressing the issues encountered in this work, by making necessary improvements to the measurement equipment and technology, this methodology can be applied directly to a setup with actual operating conditions of the engine (or compressor) in order to obtain much more realistic estimates about shaft motion inside bearing.

CHAPTER 2

LITERATURE SURVEY

The optical interferometer is a device which uses the principle of interference of light, and the optical path difference created by it. This capability of detecting deformation, or distance change by exploiting the interference of light makes interferometers desirable in many fields of applications. In this chapter, the applications of interferometry in different areas, especially in the area of metrology are addressed. Also, different methods of measuring oil film thickness are introduced. In addition to this, methods proposed to measure and characterize rough surfaces are mentioned, and also different methods of estimating and measuring dynamic motion of journal inside bearing available in literature are summarized. Before explaining the impact of interferometry to the advances in different areas, in order to make the reader familiar with some terms used in the text, it is necessary to explain the basic theory behind it.

For the interference to happen, a light beam is divided into two (or more) beams, which travel in different paths. One of these beams is the reference beam, and the others are measurement beams. Depending on the application, these measurement beams will reflect back from a body or will pass through a media, the motion or other dynamic behavior of which is under investigation. These beams then come together to form the interference. If there is an optical path difference between the beams, then "fringes" are formed creating an interference pattern. These "fringes" are patterns, in which both constructive interference (enhancement) and destructive interference (diminution) happen alternatively [9]. In the common optical arrangements, the relation between the number of fringes and the distance change can be shown by the following equation

$$L = (N + f)\frac{\lambda}{2} \tag{2.1}$$

where L is the distance (or length), N is an integer, corresponding to the number of full fringes, and f is a fraction between 0 and 1, corresponding to fraction of fringes. Therefore a fringe observed in optical interference corresponds an optical distance equal to half the wavelength of the light source. The fraction of a fringe, defined in Equation 2.1 as f is also useful. After defining the basic terminology of optical interferometry, different applications of this method are presented. There are advances in interferometric techniques employing not optics, but acoustics [10], or atomic and molecular matter. But these are not within the scope of this study. The primary focus of this thesis is on optical interferometry and its applications. Optical interferometers, based on their working mechanism, are mainly divided into two groups: homodyne and heterodyne interferometers. Homodyne interferometers employ only one laser frequency, whereas heterodyne interferometers use two laser frequencies.

As mentioned also in [11], if the interference data collected from the interferometer is appropriately analyzed, it is possible to detect a change in the distance up to a resolution of even $1/1000$th of a single fringe. Also depending on the wavelength of the light source used in the interferometer, it is possible to reach sub-nanometer measurement resolutions. Therefore, as the wavelength of the light source decreases, the resolution of the measurements increases, meaning that potentially a resolution of a picometer is possible.

As an instance, authors in [12] have reached a measurement resolution of one picometer by using X-rays as their light source, in order to evaluate and validate the measurements of the nanometrology measuring machines. The range of the wavelength of X-rays is between 0.01 to 10 nanometers. Therefore, using Equation 2.1, it is possible to see how high the resolution of the interferometer can be. Also, an orbiting interferometer as a product of Space Interferometry Mission is designed goal of which is the measurement of displacements up to a resolution of 10 picometers [13].

In [14] development of a heterodyne interferometer is explained which is aimed at resolving picometer-level displacements and nanoradian tilts. Although initially, focus of this work was to prepare a measurement setup for Laser Interferometer Space Antenna (LISA) satellites, the application became broader so that it is also used as a dilatometer to characterize the expansion of different materials. This interferometer is also used to characterize commercial precision actuators and tilt-actuated micromirrors. Laser source used in this work is a Nd:YAG laser with a wavelength of 1064 nm, and after two beams are split, they pass through an acousto-optical modulator, so that two laser beams with different frequencies are generated. A heterodyne Michelson interferometer is introduced in [15]. According to authors this design theoretically must have a resolution of 0.2 pm, however, in experiments, it is seen that resolution is higher than that, and it is below 10 pm. Another heterodyne interferometer design with picometer resolution is proposed in [16]. There are also homodyne interferometers in the literature which are capable of detecting picometer level distance changes. Interferometer design proposed to be used in space applications, which also has a resolution in the order of picometers is given in [17], where a homodyne system with a laser wavelength of approximately 664 nm is employed. An optimized fiber-optic homodyne interferometer, with an infrared laser source (1550 nm) is introduced in [18]. The aim of this work is to perform calibrations and measurements in atomic-scale displacements. According to authors, the fact that unit of length in International System of Units (SI) is defined based on wavelength of light, makes characterizing displacements using an optical interference device to reduce uncertainties due to successive calibrations.

In [19], a Fizeau-type interferometer is introduced, which uses a He-Ne laser with the wavelength of 633 nanometers. This interferometer is capable of carrying out dynamic measurements and it is illustrated by performing dynamic surface profiling and live optical system alignment. A Mach-Zehnder interferometer is proposed which utilizes fiber optics, and is used to measure the dynamic strain of a vibrating cantilever beam. The light source used in this system is in the infrared region, with a wavelength approximately equal to 1550 nanometers. In [20] a new interferometer is introduced for measurements of absolute length. For this, they use three different laser sources at different wavelengths: a Rb-stabilized diode laser at 780 nm, a He-Ne laser at 633 nm and an iodine-stabilized frequency doubled Nd:YAG laser at 532 nm. With this configuration, they were able to measure absolute distance changes at prismatic surfaces at temperatures less than 10 K. This way it was possible to observe the thermal expansion of bodies from room temperature to cryogenic temperatures, independent of time. In [21] authors have developed an approach for high precision positioning of robotic arms and mechanisms with optical interferometry and He-Ne as the laser source. In fact, this interferometry-based guidance algorithm is part of a larger control system, in which the starting point, the endpoint and the path to be followed by the end effector of the robot is specified by other means.

Measuring oil-film thickness is one of the important research topics. Several methods for this problem are proposed in the literature, however, the most important technique is to measure the thickness of the lubricant using ultrasound waves [22, 23, 24, 25, 26]. In this method, the ultrasonic wave is reflected from the lubricant layer. When the wavelength of the ultrasonic wave is in the same order of magnitude of layer thickness, the reflection is characterized by the layer's resonant behavior, using which, the thickness of the layer can be determined [23]. There are also other methods, as in [27], where authors have designed a framework in which electrical conductivity is used to measure thickness between two stationary disks. They have applied an electric potential difference across the film and by observing the resistance they obtained an estimate of lubricant thickness. On the other hand, one of the tools suitable for this problem is optical interferometry. In [28] a method is introduced which combined fiber-optics and laser fluorescence to measure oil films in cylinder walls in engines. They were also able to show the success of this method under dynamic and high-temperature conditions. In [29] it is pointed out that contrary to other applications, knowledge of absolute thickness is required. Therefore, for the purpose of measuring the absolute oil-film thickness, an analysis of the interference data recorded with Fizeau interferometer is proposed. Authors in [30] have introduced a solution to measuring semi-transparent media, such as oil-film, in which they use wide-band interferometry. They use a laser beam having a center wavelength, with a certain bandwidth. In the experiments, they use superluminescent diode laser with a center wavelength of 820 nm, and bandwidth of 20 nm. With this configuration, they were able to reach submicron resolution. Also in this work, the importance of frequency dependence of the refractive index of the media is pointed out. For the accuracy of the thickness results, it is important to know the refractive index of the media as a function of the entire wavelength spectrum.

Measurement and characterization of different rough engineering surfaces is crucial to research fields concerning with the interaction and contact between bodies. Therefore, in time different methods were developed to define, characterize, and measure the surface profile of rough bodies. For the purpose of characterization of engineering surfaces statistical definitions are used. Solid surfaces depending on their nature may have complex structures. These complex structures can be categorized as follows [7]: (1) roughness (irregularities of shorter wavelengths), (2) waviness (irregularities of longer wavelengths), (3) lay, and (4) flaws. In most engineering surfaces these irregularities are considered to be random [7]. Therefore properties of these surfaces are commonly defined with the help of statistics. Depending on the manufacturing method, Gaussian or non-Gaussian distribution methods can be applied to model the surface. Primary variable which have the most information on the variation of height of the surface relative to a reference plane is surface roughness. There are several statistical formulations used to define surface roughness, but root mean square (RMS) method is more commonly used. Another important property regarding the surface is the correlation length, which is an indication of orientation of peaks in space. In other words, it is a measure of randomness of the surface [7]. Different techniques are reported in literature for measurement of surface characteristics. In [31] a special optical interferometer is used to measure statistical properties of polished optical surfaces, having roughnesses around 100 Å RMS. This interferometer employs fringes of equal chromatic order (FECO). In this interferometer a collimated beam of white light undergoes multiple reflections between two partially silvered surfaces. One of these surfaces is the surface being measured, while the other one is a reference surface. In another work, speckle contrast is used to measure the surface roughness and correlation length [32], and a He-Ne laser having wavelength of 0.6328 μm is used. Authors in [33] have performed a valuable set of experiments on a glass-ceramic disk substrate, using different measurement techniques. Outcome of the each experiment is compared with that of other methods, and advantages and disadvantages of different measurement techniques are discussed. These measurement techniques are stylus profiler (SP), atomic force microscope (AFM), and non-contact optical profiler (NOP). Stylus profiler is a one of the most popular methods of measuring the surface profile, which is a contact type technique. In this method a stylus is in contact with the surface, and as it moves on the surface, its displacement data are recorded. Atomic force microscope is also a contact type method, in which a sharp tip located at the end of a lever, having a very low stiffness is in contact with the surface. Also a small amount of force is applied from the lever, so that the normal force on the tip is known, from the amount of deflection of the lever. As the tip moves on the surface, with a feedback loop this applied load is kept constant by changing the distance between the tip and surface, which determines the topographic structure of the surface. The only non-contact measurement method employed in this work is the optical profiler, which is based on two-beam interferometry. They have obtained two-dimensional (line) profiles by stylus profiler, and three-dimensional (surface) profiles from atomic force microscopy and optical two-beam interferometry methods. Parameters chosen to be measured are: three vertical roughness parameters (RMS roughness, peak-to-mean roughness, and peak-to-valley roughness), and one spatial roughness parameter, that is correlation length. Depending on the size of the tip in SP and AFM methods, and magnification of the objective lens in interferometry method, spatial resolution of the measurement changes. This is an important factor in the accuracy of the results of measurements. As stated in [33] poor spatial resolution will result in an underestimation in vertical parameters (e.g., RMS roughness), and an overestimation in spatial parameter, and correlation length. In this set of experiments, AFM method has the highest spatial resolution, therefore it results in more accurate measurements. The two-beam optical interferometry method, having the lowest spatial resolutions gives the least accurate results. Some submicron wavelengths on the surface were totally filtered out in interferometry and SP methods. In [34] authors use a simplified image-speckle contrast-based method to measure the roughness and correlation length of random surfaces. Same surfaces are also measured with AFM, in order to compare the results obtained from image-speckle contrast method. In image speckle contrast method a surface is illuminated with light, from which the reflected light creates interference patterns. These patterns then can be used to get information about surface and movement of the object. In [35] a method is presented in which rms roughness values of flat and curved machined metal workpieces are measured by exploiting the dependence of wavelength on specular reflectance from surfaces. As a curved machined part, they have measured the surface roughness of shaft of the journal bearing of a crankshaft, with a known rms roughness of around 0.05 μm to 0.12 μm. The measurements are observed to be in good agreement with those obtained using stylus method. Studying the effect of surface roughness of surfaces of journal bearing is becoming increasingly important for the performance of journal bearings. There are several works, both theoretically ([36, 37, 38]) and experimentally ([39]) investigate the effect of surface roughness on the bearing performance.

In addition to the surface roughness of the journal, estimation (and, if possible, measurement) of dynamic motion of it inside the bearing is also important. One of the important works on this is [40], where mobility method is used to predict the motion of the dynamically loaded journal bearings. With this method, depending on the load that is applied on the journal, velocity of the journal center is calculated, and with this knowledge, the path that it takes during one cycle can be obtained. It is obvious that in [40] a way to validate the computed motion of the journal is not possible, however, by advancements in technology, and development of high-precision measurement techniques, new methods are developed to measure the oil film thickness inside the bearing. In [41] a feasibility study of measuring the film thickness inside bearing using optical sensors is performed. The speed of the journal was varying between 350 to 1100 rpm, and the applied load was between 0 to 55 kg. They also validated the measurements with theoretical estimations, two dimensional Reynolds equation for journal bearing design, by observing that the trends caused by changing the parameters (load or speed) are consistent with the equation. Another measurement technique is employed in [42], with four Eddy current sensors located at each bearing of the engine, so that the film thickness values are measured and the motion of the center of the shaft is obtained. These sensors work according to the Faraday's law of induction, where electrical currents are formed when the magnetic field changes. This happens when a conductor is displaced. In [43] authors measure the oil film pressure, by means of optical fiber sensors, inside the hydrodynamic journal bearings. Finally, in [44] authors measure oil film thickness, pad load, oil temperature in all three guide bearings of a 10-MW Kaplan hydropower machine, in addition to the shaft motion inside bearings. Oil film thicknesses are measured with 4 displacement sensors placed in the housing of each bearing. Oil temperatures are measured with thermocouples, and pad loads are measured using load cells.

CHAPTER 3

INTERFEROMETRIC DISTANCE MEASUREMENT

The nature of light has been the topic of a long scientific debate that lasted many centuries. Isaac Newton (1643-1727) was one of the most important scientists who believed that light has a particle nature. During the same time period, Christiaan Huygens (1629-1695) concluded from his experiments that light is a wave. This view continued to be supported by Thomas Young's double-slit experiment, in which interference patterns formed by light coming out from two closely-spaced holes were created. After James Clerk Maxwell (1831-1879) developed theories of electromagnetic waves, the light was shown to be an electromagnetic wave. From that point on, to analyze light's propagation and its behavior when encountering other light beams, its wave nature is taken into account. Therefore, interference of two or more light beams is based on the superposition principle.

3.1 Basic theory of interference

An electromagnetic wave is mathematically formulated as a vector field

$$\mathbf{E} = \mathbf{E}_o \cos(ks - \omega t + \phi) \tag{3.1}$$

Where k is the propagation constant ($k = 2\pi/\lambda$, and λ being wavelength), s is the distance traveled by the wave from its source, ω is the frequency, and ϕ is the phase shift of the wave. When two waves with the same frequency meet at a point

$$\mathbf{E}_1 = \mathbf{E}_{o1} \cos(ks_1 - \omega t + \phi_1) \tag{3.2}$$

$$\mathbf{E}_2 = \mathbf{E}_{o2}\cos(ks_2 - \omega t + \phi_2) \tag{3.3}$$

Superposition principle is used

$$\mathbf{E}_p = \mathbf{E}_1 + \mathbf{E}_2 \tag{3.4}$$

Any detector (human eye, or a photo-detector) can measure only the energy of the light beam, since these waves themselves are rapidly varying functions which average to zero in short time intervals [9]. This measured energy is called radiant power density, or irradiance $\mathrm{W/m^2}$. Irradiance is the time average of the square of the amplitude of the wave

$$I = \varepsilon_o c < \mathbf{E}_p^2 > \tag{3.5}$$

Where,

$$I = \varepsilon_o c < \mathbf{E}_p \cdot \mathbf{E}_p >= \varepsilon_o c < (\mathbf{E}_1 + \mathbf{E}_2) \cdot (\mathbf{E}_1 + \mathbf{E}_2) > \tag{3.6}$$

$$I = \varepsilon_o c < \mathbf{E}_1 \cdot \mathbf{E}_1 + \mathbf{E}_2 \cdot \mathbf{E}_2 + 2\,\mathbf{E}_1 \cdot \mathbf{E}_2 > \tag{3.7}$$

In these equations, ε_o is the permittivity of vacuum, and c is the speed of electromagnetic waves in free space. Values of these constants are $\varepsilon_o = 8.8542 \times 10^{-12}$ $(\mathrm{C} \cdot \mathrm{s})^2/\mathrm{kg} \cdot \mathrm{m}^3$, and $c = 2.998 \times 10^8$ m/s. Note that $\varepsilon_o c < \mathbf{E}_1 \cdot \mathbf{E}_1 >$, and $\varepsilon_o c < \mathbf{E}_2 \cdot \mathbf{E}_2 >$, are irradiance values of the separate light beams, and $< 2\,\mathbf{E}_1 \cdot \mathbf{E}_2 >$ corresponds to the interference of the waves. Therefore irradiance equation can be rewritten as

$$I = I_1 + I_2 + I_{12} \tag{3.8}$$

In this equation I_{12} is the term corresponding to the interaction between two light beams. If the two light beams are originating from two independent sources, then the interference will average to zero ($I_{12} = 0$). These light beams are said to be mutually incoherent. However when the light beams both originate from the same light source splitting in two different beams, and under a certain assumption which will be mentioned later in this section, then these beams are mutually coherent. For the interference of mutually coherent beams irradiance of the resultant wave can be written as

$$I = I_1 + I_2 + 2\sqrt{I_1 I_2}\cos(\delta) \tag{3.9}$$

Where δ is the phase difference between $\mathbf{E}_1$ and $\mathbf{E}_2$ at the point where two light beams meet

$$\delta = \phi_2 - \phi_1 \tag{3.10}$$

Therefore in fact it can be said that the irradiance is a function of phase difference between two light beams. Initially, mutually coherent light beams have no phase difference, but when they follow different directions then the difference between their optical path lengths increase, which leads to phase difference. Due to the nature of the term $\cos(\phi)$ in Equation B.4, irradiance of the resultant beam will oscillate between a maximum and minimum value. Constructive interference happens when irradiance is at a maximum, and destructive interference happens when irradiance is at a minimum. Maximum irradiance can be written as

$$I_{max} = I_1 + I_2 + 2\sqrt{I_1 I_2} \tag{3.11}$$

When

$$\delta = 2m\phi \tag{3.12}$$

Where m can be any integer and zero. Constructive interference is shown in Figure 3.1.

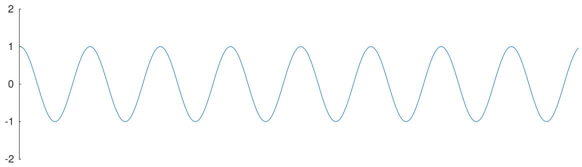

(a) I_1

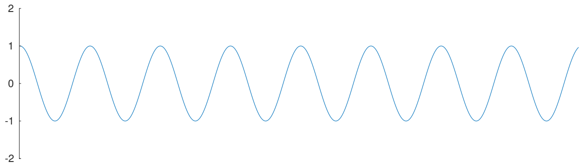

(b) I_2

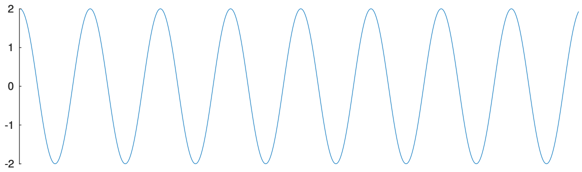

(c) I_{max}

Figure 3.1: *Constructive interference*

Minimum irradiance is written as

$$I_{min} = I_1 + I_2 - 2\sqrt{I_1 I_2} \tag{3.13}$$

This happens when

$$\delta = (2m+1)\phi \tag{3.14}$$

Again m can take any integer value or zero. This case is shown graphically in Figure 3.2.

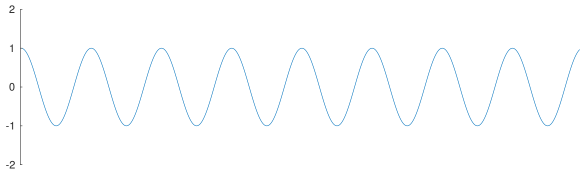

(a) I_1

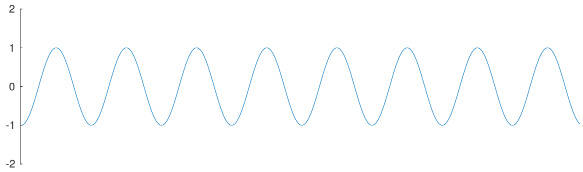

(b) I_2

(c) I_{min}

Figure 3.2: *Destructive interference*

Usually the phase difference changes continually, and this happens when the relative path difference between light beams continuously changes, or the recombination point of the two light beams changes. This causes $\cos\delta$ to change alternatively so that irradiance changes between maximum and minimum values, leading to the creation of the so-called interference fringes. These interference fringes can be visually expressed as a function of several entities. It is possible to express interference pattern as a function of the phase difference of two light beams or time, or also as a distance at which light beams meet. In Figure 3.3 interference fringes can be seen as a function of phase difference.

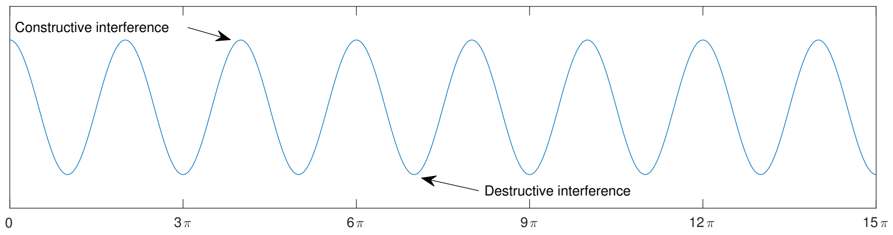

Figure 3.3: *Interference fringes as a function of phase difference*

The contrast of the fringes seen in Figure 3.3 is measured with fringe visibility (v), which varies between 0 and 1, defined as

$$v = \frac{I_{max} - I_{min}}{I_{max} + I_{min}} \tag{3.15}$$

Fringe visibility decreases as the path difference between two beams decreases. Mathematically, the difference between I_{max} and I_{min}, which is I_{12}, vanishes. This fact is related to the mutually-coherent assumption which was made earlier. For independent light beams originating from same light source the mutually-coherent assumption becomes weaker as the path difference between two beams becomes larger.

As mentioned above, interference patterns called fringes are generated when the phase difference between two light beams is continuously changing. This is a direct result of the continuous change in the path difference between the two beams. Thomas Young (1773-1829) performed a famous experiment which showed the wave-nature of the light. With this experiment, the relation between path difference of beams and their wavelengths became clear. The idea was to measure the path difference, and also by detecting the location of constructive and destructive interferences, calculate light beams' wavelength. Later this knowledge was exploited in the opposite sense, that is if the path difference is unknown but the wavelength of the light source is known, by investigating the interference pattern, path difference can be calculated. This methodology became the basis of optical interferometry.

3.2 Optical interferometry

An optical interferometer is a device which uses interference of light and the interference patterns and fringes resulting from the path differences for measurements in different applications. These applications include distance measurement, surface irregularities measurement, and also the measurement of index of refraction [45]. In optical interferometers light originating from a source is split into two independent coherent beams, and after taking different paths they meet to create interference patterns.

Optical interferometers can be classified in two different ways [9]. One is how the light originating from the source is split into two (or more) light beams:

1. Wavefront-division interferometers use portions of the same wavefront as new individual waves, as in Young's double-slit experiment.

2. Amplitude-division interferometers create new beams with partial reflection or refraction, which acts as a beam-splitter.

The second way of classification is based on the number of beams used in interference procedure. For instance, the Michelson interferometer is an amplitude-division type interferometer which uses two light beams. The Fabry-Pérot interferometer uses multiple beams.

3.2.1 The Michelson interferometer

This kind of interferometer was designed in the year 1881 by Albert Michelson. This interferometer became a highly important invention for modern physics and was used in many areas [9]: as an experimental tool in support of the special theory of relativity, to see the tidal effect of the moon on earth, and many other examples. A schematic of the Michelson interferometer can be seen in Figure 3.4.

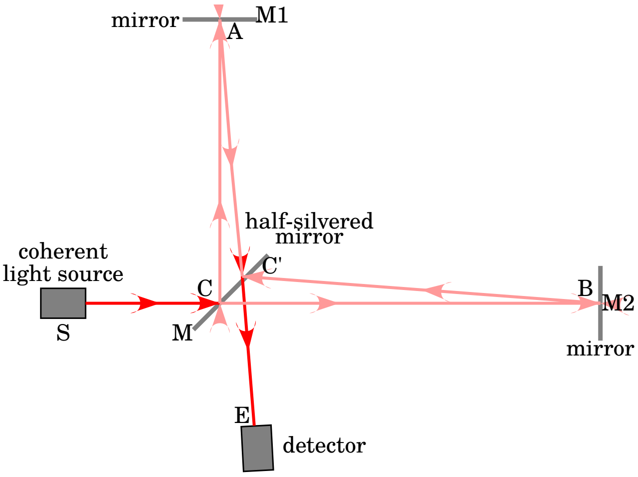

Figure 3.4: *Michelson interferometer [2]*

In Michelson interferometer, as shown in Figure 3.4 coherent light beam originated from the light source is split into two beams at the point C with a half-reflective and half-transmissive mirror. One beam is directed to point A at mirror M_1 and the other one is directed to point B at mirror M_2. Reflecting beams from mirrors M_1 and M_2 again meet at the point C' of mirror M, and their interference is directed to point E, where the irradiance of the superposed light beam is detected by the detector. Optical path difference between two beams changes as one of the mirrors moves away from the half-reflective mirror, while the other mirror acts as a reference. As this happens the irradiance measured at detector changes from I_{max} to I_{min}, and then it increases back to I_{max}. This is counted as one fringe. How measured irradiance changes depends on how much one of the mirrors has moved. A change in irradiance from I_{max} to I_{min} and then back to I_{max} (one fringe) corresponds to a distance of $\lambda/2$ in the movement of one of the mirrors. This fact can be generalized as follows: if N fringes are visible, then the distance traveled by the movable mirror (l) is equal to

$$l = N \times \frac{\lambda}{2} \tag{3.16}$$

As will later be explained, this equation is used as the basis for optical interferometry in this work.

3.2.2 The Fabry-Pérot interferometer

The Fabry-Pérot is an example to the interferometers which employ multiple light beams. This interferometer is also used in many applications, such as analysis of hyperfine spectral line structure, determination of refractive indices of gases, and calibration of the standard meter in terms of wavelengths [9]. A schematic of this interferometer is shown in Figure 3.5.

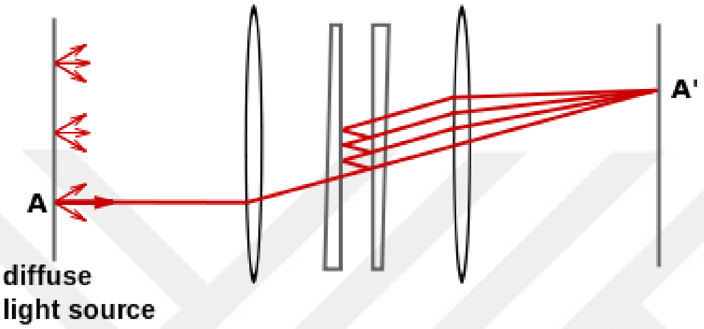

Figure 3.5: *Fabry-Pérot interferometer [3]*

In this interferometer, there are two parallel partially reflective plates, where the reflective surfaces face each other. Outer surfaces of the plates have a wedge shape with small angles, in order to eliminate the formation of interference patterns from outer surfaces of the plates. Light is generated from the source at point A, then it enters the cavity between the parallel plates with a certain angle with respect to the optical axis of the system. Multiple beams created from the reflective surfaces of the plates then are recombined at point A' in order to create interference patterns.

CHAPTER 4

EXPERIMENTAL SETUP AND PROCEDURE

4.1 Fiber optics

The interferometer constructed in this work uses optical fibers, a tool utilizing the property of the clear materials to transport light beams. The idea of guiding the light beams with clear materials such as glass surfaced from the experiment done in the year 1870 by an Irish physicist John Tyndall in USA [4]. The light was shone into a container full of water in a dark room. Then the bung of the container was pulled out. It was observed that the water gushed out containing the light. Therefore the conclusion was that water, as a clear material, has the capability to guide the light.

It is known that light travels at different speeds inside materials with different index of refraction. Lower refraction index means higher speed of light. Based on this fact when light traveling at a certain angle inside a medium is about to enter into another medium with lower refractive index, it enters to it with a different angle. Depending on the refraction indices of the two materials and the initial angle of incidence of the light, there is a critical angle at which it will move along the boundary between two media as the light enters the new medium. Light with an angle of incidence higher than critical angle will reflect back into the same medium. This phenomenon can be seen in Figure 4.1. Measured from the normal direction, beam with an angle higher than the critical angle reflects back.

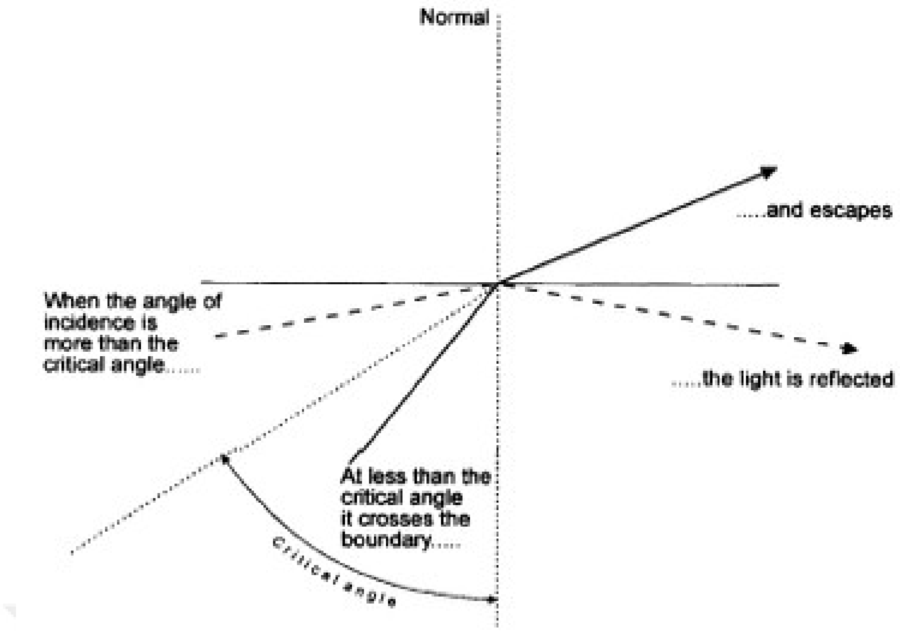

Figure 4.1: *Critical angle of incidence of light [4]*

This mechanism keeps, and guides the light inside the fiber optic cable, the core of which has a higher refraction index than the surrounding medium. This phenomenon is called total internal reflection (TIR).

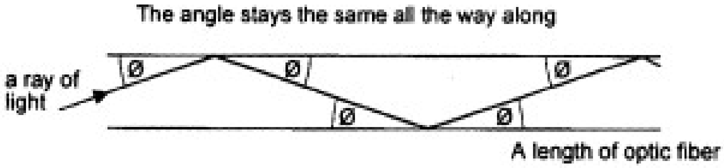

Figure 4.2: *Light moving inside fiber by bouncing from its boundaries [4]*

As seen in Figure 4.3 fiber optic cable is composed of a core typically made of silica, surrounded by a cladding, which is also a glass material. The cladding is added to prevent the contamination from dirt, dust or grease since these can cause leakage of light from the core. Finally, another jacket, made of plastic surrounds the cladding. This jacket, sometimes called primary buffer is only for mechanical protection.

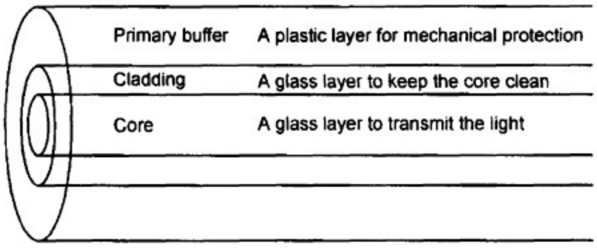

Figure 4.3: *Composition of a typical fiber cable [4]*

There are two different types of fiber optic cables: single-mode, and multi-mode. In multi-mode fibers the light can travel in different paths, and diameter of core is around 60 μm, while in a single-mode fiber only one path for the light is allowed and the diameter of single-mode fiber is typically around 9 μm. Single-mode fibers have higher bandwidth compared to multi-mode fibers [46].

4.2 Fiber optic interferometer

The fiber optic interferometer uses fiber optical components to guide the laser light from the source, separate the light beams, direct it to the target and receive it back and recombine it with the reference beam to be directed to the photodetector, a device which converts irradiance to voltage output. A simple schematic showing the basic components required in a fiber optic interferometer is shown in Figure 4.4.

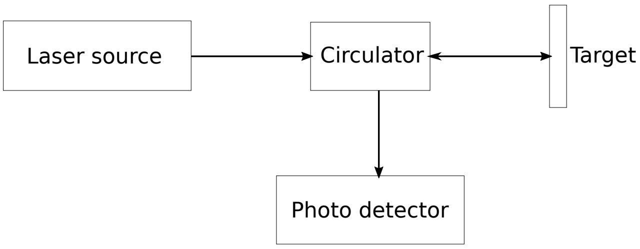

Figure 4.4: *A simple fiber interferometer*

Optical fiber cables are used to carry the light originating from laser source to the next component, circulator, which is a critical part of the interferometer. Circulator guides the light from the source to the target surface, and then receives it again after reflection from the target surface, and this time guides it to photodetector through fiber optic cable. Irradiance measured at the photodetector can be calculated with the equation below [5]

$$I = I_1 + I_1 + 2\gamma\sqrt{I_1 I_2}\cos(\phi) \tag{4.1}$$

Where, for a fiber optic interferometer
$I_1 = I_o R_1$
$I_2 = (1 - R_1)^2 R I_o$
$\gamma = \sin(\xi)/\xi$
$\phi = 4\pi x_o/\lambda$
Thus rewriting the equation gives

$$I = I_o\left[R_1 + (1 - R_1)^2 R + 2(1 - R_1)\sqrt{RR_1}\frac{\sin(\xi)}{\xi}\cos\left(4\pi\frac{x_o}{\lambda}\right)\right] \tag{4.2}$$

Where,
I_o: Irradiance of the laser diode radiation couple into the fiber
R_1: Reflectivity of the end face of the fiber
R: Reflectivity of external target mirror
$\xi = \pi(l/l_c)$: The ratio of path-length difference and the coherence length multiplied by constant π
λ: Wavelength of the laser beam
x_o: Gap between fiber and the target mirror

Based on this equation, the irradiance detected at the photodetector is shown in Figure 4.5. When the path-length difference between interfering beams is equal to the coherence length of the laser beam, visibility becomes zero. These points can clearly be seen in Figure 4.5 where the intensity vanishes.

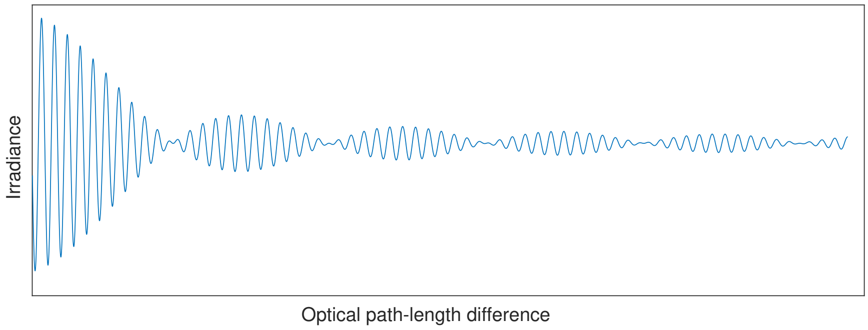

Figure 4.5: Variation of detected intensity at photodetector with distance between interferometer at target mirror

Since the light coming out of fiber towards the target mirror diverges, the amount of light reflecting and entering the fiber again will depend on the distance between fiber and mirror. Longer the distance, lower the percentage of incoming light. This makes the optical power detected at the photodetector to depend on this distance. Variation of optical power with distance between fiber end and target mirror is shown in Figure 4.6.

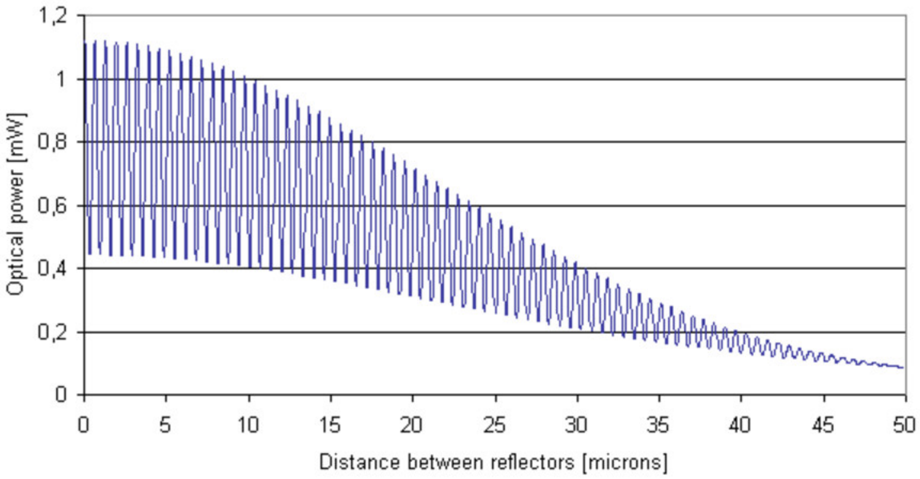

Figure 4.6: Dependence of optical power detected at photodetector on the distance between fiber end and target mirror [5]

4.3 Final experimental setup

Experimental setup has three main parts: (i) optical stage, containing the fiber optics equipment making the interferometer,(ii) mechanical stage, which is rotating the crankshaft on the engine block, and (iii) data acquisition and analysis stage which records the data sent from photodetector, and converts them to meaningful data for analysis.

4.3.1 Optical stage

The optical stage includes a laser source. Fiber optic cables are all single-mode fibers. Core diameter of the fibers is 9 μm and cladding diameter is 125 μm. Light beam originating from the laser source is input to the isolator, in order to prevent the back-reflection to the laser source, and minimize the losses. Then it is guided to a beam splitter, which divides the beam into 4 individual coherent beams with the amplitude-division method so that it is possible to record interference patterns from 4 independent points. Every beam is input to a circulator, so that first it is guided by a fiber optic cable having an open end from one side to the target surface, and reflected back by the same cable to circulator again. This time circulator guides it, again with fiber optic cables to the photodetector. A schematic of the optical stage is given in Figure 4.7.

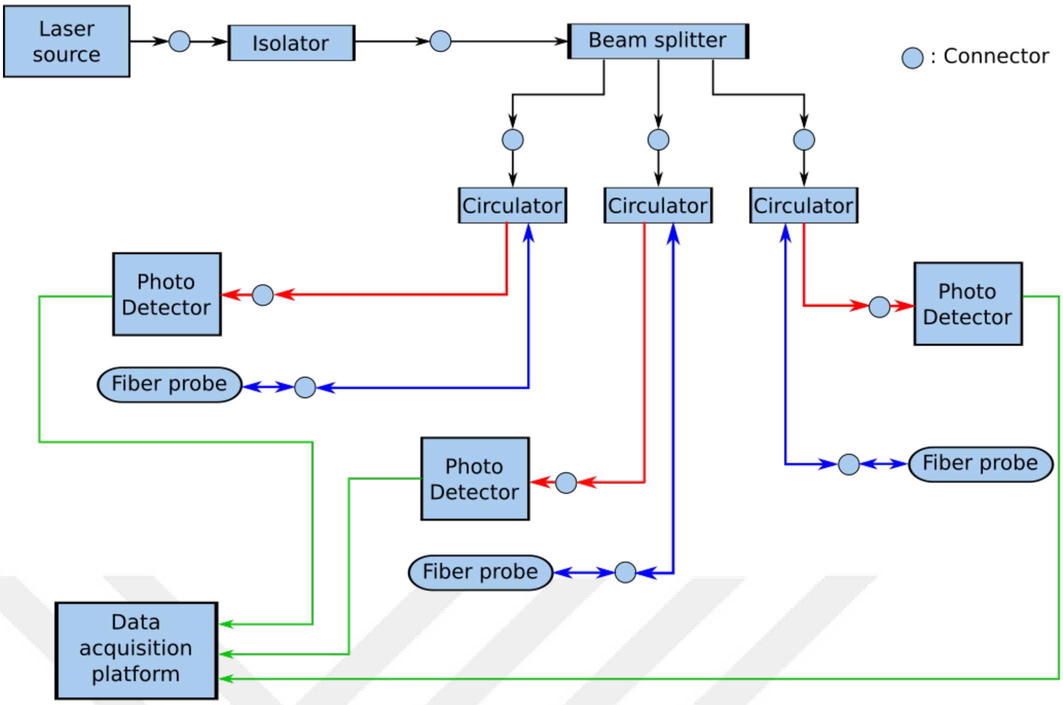

Figure 4.7: *A schematic of optical stage*

There are special connectors which are used to connect all separate components to each other. Before explaining every component in detail, it is best to explain the connector type. All the components are connected to each other with FC/APC connectors. “FC” stands for ferrule connector, and “APC” stands for angled-physical contact, designed to be used for single-mode fibers. In this of connectors, both ends are angled at 8° degrees. Physical contact minimizes the back-reflection due to the gap between the fiber ends, and angled ends minimize the back-reflections at the point of contact [46]. FC/APC connectors have a threaded body as shown in Figure 4.8, ferrules at both ends are in contact inside this body.

Figure 4.8: *Connector*

4.3.1.1 Laser source

Laser source used in experiments has a wavelength of 1550 nm. It is manufactured by Oz Optics, as a Highly Stable Laser Diode Source (HIFOSS), Distributed Feedback (DFB) laser. It can be seen in Figure 4.9. Specifications of the laser source are given in Appendix A.1.

Figure 4.9: *Laser source*

4.3.1.2 Isolator

A fiber optic isolator blocks returning light to the laser. First input light to the isolator is collimated and then sent to a focusing lens on the output, so that the light is coupled back to the output fiber. Isolators can be either polarization-sensitive or polarization insensitive. In experiments, the polarization-insensitive isolator manufactured by Oz Optics is used. It can be seen in Figure 4.10. Specifications of the isolator are given in Appendix A.2.

Figure 4.10: *Isolator*

4.3.1.3 Beam splitter

A beam splitter divides the light into two or more individual beams. These devices can be manufactured such that they can produce beams with equal optical powers or different optical powers. For the experiments, a beam splitter by Oz Optics is used, which divides the incident beam into four beams with equal optical powers. It can be seen in Figure 4.11, and its specifications are given in Appendix A.3.

Figure 4.11: *Beam splitter*

4.3.1.4 Circulators

An optical circulator is a device with three ports: Light entered from Port 1 is directed to Port 2, and light entering from Port 2 is directed to Port 3. For the experiments, light coming from the laser source (passing through the isolator, and after beam splitter) enters Port 1. In order to be sent to the target surface, it enters Port 2. Finally after being reflected from the surface of the target, it enters again to Port 2, and in order to be sent to the photodetector it is directed to Port 3. Fiber optic miniature circulators manufactured by Oz Optics are used in experiments. One of the circulators is shown in Figure 4.12. Specifications of the circulators are given in Appendix A.4.

Figure 4.12: Circulator

4.3.1.5 Fiber optic cables

All the components explained above are equipped with fiber optic cables from both input and output sides. In addition to these, fiber optic cables with an open end are used to send the light to and receive from the target surface. The open end has a polished ferrule. This polished ferrule end is shown in Figure 4.13. Specifications of the fiber optic cables are given in Appendix A.5.

Figure 4.13: Fiber optic cable end, with polished ferrule

4.3.1.6 Photodetectors

A photodetector is a device that converts light into voltage or current. This is an essential device if the interference data generated from the optical stage of the experimental setup is to be recorded and analyzed digitally by computer. For the experiments, Ge-based transimpedance amplified photodetectors with switchable gain, manufactured by Thorlabs are used. In order to send the data converted to voltage to a data acquisition platform, cables with BNC connectors (simply called BNC cables) are used.

Photodetector is shown in Figure 4.14, and its specifications are given in Appendix A.6.

Figure 4.14: *Photodetector*

4.3.2 Mechanical stage

This stage is composed of engine block, the crankshaft installed on it, the electrical equipment necessary to rotate the crankshaft, and the special stages manufactured to hold the fiber optic cables in their position during the experiments. Next, these components are explained in detail.

4.3.2.1 Crankshaft assembly and bearings of engine block

In the experiments, a 5-cylinder engine is used. Main bearings of the engine block can be seen in Figure 4.15.

Figure 4.15: *Main bearings of the engine block*

This engine holds the crankshaft only, without pistons. Crankshaft is attached to the engine block with bearing caps. Engine assembly containing engine block, crankshaft, and bearing caps can be seen in Figure 4.16. Detailed information on the crankshaft assembly is given in Appendix A.7 and Figure A.1.

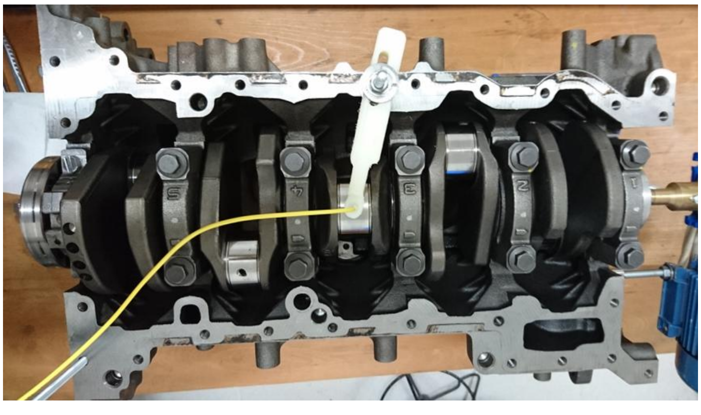

Figure 4.16: *Crankshaft assembly in engine block*

4.3.2.2 Fiber optic probe holders

In experiments there are three fiber optic holders, attached to the main engine block, in order to hold the optic probes in their respective positions during the experiments. First, to hold the optic probe which plays the role of an encoder, the holder seen in Figure 4.17 is manufactured.

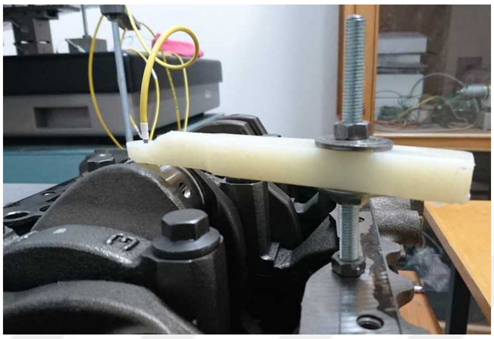

Figure 4.17: *Probe holder used for the encoder probe*

There is another holder designed to guide the optic probes to the holes on the engine bearing caps. The main reason to manufacture this holder is to keep the optic cables straight and minimize the risk of them being broken. This holder can be seen in Figure 4.18.

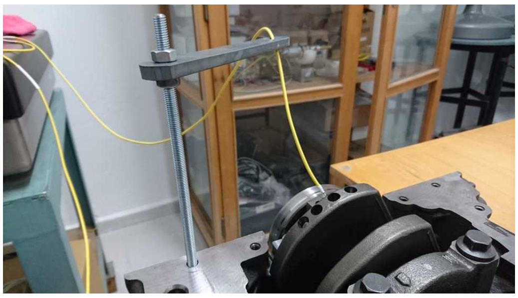

Figure 4.18: *Holder used to keep the cables inserted into the bearing caps*

Another part is manufactured specially for the probe which will be inserted into a hole opened in the engine block, to take measurements from below of the main bearing of the engine. This part can be seen in Figure 4.19.

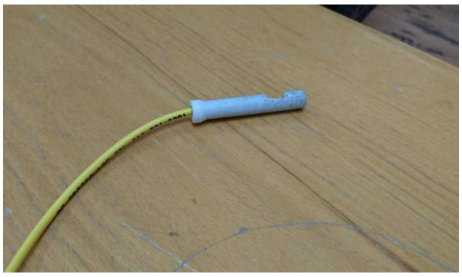

Figure 4.19: *Holder used to insert the probe inside the hole drilled in engine block*

4.3.2.3 Electrical motor and reducer gearbox

In order to rotate the crankshaft, a three-phase 380V electric motor equipped with a reducer is used. Reducer is a gear mechanism, which reduces the rotational speed provided by the electric motor, to be transferred to the next stage. Electric motor and reducer can be seen in Figure 4.20. Details about electrical motor can be found in Appendix A.8.

Figure 4.20: *Electric motor and reducer*

As it also can be seen in Figure 4.20, a flange is used to connect the output shaft of the reducer to the shaft of the crankshaft.

4.3.2.4 AC motor driver

An AC motor driver is used to drive the electric motor. This driver can be seen in Figure 4.21. Detailed specification of the electric motor is given in Appendix A.9.

Figure 4.21: *Inverter*

4.3.3 Data acquisition and analysis stage

As mentioned above, the optical data input to the photodetectors are converted into voltage, then using coaxial cables with BNC connectors they are sent to data acquisition (DAQ) platform. DAQ platform consists of a connector block equipped with BNC connectors, a shielded cable from the connector block to DAQ card located on the motherboard of the desktop computer. Connector block simplifies the task of transferring analog data from measurement devices with BNC connectors to the DAQ card on the computer. MATLAB is used to receive the analog data from DAQ device. These data saved in the desktop computer are then transferred to the laptop computer for further processing and analysis. Below, the components of the data acquisition and analysis stage are explained more in detail.

4.3.3.1 Coaxial cables

Coaxial cables having male BNC connectors at both ends are called in short BNC cables. These cables have a conductor core, insulated by a layer, and another conductor shield is braided around the dielectric insulator. Coaxial cables are used in many fields where it is important to keep the signal loss at minimum [47]. In Figure 4.22 one of the cables used can be seen.

Figure 4.22: *Coaxial cable with BNC male connectors*

4.3.3.2 Data acquisition platform used for initial experiments

Figure 4.23: *DAQ platform used for initial experiments*

During the initial phases of the study National Instruments' USB-4431 data acquisition platform, shown in Figure 4.23 was used. This device is connected to the computer via USB port and does not require extra connector block and cable. It has four analog inputs and one analog output. Maximum sampling rate available in this device is 102.4 kS/s. More specifications can be found in Appendix A.10.

4.3.3.3 Data acquisition connector block

Connector block in these experiments is National Instruments' BNC-2110. It is a shielded connector block with BNC female connectors. Analog signal from photodetectors are sent with coaxial cables to the connector block, and from this device, they are sent through data acquisition cable to the data acquisition card mounted on the motherboard of the desktop computer. Connector block can be seen in Figure 4.24. Specifications of the connector block can be found in Appendix A.11.

Figure 4.24: *Data acquisition connector block*

4.3.3.4 Data acquisition cable

For the purpose of transferring signal from connector block to the data acquisition card in the desktop computer, SHC68-68-EPM shielded data acquisition cable manufactured by National Instruments is used. Specifications of the shielded cable are given in Appendix A.12.

4.3.3.5 Data acquisition card

DAQ card used in the experiments is PCIe-6321 multifunction I/O card manufactured by National Instruments. It uses the high-speed serial computer expansion bus called PCI Express (PCIe), and has a maximum sampling rate of 250 kS/s for a single channel. Further specifications of the card are given in Appendix A.13, and it can be seen mounted on the motherboard of the desktop computer in Figure 4.25.

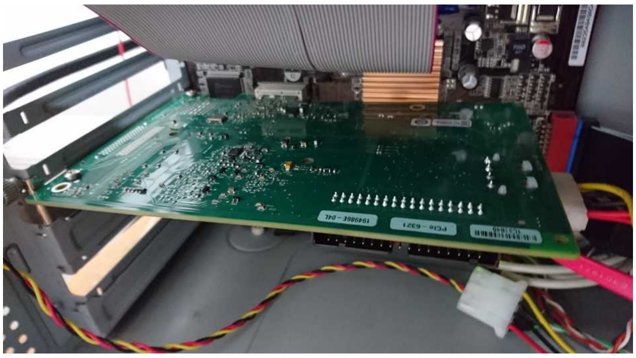

Figure 4.25: *Data acquisition card*

4.3.3.6 Data acquisition software

MATLAB version used in experiments is 2013a. Data acquisition platform also needs NI-DAQmx software as the driver to be installed on the desktop computer. The version of NI-DAQmx used in experiments is 9.7.5. The signal is acquired by Data Acquisition Toolbox of MATLAB, using session-based interface. This feature can be used with National Instruments DAQ devices, directly from command line. A session can be created, and input channels are added to the session. When duration and sampling rate of the data acquisition is configured, data acquisition process is ready to start. After data acquisition is finished, acquired data are stored as an array, which can be used and plotted immediately, or saved for further analysis and processing.

4.3.3.7 Desktop computer

Figure 4.26: *Desktop computer*

Desktop computer (shown in Figure 4.26) is used for the task of data acquisition. DAQ card is mounted on its motherboard. Its operating system is Microsoft Windows XP Professional. Other specifications of the desktop computer are given in Appendix A.14.

4.3.3.8 Laptop computer

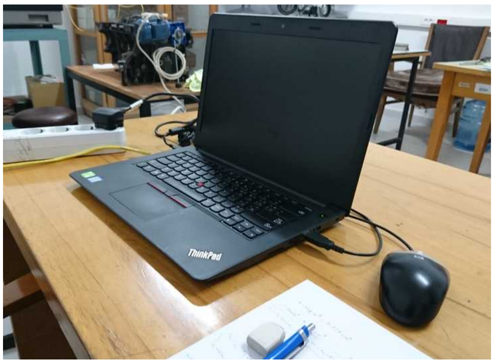

Figure 4.27: *Laptop computer*

Laptop computer (shown in Figure 4.27) is used for analysis and post-processing of the data acquired by the desktop computer. It is a Lenovo Thinkpad E470. Its operating system is Ubuntu 16.04 LTS. Other specifications of the computer are given in Appendix A.15.

4.4 Experimental procedure

In order to be able to understand the experimental procedure, an overall view of the experimental setup, as a diagram, can be seen in Figure 4.28.

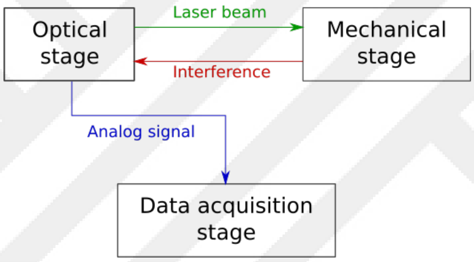

Figure 4.28: *A diagram of the experimental setup*

The laser beam produced by the laser source in optical stage is sent to the target surface in the mechanical stage, through the fiber optic equipment explained above. In this work, the target surface of the laser beam is the surface of the shaft rotating inside the journal bearing. In order to reflect the beams to and from the surface of the shaft, in total four holes are drilled around the journal bearing. Three of these holes are drilled on the bearing cap, and the fourth one is drilled in the engine block. Diameter of the holes is 1.8 mm. Top view and the view from inside of the bearing of the cap with three holes can be seen in Figure 4.29. The fourth hole can also be seen in Figure 4.30. The special part produced to hold the probe, introduced previously in this chapter can also be seen in this figure.

(a)

(b)

Figure 4.29: *Holes drilled on the bearing cap as seen (a) from top, and (b) from the view inside the bearing*

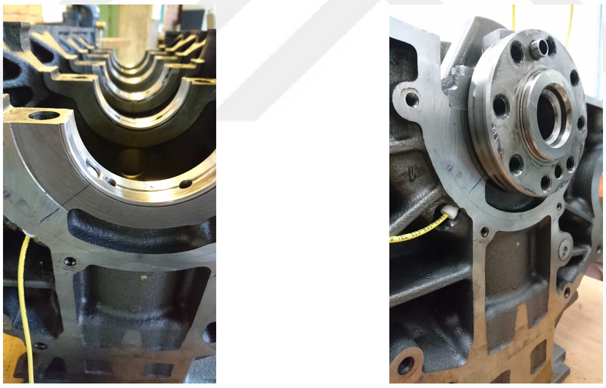

(a) *(b)*

Figure 4.30: *Fourth hole drilled on the engine block as seen, (a) from inside bearing, and (b) from outside engine block*

In addition to the targets for the laser beam explained above, another probe is used to act as an encoder, called "encoder probe". This probe has two uses

- To measure the rotational speed of the crankshaft, while it is rotating with electric motor,

- To divide the acquired optical data into cycles, and specify the start and end points of the cycles.

After installation of the encoder probe, all the experiments are done with at least 2 probes, one being the encoder probe.
The steps to be followed to perform an experiment are listed below

1. Check if the connections between optical equipment and data acquisition platform are established. If not, connect them.
2. Turn on the laser source, photodetector, and desktop computer.
3. Switch on the power to the electric motor driver.
4. Turn on the desktop computer and open MATLAB.
5. Using the command line of the MATLAB, create a data acquisition session. Name of the DAQ device, its active channels, duration, and the sampling rate of the experiment must be specified.
6. Start the electric motor, using the rotary switch located in the motor driver.
7. Use the same switch to specify the rotational speed of the motor.
8. Start the data acquisition process and wait until it is finished.
9. Stop the electric motor using the same rotary switch.
10. Turn off the laser.
11. Save the acquired data, and transfer them to the laptop computer for data analysis processes.
12. Cut the electric motor driver.
13. Clean the probe used in the journal bearing with isopropyl alcohol and a microfiber cloth, to remove the lubricant on the ferrule.
14. Perform data analysis on the acquired data using the laptop computer.

CHAPTER 5

DATA ANALYSIS PROCEDURE

After interference signals are acquired and saved in the desktop computer, they are transferred to the laptop. Before data analysis, the signal must be smoothed, in order to remove the random. Then interference data are divided into the cycles. These are done using MATLAB. After this, they are converted to generate clearance curves. This task is done in MATLAB and C++ environments. Finally these clearance curves of the same cycle which are obtained from different points on the bearing, are used to obtain a set of possible trajectories that the shaft has followed during that cycle, again in MATLAB. In this chapter, these processes are explained in detail.

5.1 Raw data filtering

Acquired and saved data in the desktop computer is "raw", which means that in order to get the intended information from it, random noise inside it must be removed. Since in these experiments nature of the noise is generally random, and the signal is a time-domain encoded one, the most suitable method for eliminating the noise is moving average filter. This method of filtering the noise is simple and easy to implement. It works with taking an average value for a certain data points of the raw signal to produce the filtered signal. The basic equation of moving average filtering can be written as [48]

$$y[i] = \frac{1}{M} \sum_{j=0}^{M-1} x[i+j] \tag{5.1}$$

In this equation $x[]$ is the noisy input signal, $y[\,]$ is the filtered output signal, and M is called the number of points in the average, normally called "window size" of the filter. The window size of the filter plays an important role. Therefore, care must be taken in selecting its value for filtering the signals, based on the factors listed below:

- Diameter of the beam incident to the target surface,
- Rotational speed of the crankshaft,
- Sampling rate of the data acquisition platform.

The diameter of the beam coming out of fiber probe is approximately 7 μm, and for all experiments, sampling rate is selected to be 10^2kS/s, therefore the only variable factor is the rotational speed of the crankshaft. Speed determines the number of samples acquired for a unit of distance traveled by the surface of the shaft. As the speed increases, sample points corresponding to a unit distance decreases, and vice versa. This affects the selection of the window size.

5.2 Obtaining relative clearance change

After smoothing the signal, next task is to convert it to a clearance variation curve. This procedure is explained with an example. A sample (and filtered) optical output can be seen in Figure 5.1. This signal is taken from the surface of the bearing during an experiment with crankshaft.

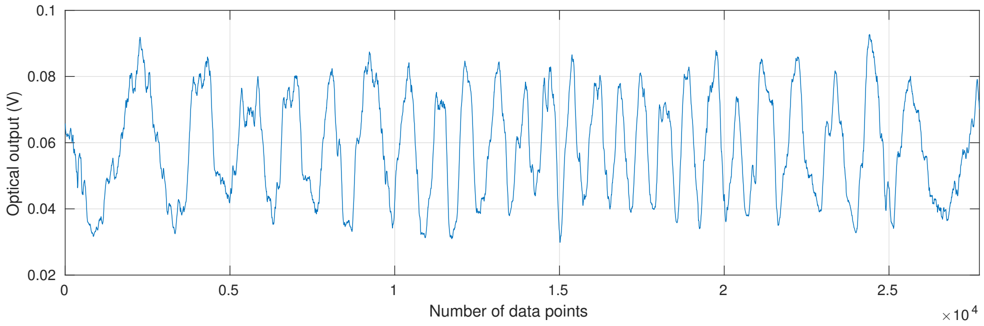

Figure 5.1: *A sample optical output taken from an experiment*

The first thing to do with an optical signal after smoothing is to identify individual fringes in it. This task can be done by locating the local maxima and minima of the signal, using MATLAB. First, the local maxima are found and shown in Figure 5.2.

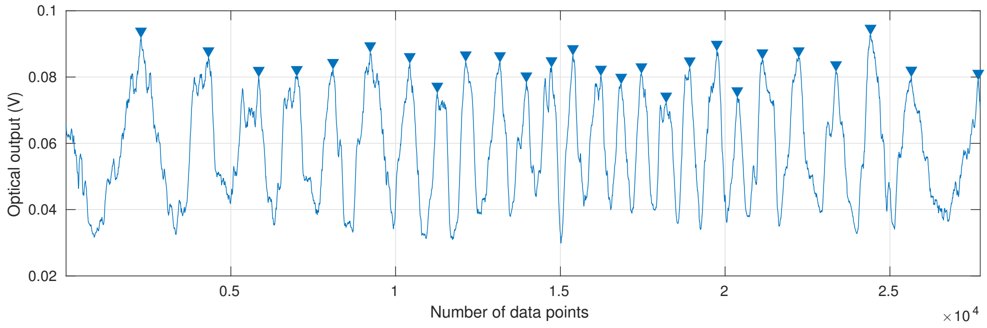

Figure 5.2: *Finding the local maxima (peaks) of the signal*

In order to find the local minima (valleys), peaks of the inverse of the signal are found, as shown in Figure 5.3.

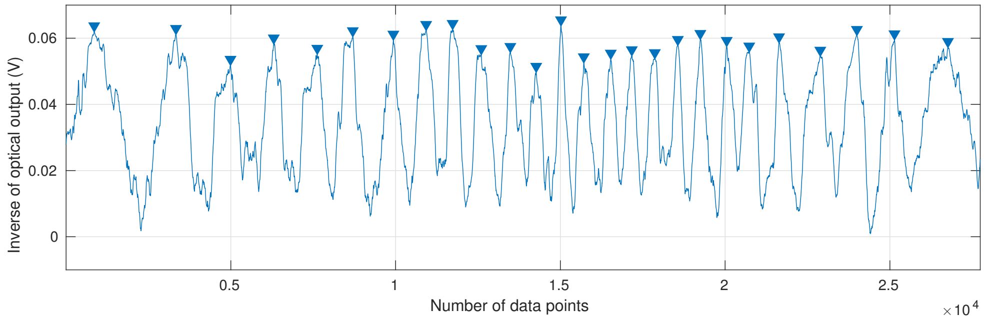

Figure 5.3: *Finding the local minima (valleys) of the signal*

Data points corresponding to local maxima and minima are written and saved in separate text files, and along with the text file containing the data points of the whole signal they are sent to a code written in C++, as inputs. This code implements the algorithm used to convert optical output (fringes) to the relative distance change. Algorithm calculates the phase difference at the each data point, and uses it to obtain the "clearance curve". Phase difference calculation is done for every individual fringe, using the maximum and minimum irradiances of every individual fringe. Then, by adding the phase differences calculated for every fringe cumulatively, overall clearance curve is obtained. Equation to calculate the phase difference can be derived from the general interference equation

$$I = I_1 + I_2 + 2\sqrt{I_1 I_2}\cos(\Delta\phi) \tag{5.2}$$

In Equation 5.2 resulting irradiance I depending on the value of $\cos(\Delta\phi)$ can take both I_{max} and I_{min} values

$$I_{max} = I_1 + I_2 + 2\sqrt{I_2 I_2} \tag{5.3}$$

$$I_{min} = I_1 + I_2 - 2\sqrt{I_1 I_2} \tag{5.4}$$

In Equations 5.3 and 5.4 common term is $2\sqrt{I_1 I_2}$. Therefore by re-writing Equation 5.3 as

$$2\sqrt{I_1 I_2} = I_{max} - (I_1 + I_2) \tag{5.5}$$

And inserting it in Equation 5.4 the following equation can be obtained.

$$I_1 + I_2 = \frac{I_{max} + I_{min}}{2} \tag{5.6}$$

This time, it can be seen that the term $(I_1 + I_2)$ is common in Equations 5.5 and 5.6. Therefore by using these equations following expression is obtained

$$2\sqrt{I_1 I_2} = \frac{I_{max} - I_{min}}{2} \tag{5.7}$$

By using Equations 5.6 and 5.7 general interference equation given in Equation 5.2 can be written only in terms of I_{max}, I_{min} and phase difference $(\Delta\phi)$

$$I = \frac{I_{max} + I_{min}}{2} + \left(\frac{I_{max} - I_{min}}{2}\right)\cos(\Delta\phi) \tag{5.8}$$

This expression can be simplified by defining

$$A = \frac{I_{max} + I_{min}}{2} \tag{5.9}$$

And

$$B = \frac{I_{max} - I_{min}}{2} \tag{5.10}$$

Thus

$$I = A + B\cos(\Delta\phi) \tag{5.11}$$

Phase difference can be obtained as

$$\Delta\phi = \cos^{-1}\left(\frac{I-A}{B}\right) \tag{5.12}$$

Phase difference $(\Delta\phi)$ for every data point of the signal is calculated, given the terms I, I_{max}, and I_{min} for every data point are known. I is known since it is the optical output. I_{max} and I_{min} are obtained when the whole signal is divided into individual fringes. Every fringe has its I_{max} and I_{min} values, and it remains the same for data points inside which that fringe is composed of.

In order to obtain the clearance curve following equation is used

$$C = \frac{\lambda}{4}\left(\frac{\Delta\phi}{\pi}+n\right) \tag{5.13}$$

Where,

C: Relative clearance change at a data point

λ: Wavelength

n: Positive integer value equal of the number of fringe at a data point

With implementation of this algorithm for the signal shown in Figure 5.1, clearance curve shown in Figure 5.4 is obtained.

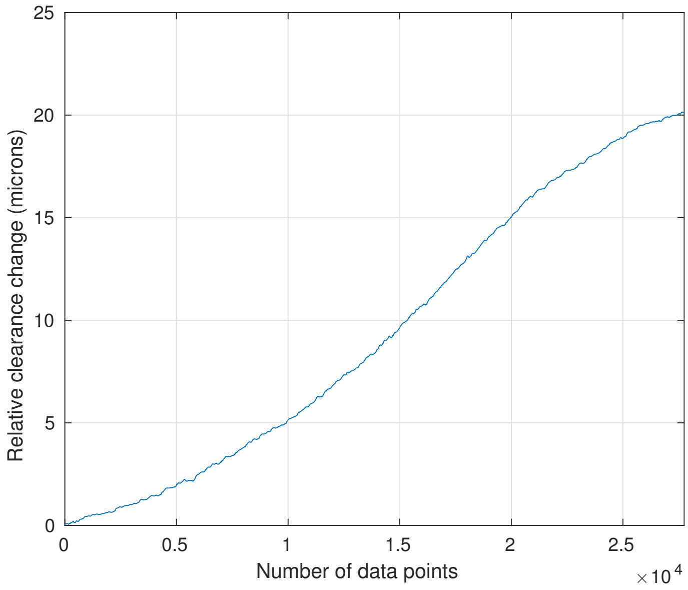

Figure 5.4: *Clearance curve*

A constant increase in clearance would result in a clearance curve which is a straight line, with constant slope. Deviations of the computed clearance curve from the straight line can be due to different reasons:

- Rate of change of the clearance might be variable,
- The actuation mechanism might not be generating a constant motion,
- Target surface might be rough.

The deviation of the clearance curve shown in Figure 5.4 can be seen in Figure 5.5.

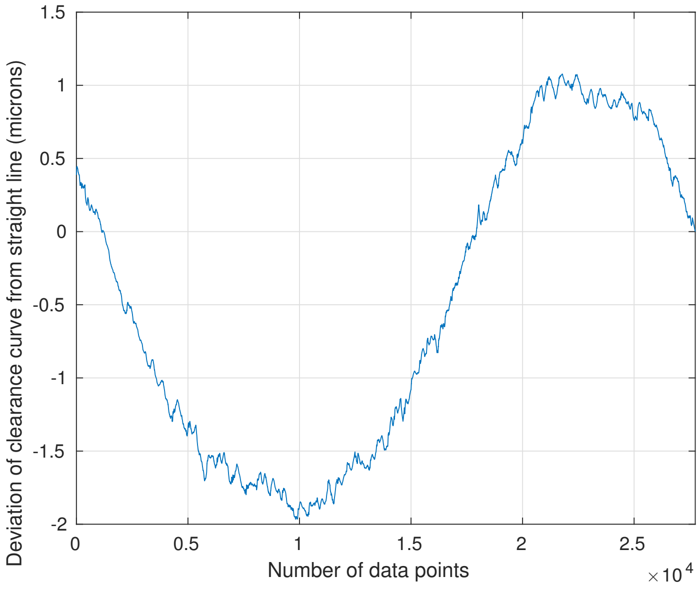

Figure 5.5: Deviation of clearance curve from straight line

In this case, where the clearance curve is expected to change its slope, or even change its direction because of motion of the shaft, this deviation is expected. It can be said that the major deviation source is change in rate of change of the clearance.

5.3 Obtaining trajectory of the shaft

Using four measuring points around the circumference of the bearing, it is possible to obtain clearance curves corresponding to multiple points from the surface of the shaft inside journal bearing, simultaneously. This way a trajectory for the shaft can be obtained. Before deriving a methodology for calculating the trajectory of the shaft from clearance information, first, the basic coordinate system to define the angular position of the shaft is explained.

The trajectory of the shaft for its full cycle is actually a collection of the following pair: angular position, and corresponding eccentricity of the data points constituting the cycle. This pair can be used to show the position of the shaft in a polar coordinate system, as given in Figure 5.6.

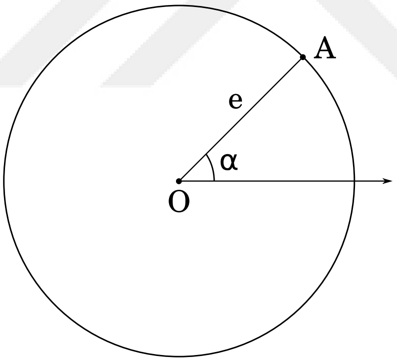

Figure 5.6: *Coordinate system used to define angular position of the shaft inside bearing*

In Figure 5.6 the pair (e, α) defines the position of point A. Reference direction for the polar coordinate can also be seen in this figure. For the case of a shaft with a radius of R_s inside a circular cavity (bearing) with a radius of R_b, this system defines the position of the shaft as shown in Figure 5.7.

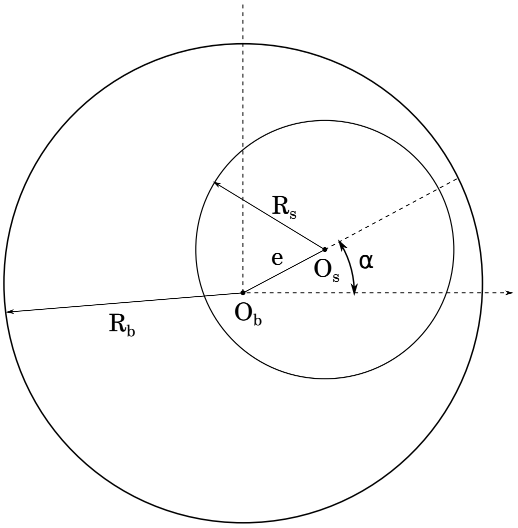

Figure 5.7: *Defining the position of the shaft inside bearing using coordinate system introduced in Figure 5.6*

In this system angular position of the shaft is defined as the angle between the line connecting two center points, O_s and O_b, and reference direction of the polar coordinate. Reference direction of this polar coordinate is the same as the x-axis of the Cartesian coordinate, whose origin is located at the center of the bearing.

In this study, the gap between the hub and the shaft, which is a function of θ, will be named “the clearance”. The clearance, h, between shaft and bearing at any known point (e, α) from a point A on the bearing at an angle of θ can be calculated with Equation 5.14.

$$h = c_r - e(t) \times \cos(\alpha(t) - \theta) \tag{5.14}$$

Where,
c_r: Nominal radial clearance $(R_b - R_s)$
$e(t)$: Eccentricity of the shaft’s center with respect to bearing’s center
$\alpha(t)$: Angular position of the shaft’s center center with respect to reference direction
θ: Angular position of the point A with respect to reference direction

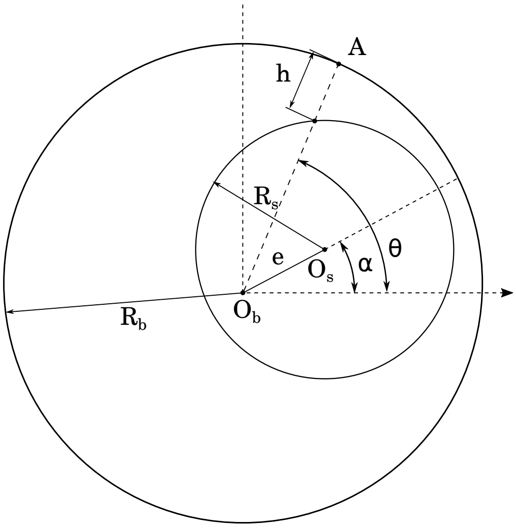

Figure 5.8: *Visualization of problem of calculating the clearance between shaft and bearing at point A*

Main concern is to be able to estimate the coordinates of the center of the shaft using thickness values measured from multiple points on the bearing wall. In Equation 5.14 by taking nominal radial clearance c_r and angular position of point A (i.e., θ) as known, following terms are unknown and finding them will give the position of the shaft: $e(t)$ and $\alpha(t)$. Clearance h is an absolute value, however using interferometry its relative change during a certain time can be measured. Therefore at two different times, t_0 and t_1 using Equation 5.14

$$h_o = c_r - e(t_o) \times \cos(\alpha(t_o) - \theta) \tag{5.15}$$

$$h_1 = c_r - e(t_1) \times \cos(\alpha(t_1) - \theta) \tag{5.16}$$

Using Equations 5.15 and 5.16 will give

$$\Delta h_A = e(t_1)\cos(\alpha(t_1) - \theta) - e(t_o)\cos(\alpha(t_o) - \theta) \tag{5.17}$$

Where,
$\Delta h_A = (h_{1A} - h_{oA})$: difference of two consecutive clearance values measured from point A on the bearing wall
In this equation the that number of unknowns is four: $e(t_o)$, $\alpha(t_o)$, $e(t_1)$, $\alpha(t_1)$. However if initial values for the position of the shaft, that is, $e(t_o)$, $\alpha(t_o)$, are known, or can be estimated, then number of unknowns can be reduced to only two. This

way by adding a second measurement point, with a known angular position (β), and producing the following equation

$$\Delta h_B = e(t_1)\cos(\alpha(t_1)-\beta) - e(t_o)\cos(\alpha(t_o)-\beta) \tag{5.18}$$

Where, $\Delta h_B = (h_{1B} - h_{oB})$: difference of two consecutive clearance values measured from point B on the bearing wall,

The following system of equations can be written

$$\begin{cases} \Delta h_A = e(t_1)\cos(\alpha(t_1)-\theta) - e(t_o)\cos(\alpha(t_o)-\theta) & (5.19) \\ \Delta h_B = e(t_1)\cos(\alpha(t_1)-\beta) - e(t_o)\cos(\alpha(t_o)-\beta) & (5.20) \end{cases}$$

In this system of nonlinear equations there are two unknowns: $e(t_1)$, and $\alpha(t_1)$. Therefore by manipulating this system to become a nonlinear system of equations, to satisfy the following

$$\begin{cases} u[e(t_1),\alpha(t_1)] = 0 & (5.21) \\ v[e(t_1),\alpha(t_1)] = 0 & (5.22) \end{cases}$$

Then a multidimensional root finding algorithm can be used to find the unknowns. Functions u and v are written as

$$\begin{cases} u[e(t_1),\alpha(t_1)] = e(t_1)\cos(\alpha(t_1)-\theta) - e(t_o)\cos(\alpha(t_o)-\theta) - \Delta h_A & (5.23) \\ v[e(t_1),\alpha(t_1)] = e(t_1)\cos(\alpha(t_1)-\beta) - e(t_o)\cos(\alpha(t_o)-\beta) - \Delta h_B & (5.24) \end{cases}$$

Newton-Raphson method is used as the root finding algorithm for this problem. This method is based on simplification of the original nonlinear equation to its first order Taylor series expansion [49]

$$f(x_{i+1}) = f(x_i) + (x_{i+1} - x_i) f'(x_i) \tag{5.25}$$

Where,

x_i: Initial guess at the root

x_{i+1}: point at which the slope intercepts the x-axis

By rearranging, the new guess can be found as

$$x_{i+1} = x_i - \frac{f(x_i)}{f'(x_i)} \tag{5.26}$$

One-dimensional form of the Newton-Raphson method, explained above, can be used to derive a multidimensional method. This time a multi-variable Taylor series expansion is required. For the two-variable case suitable for this problem, by taking

$e(t_1) = x$

$\alpha(t_1) = y$

First-order Taylor series for functions u and v can be written as

$$u_{i+1} = u_i + \frac{\partial u}{\partial x}\Big|_i \Delta x + \frac{\partial u}{\partial y}\Big|_i \Delta y \tag{5.27}$$

$$v_{i+1} = v_i + \frac{\partial v}{\partial x}\Big|_i \Delta x + \frac{\partial v}{\partial y}\Big|_i \Delta y \tag{5.28}$$

Where,

$\Delta x = x_{i+1} - x_i$

$\Delta y = y_{i+1} - y_i$

By applying the similar re-arrangement and re-writing done to one-dimensional case, new estimates can be found using following equations

$$x_{i+1} = x_i - \frac{u_i \frac{\partial v}{\partial y}\big|_i - v_i \frac{\partial u}{\partial y}\big|_i}{\frac{\partial u}{\partial x}\big|_i \frac{\partial v}{\partial y}\big|_i - \frac{\partial u}{\partial y}\big|_i \frac{\partial v}{\partial x}\big|_i} \tag{5.29}$$

$$y_{i+1} = y_i - \frac{v_i \frac{\partial u}{\partial x}\big|_i - u_i \frac{\partial v}{\partial x}\big|_i}{\frac{\partial u}{\partial x}\big|_i \frac{\partial v}{\partial y}\big|_i - \frac{\partial u}{\partial y}\big|_i \frac{\partial v}{\partial x}\big|_i} \tag{5.30}$$

These equations are used iteratively to improve the estimate and finally converge to answers which are within an error limit.

In order to demonstrate the algorithm developed to estimate the trajectory of the path, a synthetic motion for a shaft inside bearing with known geometrical properties is generated. Radial clearance is selected to be 60 μm, and eccentricity is defined as shown below, which is changing with angular position, ϕ

$$e = 4 \times (1 - 0.2 \times \sin(2\phi)) \tag{5.31}$$

This trajectory is shown in Figure 5.9.

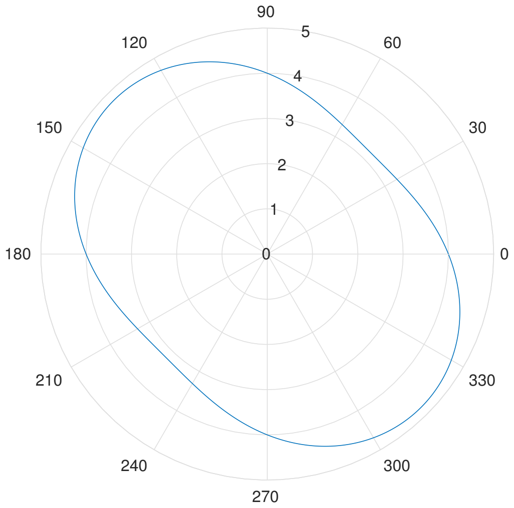

Figure 5.9: *A sample simulated trajectory of the shaft center inside bearing*

Two points A and B simulated to be on the bearing wall have the following angular positions

$\theta = \pi/2$: Angular position of point A

$\beta = \pi/4$: Angular position of point B

For trajectory defined above, clearance change measured from points A and B is shown in Figure 5.10.

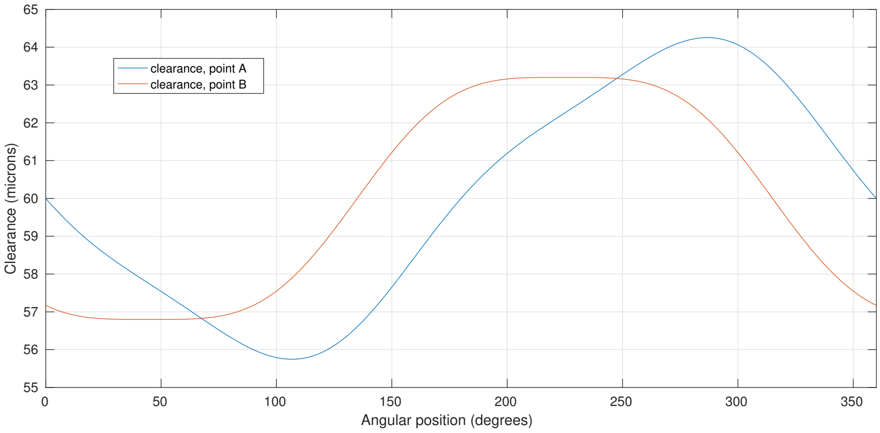

Figure 5.10: *Simulated clearance change measured from points A and B*

Clearance values are input to the implementation of the Newton-Raphson algorithm in MATLAB, and trajectory of the shaft center is estimated as shown in Figure 5.11.

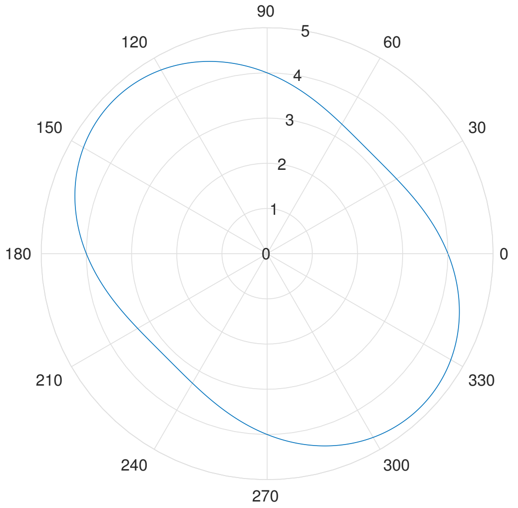

Figure 5.11: *Estimated trajectory of the shaft center from simulated clearance curves shown in Figure 5.10*

It can be seen that the algorithm successfully estimates the trajectory based on the measured clearances from two points on the bearing wall.

CHAPTER 6

RESULTS AND DISCUSSION

In this chapter the process and evolution of experimental setup is explained. First, tests with a piston and cylinder assembly of a compressor, and their outcomes are mentioned. Then tests performed with main bearing on the engine are presented. In this case, the procedure of conducting experiments can be divided into two stages, where each has their own aims, and expectations. In the first stage of tests, called preliminary tests, the aim is to get a solid grasp of how to measure clearance changes inside the bearing, and set the expectations from the main tests. Points and problems encountered at this stage are all listed, and probable causes of them are explained. In next stage of tests, called final tests, more detailed and extensive tests are done. A methodical procedure to extract optical data of every cycle of the crankshaft is introduced (with “encoder probe”), and several factors affecting the behavior of the optical data are addressed. Effect of these factors on the optical data are investigated, and possibilities of eliminating these effects are studied.

6.1 Initial experiments with compressor piston

Prior to constructing the final experimental setup, initial experiments with different applications of the clearance measurement of plain bearings are done. In these experiments, it was attempted to dynamically measure clearances inside piston and cylinder assembly of a refrigerator piston. Being able to measure and observe the variations of the clearance while the piston is making its primary motion (i.e., reciprocal motion) inside cylinder would create a potential improvement in designing and manufacturing compressors with higher efficiency. Changes in clearance inside cylinder are due to translational motion of piston perpendicular to the cylinder wall, and its rotational motion on piston pin axis. In this section the progress made and the outcomes from these experiments are explained. A piston and cylinder assembly of refrigerator compressor can be seen in Figure 6.1.

Figure 6.1: *Piston and cylinder assembly of a refrigerator compressor*

It is known that different materials have different levels of reflectivity for light with a certain wavelength. Therefore in order to have a reference for the reflectivity of a steel surface, first a mirror-finished surface made of stainless steel; a gauge block, is examined. Gauge blocks are used as a calibration for precision length measuring instruments. Their surfaces are lapped to a very smooth finish. Using the experimental setup whose details are explained in [50], optical data shown in Figure 6.2 are obtained.

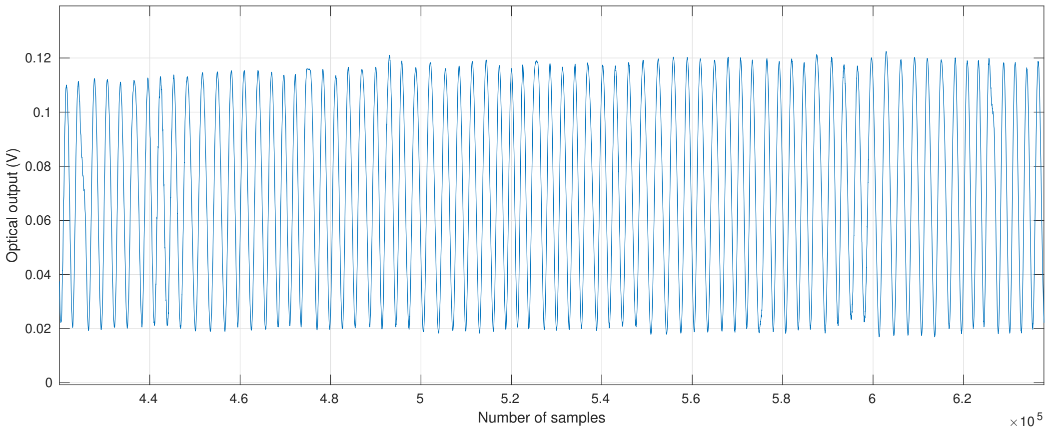

Figure 6.2: *Optical data obtained from surface of gauge block*

It can be seen that fringes are very smooth. Visibility of this optical data is approximately 0.7, which is an acceptable value for a reference surface. With this result, it can be validated that given the surface of the piston is properly finished, it will reflect the light.

In order to realize a controlled version of motion of piston inside the cylinder, the setup schematically shown in Figure 6.3 is designed. Configuration of the fiber optic equipment used in these tests can be seen in Figure 6.4. In this setup, a stepper motor is used to rotate the crankshaft. There are holes in the cylinder body, in which fiber optic probes are located. Addition of a reducer, in order to eliminate the step motion of the stepper motor is necessary between stepper motor and crankshaft. As it can be seen in Figure 6.1 cylinder itself is a part of a larger part of the compressor. Therefore unnecessary parts around cylinder are cut out, as seen in Figure 6.5.

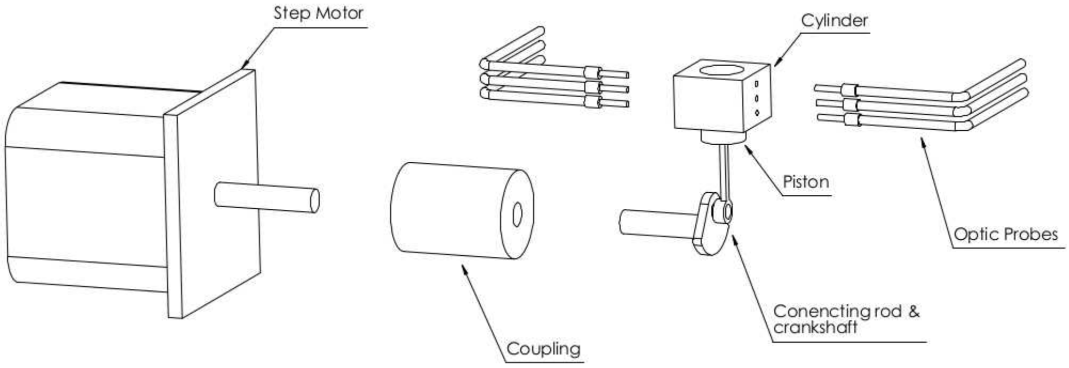

Figure 6.3: *Schematic of the test setup designed to measure the clearance inside piston and cylinder assembly*

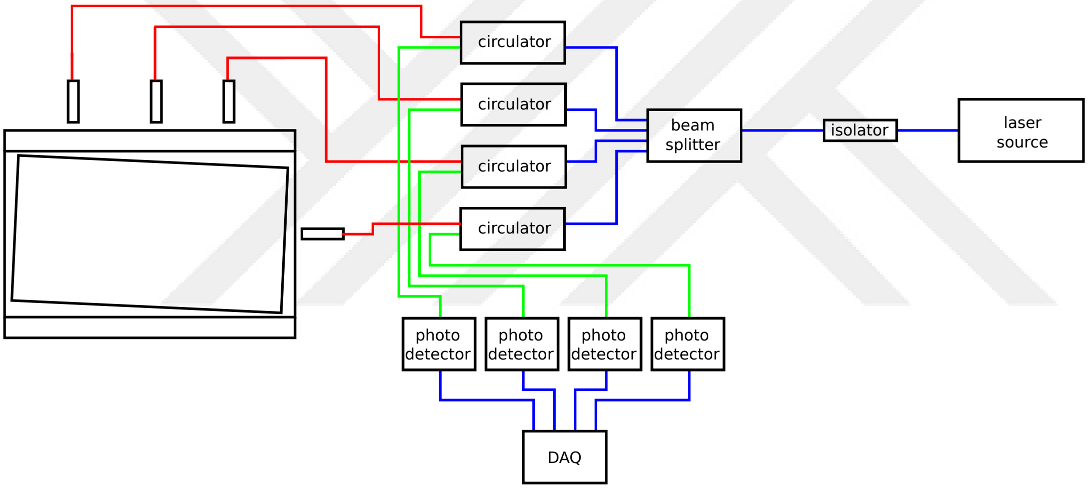

Figure 6.4: *Configuration of fiber optic equipment for piston and cylinder experiments*

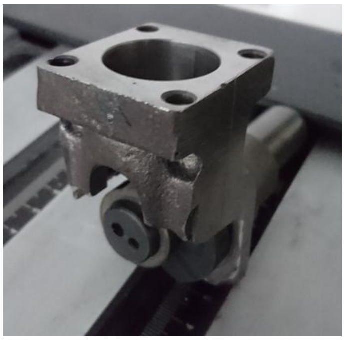

Figure 6.5: *Cylinder used in experiments*

Based on the schematic shown in Figure 6.3, experimental setup is constructed as shown in Figure 6.6.

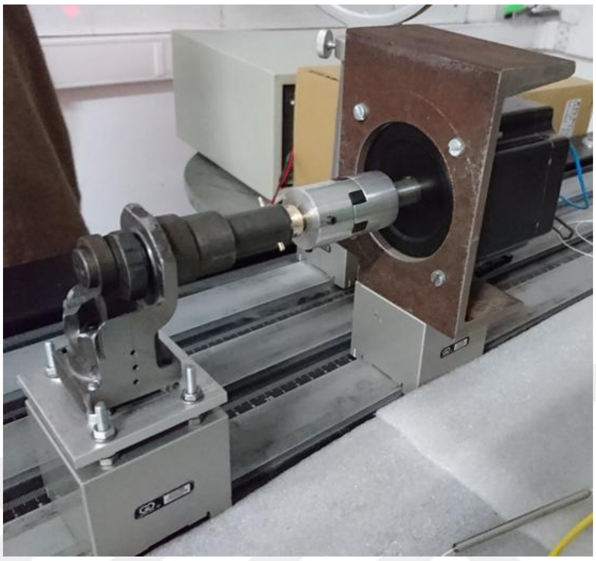

Figure 6.6: *Piston and cylinder experimental setup*

However, constructing only the necessary experimental setup is not enough for the interferometric measurement of the clearances inside the piston and cylinder assembly. Due to the nature of the interferometer, target surface of the apparatus must be of optical quality. In this application target surface is the surface of the piston. However, original surface of the piston, due to the coatings applied, is not suitable for interferometric measurements. Therefore operations must be done on the surface to improve its quality. Optimally a sophisticated procedure of operations can bring a surface made of stainless steel (piston's material) to the most reflective surface finish, called "mirror finish". However, this process requires professional skill. Also, cylindrical geometry of the surface adds to difficulties. The first attempt for this was to polish the surface using wet-and-dry sandpaper. This kind of sandpaper is applied to the surface mainly with the addition of water and produces surfaces with high smooth quality. Piston after wet-sanding operation can be seen in Figure 6.7.

Figure 6.7: *Surface of piston wet-sanded with wet-and-dry sandpaper*

With this piston, tests are performed and optical data during one full cycle of the crankshaft is acquired. This signal can be seen in Figure 6.8. In this optical data, some features of the piston and cycle can easily be pinpointed, the points where the piston reverses its direction can also be seen. These are the Top Dead Center (TDC) and Bottom Dead Center (BDC) positions of the piston. Also from sudden changes in the amplitude of the signal, the time when the groove of the piston starts to pass in front of the probe can be detected. Finally, by observing the amplitude of fringes in certain regions of the cycle some comments can be made on the relative proximity of the piston to fiber optic probe (or cylinder wall). When amplitude of signal is higher, this means that piston is closer to the probe.

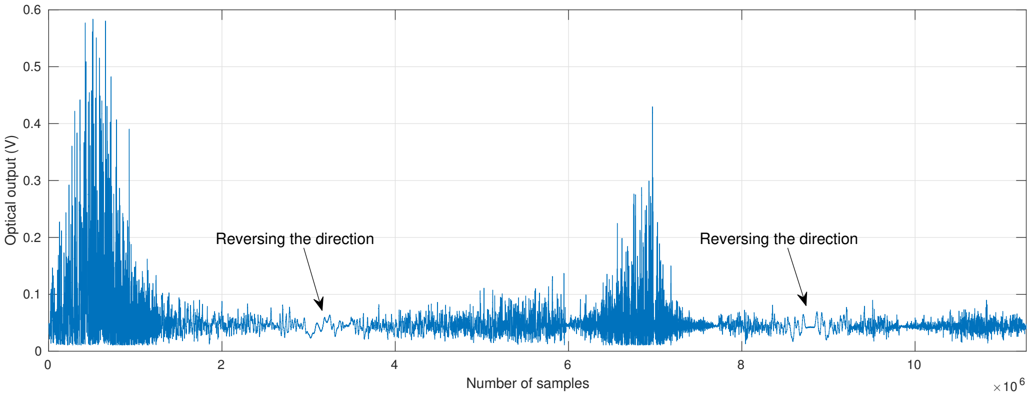

Figure 6.8: *Optical output obtained during one cycle of crankshaft*

However, in addition to detecting the features and main characteristics of the motion of the piston, the necessary thing is to detect distinct fringes from optical data. As it can be seen in Figure 6.9, quality of optical data is not sufficient to enable the resolution of individual fringes.

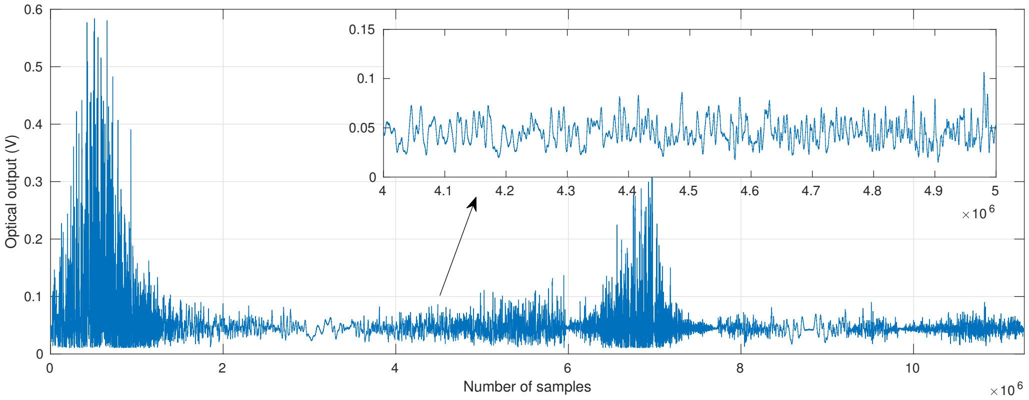

Figure 6.9: *A detailed sample of optical data obtained from surface of piston during its one full cycle*

After not being able to get any meaningful relative clearance estimates from optical data acquired from the piston, next its surface was further polished in an industrial polishing workshop. After the operation in the polishing workshop, it was observed that surface of the piston has become much more reflective, but there is a significant amount of waviness on its surface. These waves on the surface were of the same order of magnitude of relative clearance changes inside the cylinder. Therefore any optical data acquired from this surface will not be able to give reliable information on piston's relative clearance with the cylinder wall. Conclusion from these attempts is that in order to realize the task of dynamic measurement of piston and cylinder clearances, surface of the piston must be polished with sophisticated processes, which exceeds the capability of this work.

6.2 Preliminary tests

This stage of the experiment can be divided into two steps: the first step is before integrating the engine-crankshaft assembly into the experimental setup, and the second step is when the engine-crankshaft assembly is already integrated into the experimental setup, and initial tests are done to observe and evaluate the outcomes, so that analyzing the test results of the final stage of tests can be done easier, with previous knowledge and experience. In these tests, there is no lubricant inside bearing. In the first step of the preliminary tests, it is tried to make sure that surface of the bearing shaft has an optical quality. Due to the size of the crankshaft, taking measurements from the surface of the bearing shaft is impossible without a special engine-crankshaft assembly. Therefore another part with similar surface characteristics is used in these tests. This part is a piston pin. After validating the measurability of the surface, the mechanical stage of the experimental setup is constructed. Details of this stage are given in Chapter 4. In the initial tests with newly added mechanical stage, the bearing used in the experiment does not contain any lubricant. The important reason for this is that the lubricant decreases the visibility of the optical output considerably. Therefore lack of any media (except air) in the gap between the optical probe and target surface would increase the visibility. For the preliminary tests, this is a desirable consideration, since this way the feasibility of the actual "final" tests can be investigated.

6.2.1 Tests on a piston pin

An essential characteristic affecting the outcome of the interferometry experiments is the surface quality of the target surface. The surface roughness of the target surface must be low enough to reflect the beam back to its source. This back-reflection might not be perfect, the beam will reflect from the surface with a wider angle. Important point is to make enough amount of reflected light back to the source (fiber optic probe). In addition to factors such as angle of light incident on the surface, proximity of the optical probe to the surface, and wavelength of the light beam, another important factor, as mentioned above, is the roughness of the surface.

Before preparing the engine-crankshaft assembly, in order to see if the surface of the bearing shaft is capable of reflecting the light successfully, another cylindrical object with very similar surface roughness to the bearing shaft was tested. This object is a piston pin used in a reciprocating compressor for automotive applications, shown in Figure 6.10.

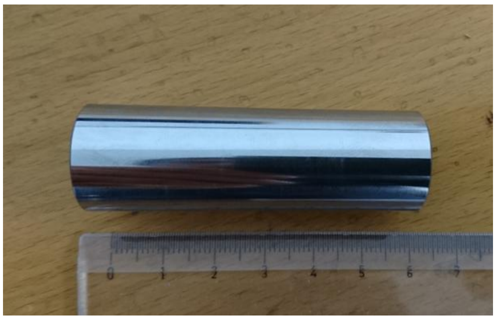

Figure 6.10: Piston pin

The experimental setup used to analyze the surface of the piston pin is an apparatus used to measure clearances of a surface only in horizontal direction. The optical probe is mounted on a stepper-motor-actuated plate, moving with a constant speed on horizontal axis, while under this plate the target surface is placed, with an adjustable angle. Therefore, as the angle changes, the clearance between starting and ending point of the optical probe changes accordingly. This setup can be seen in Figure 6.11. More details about the experimental setup can be found in [50, 51].

Figure 6.11: Piston pin placed in the experimental setup

The experiment done with piston pin contains three tests with different angles, in order to check if optical interference data collected from the surface of the pin is independent of the angle of incidence of the light. Horizontal distance traveled by probe on the surface of the pin is 13.5 mm. Optical interference (raw) output obtained in these tests are shown in Figure 6.12. In these plots, it can be seen that each test resulted in fringes with higher visibility compared to the previous test. This is due to the fact that as the angle between the plate holding the fiber optic probe and the target surface decreases, the gap between them becomes smaller. This causes an increase in visibility.

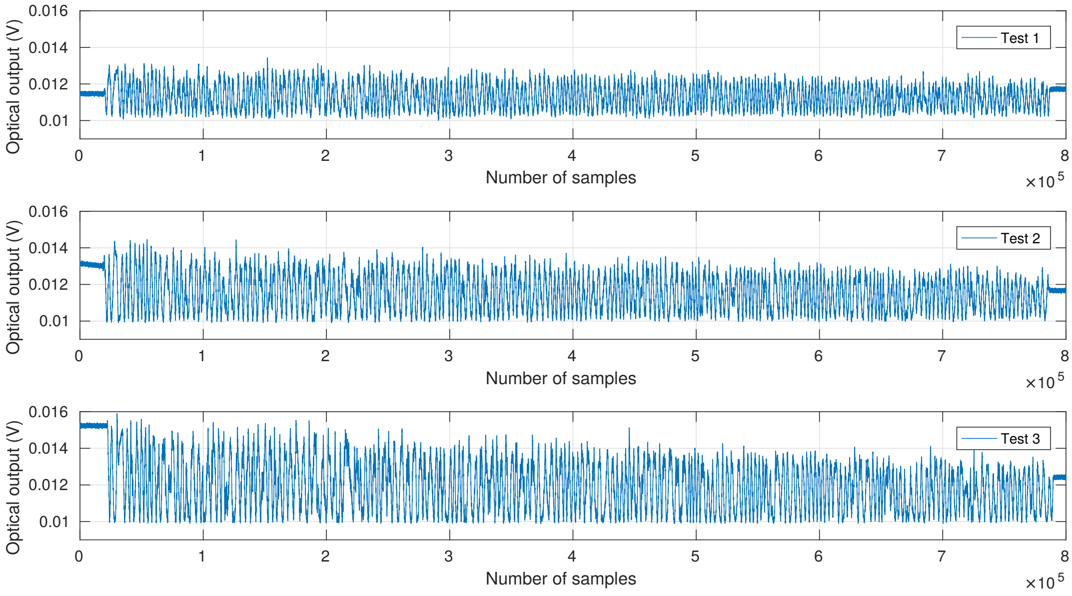

Figure 6.12: *Optical output obtained in pin tests*

After converting these optical data into clearance, following clearance curves are obtained, shown in Figure 6.13.

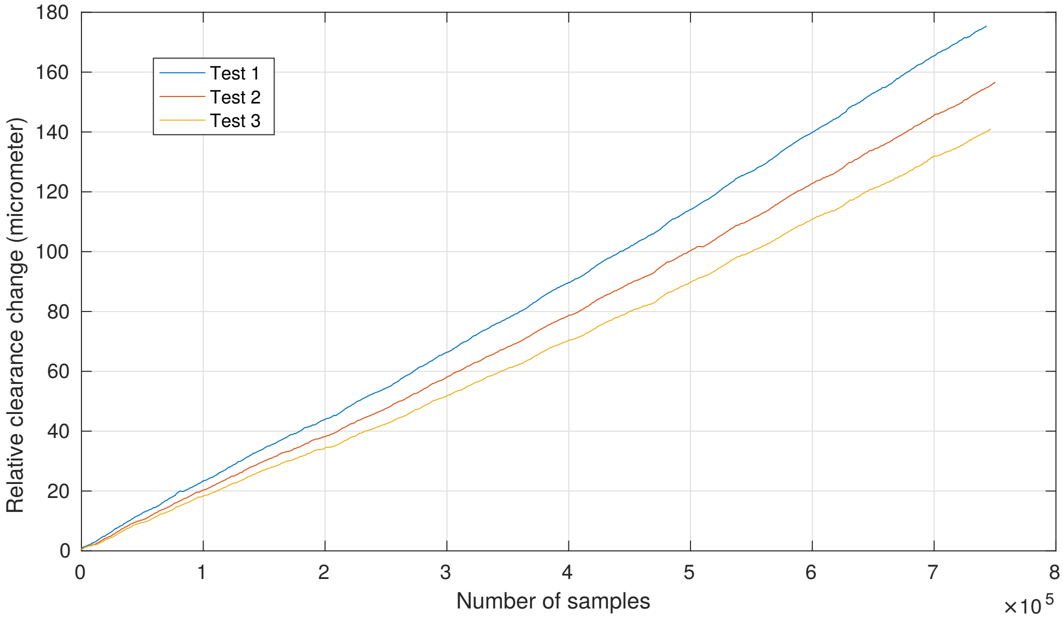

Figure 6.13: *Clearance curve obtained from optical outputs of pin tests*

As expected, clearance curves have different slopes. The last test resulted in the smallest change in relative clearance, as in this test the angle between plate holding the probe and target surface is the smallest. Deviation of these curves from their respective straight line is shown in Figure 6.14.

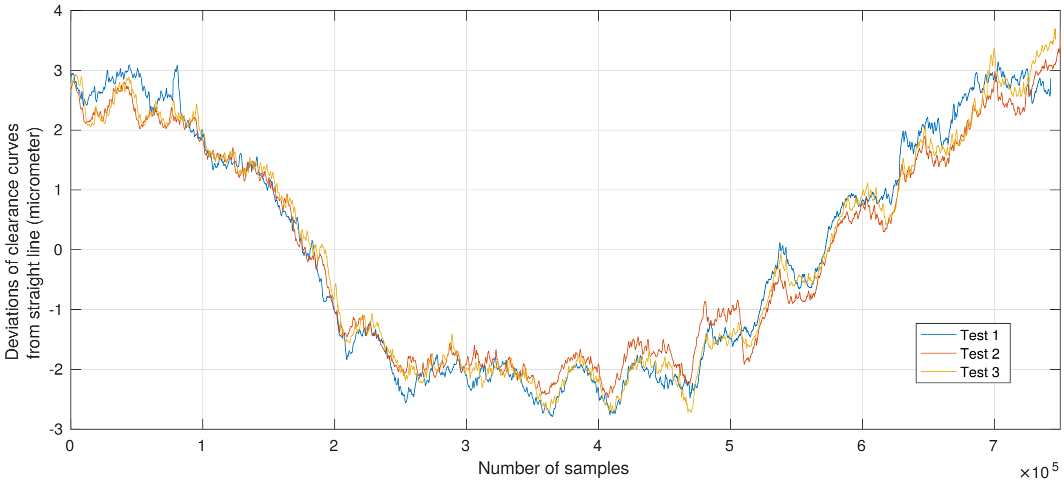

Figure 6.14: *Deviations of clearance curves from straight line*

By observing the results of this experiment, it can be said that any change in angle of the surface with respect to the fiber optic probe does not affect the measurability of the interferometer considerably. This way, it is validated that surface of the piston pin is suitable for interferometric measurements. Also, the surface profile of the piston pin is obtained (given in Appendix C) and in this profilometer data, it can be seen that surface contains approximately 9 peaks for a range of 20 μm. In Appendix B it is shown that if surface contains peaks with a wavelength smaller than approximately 20 μm then they do not affect the interferometric measurement. Further details on the measurability limits of the experimental setup, are given in Appendix B. Bearing shaft has a similar surface roughness to the piston pin, therefore it is concluded that it is possible to obtain optical data from the surface of the bearing shaft as well.

6.2.2 Journal bearing tests without lubricant

After validating that a surface produced with a similar technique with bearing shaft can be used in interferometric measurements, experiments are conducted on the engine-crankshaft assembly. Aims of these tests are: to examine the surface of the shaft, and also to try the algorithm that calculates the trajectory of the shaft during a cycle of the crankshaft, and finally to check the repeatability of measured optical outputs of successive cycles. Presence of lubricant inside bearing dramatically decreases the visibility of the optical output, therefore for the sole purpose of examining the algorithm, to see whether it works or not, preliminary tests were performed without lubricant inside bearing. However, it must be noted that after addition of the lubricant, the behavior of the shaft inside bearing while the crankshaft is rotating will not be the same as when there is no lubricant. In this stage of experiments the suitable sampling rate depending on geometry of the shaft, clearances inside bearing, and rotational speed of the crankshaft is selected.

In order to select a suitable sampling rate for data acquisition, the following methodology is followed: diameter of the bearing shaft is 70 mm, therefore distance scanned by fiber optic probe during a cycle of the crankshaft (i.e., the perimeter of the shaft) is approximately 220 mm. From production specifications of the engine bearing it is known that clearance between the shaft and bearing wall changes between 28-72 μm. Therefore, during an extreme case in one cycle of the crankshaft, the clearance can increase from zero to 72 μm and come back to its original position. A 72 μm clearance change for a beam with wavelength of 1.55 μm is equal to approximately 93 fringes. This means that for a half-cycle of the crankshaft (a distance of 110 mm) maximum number of possible fringes is 93. In order to set the minimum applicable sampling rate, it is required to estimate the minimum number of samples constituting one fringe. The maximum rotational speed of the electric motor is 2.5 rev/s, therefore for this speed, one half-cycle of the crankshaft is traveled in 0.2 sec. If the sampling rate of data acquisition is 10 kS/sec then there will be 21 samples for each fringe. However if the sampling rate is increased to 100 kS/sec, then the minimum number of samples for a fringe is estimated as 210 samples. Applicability of this selection for the sampling rate is further analyzed by looking at the suitable window size for filtering the fringes. A window size larger than the number of data points representing a fringe would smooth out the fringe. A window size smaller than this number would not smooth it out completely, however closer the window size to number of data points of one fringe, lower will be the amplitude of that fringe after filtering.

Selection of a proper window size for smoothing the raw optical data is not a straightforward process. During one revolution of the crankshaft, since the rate of change in clearance does not remain constant, the frequency of the fringes changes. Therefore, finding a suitable window size which can both remove noise, and also fully restore the fringes at their best possible amplitude is not simple. In order to show this, a sample raw optical data is selected. This signal is smoothed with three different window sizes and the resulting smooth signals are compared with the original signal. Considering the limitation to the window size introduced from the analysis above, it is given that maximum window size cannot exceed 200 samples. Therefore three possible window sizes are selected as 30, 100, and 200 samples. In regions with low fringe frequency (Figure 6.15) it can be seen that window size of 200 samples successfully eliminates the random noise and smooths the signal. However, in regions where the fringe frequency is high (Figure 6.16), compared to window sizes of 30 and 100 samples, the window size of 200 samples cannot follow the signal correctly. Window size of 30 samples (especially in regions of low fringe frequency) cannot fully eliminate the random noise effect. Therefore most suitable window size is chosen as 100 samples. This operation is done for different speed levels.

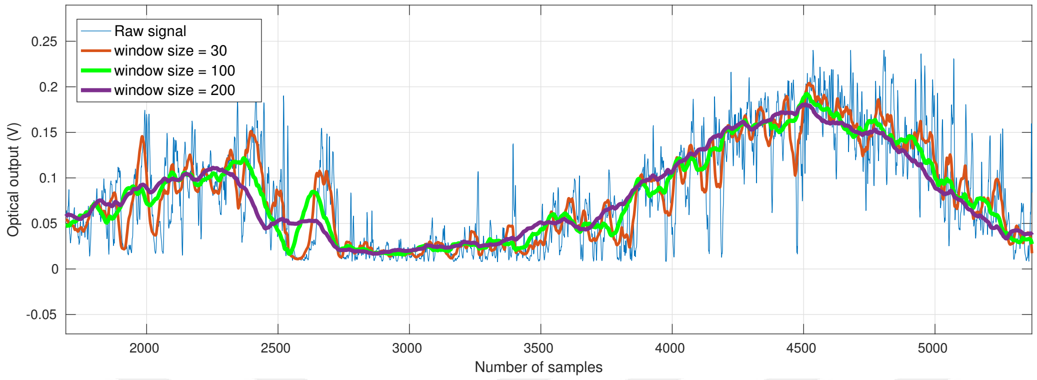

Figure 6.15: *A case when the frequency of fringes is low*

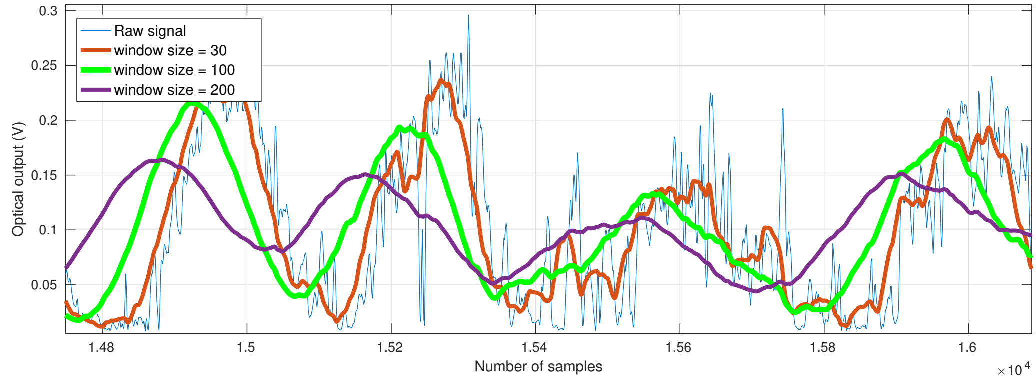

Figure 6.16: *A case when the frequency of fringes is high*

After selection of a suitable window size for filtering the optical output, data analysis process gives a series of estimates on the trajectory of the shaft inside bearing for one cycle of the crankshaft. For this, interference measurements are obtained at four points on the bearing wall. Then these four points are used to generate 5 solutions for the trajectory of the shaft. Locations of the points on the bearing wall with respect to the polar coordinate system introduced in Chapter 5 is shown in Figure 6.17.

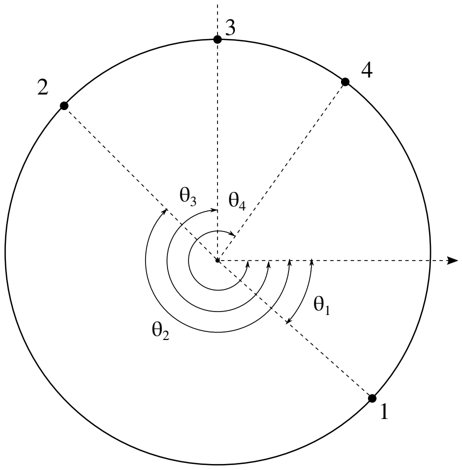

Figure 6.17: *Locations of probes on bearing wall*

Angular positions of the probes are

$\theta_1 = \pi/4$ [rad]

$\theta_2 = 5\pi/4$ [rad]

$\theta_3 = 3\pi/2$ [rad]

$\theta_4 = 3\pi/2 + 50\pi/180$ [rad]

In this coordinate system angular positions of the points are defined from reference line in clockwise direction as shown in Figure 6.17, since crankshaft rotates in clockwise direction. Configuration of fiber optic equipment can be seen in Figure 6.18.

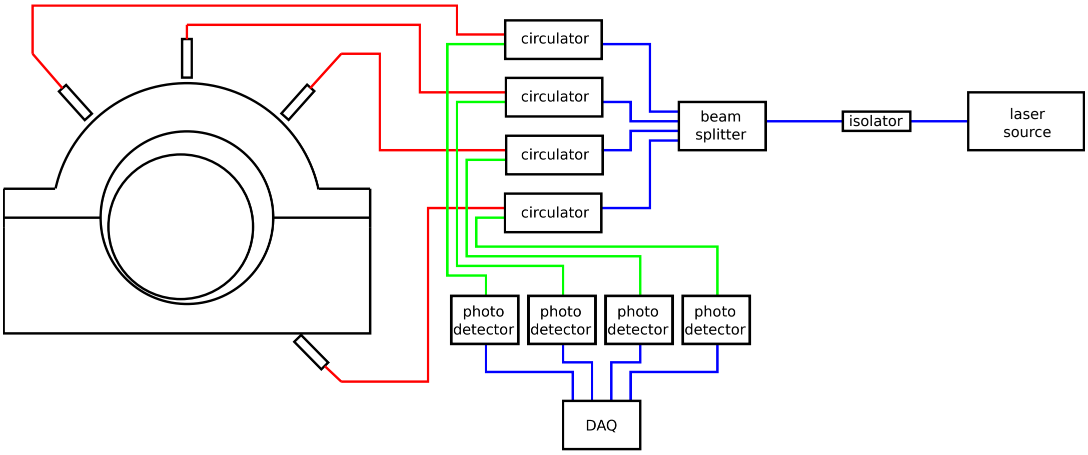

Figure 6.18: *Configuration of the fiber optic equipment for journal bearing experiments*

Optical data collected from four points are used in algorithm as the following pairs: $(1,3)$, $(1,4)$, $(2,3)$, $(2,4)$, $(3,4)$. Probes at locations 1 and 2 are separated from each other with an angle of 180°, therefore, a solution cannot be obtained by using this pair in the algorithm.

As mentioned in Chapter 5, in order to calculate the trajectory from relative clearance changes measured from two points on the bearing wall, initial angular position and absolute clearance value at that position must be known. In order to estimate the initial angular position, the optical data collected from the probe at point 3 is used. It is observed that when the nearest crankpin is at its top position (i.e., coincident with direction of point 3) then shaft either is at an angle of $\pi/2$ or $3\pi/2$ [rad]. For results of analysis presented here initial position is taken as $\pi/2$ [rad]. It is also known that clearance between shaft and bearing wall can change between 0 and nominal radial clearance of bearing. For this analysis, an arbitrary value is selected, since shape of the trajectory is independent of the initial clearance. Optical output of four probes corresponding to one cycle of crankshaft is shown in Figure 6.19.

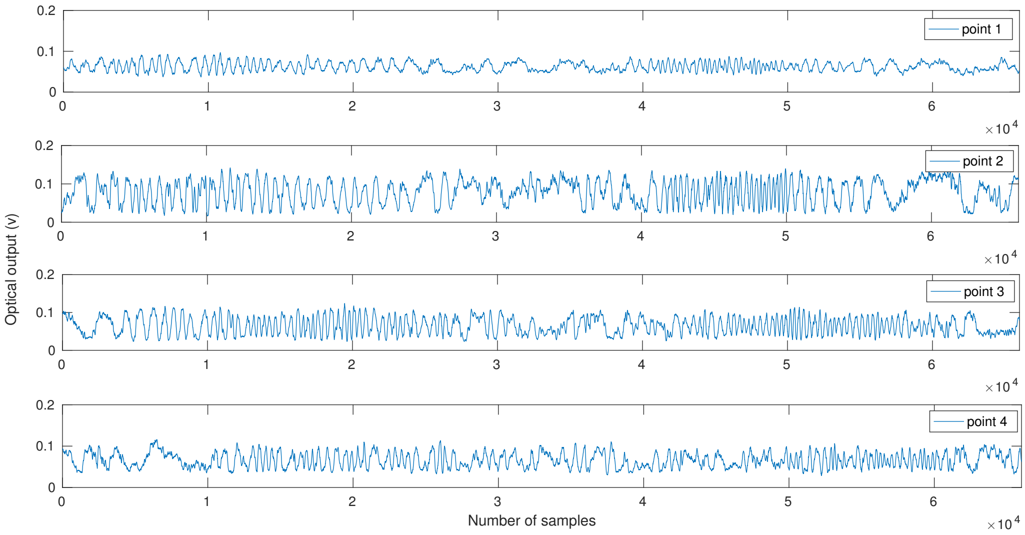

Figure 6.19: *Optical output of probes*

It is expected for a relative clearance curve of a cycle to start from level 0 and come back again to 0. Therefore in an actual clearance curve, there must be at least one stationary point where the curve changes direction. As the stationary point approaches, the absolute value of the slope of the clearance curve decreases, so that at the stationary point it reaches a minimum. In optical outputs this can be seen as a decrease in frequency of the fringes in the vicinity of stationary point. By observing the variation of fringes in a cycle it can be seen that all have two regions where the frequency of the fringes are low. This can also be seen when optical outputs are converted to clearances. This observation is also supported by the sample clearance curves which are produced by simulation and are presented in Chapter 5. These clearance curves change their direction two times in one cycle. However, initially without considering the fact that clearance curve must change its direction at stationary points, optical outputs are all converted to clearance curves as if they are all increasing. These curves are shown in Figure 6.20.

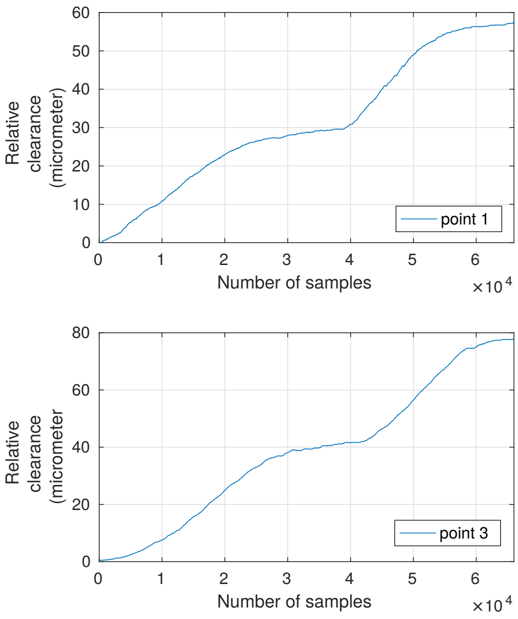

Figure 6.20: *Optical data converted to clearance curves*

Based on the three criteria listed below, these curves are used to generate clearance curves representing the increase/decrease in the curves. These criteria are

- An actual clearance curve must start at 0 and at the end of the curve it must again be at 0, based on the fact that measurements are relative, not absolute.

- At the stationary point of the curve where it changes direction, absolute value of slope of the curve decreases, and after that point the absolute value of slope starts to increase.

- Clearance curves of four points must complement each other, considering their positions. For example, if clearance is decreasing at point 1 then it should increase at point 2 since they are apart from each other at an angle of 180$^{\text{o}}$.

Based on these considerations actual clearance curves are obtained from clearance curves shown in Figure 6.20. These curves are shown in Figure 6.21.

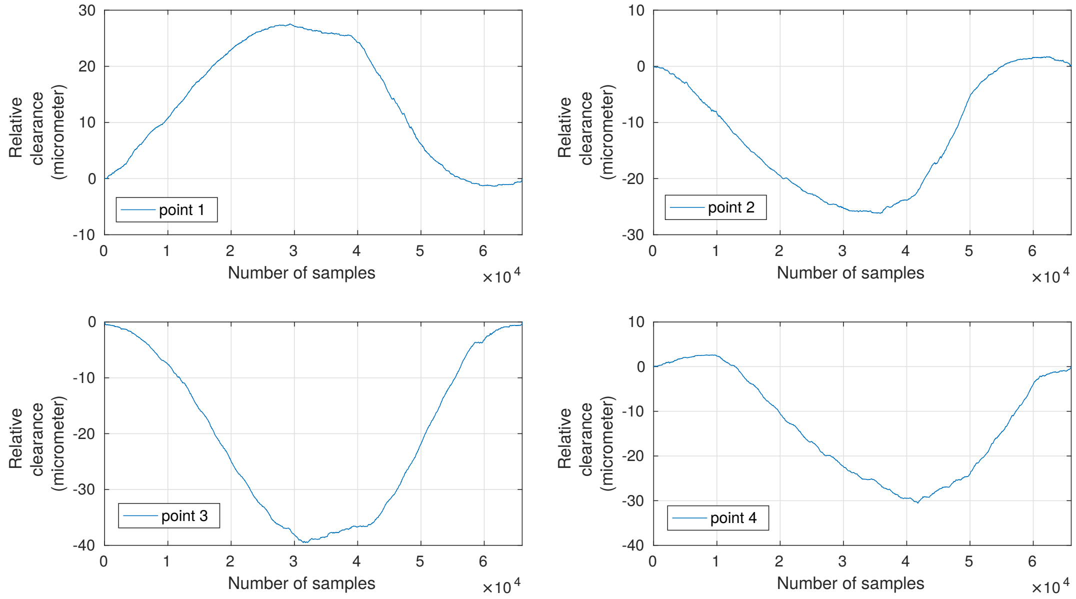

Figure 6.21: *Actual clearance curves*

Estimated trajectory of the shaft center by using clearance curves of probes 1 and 3 is shown in Figure 6.22.

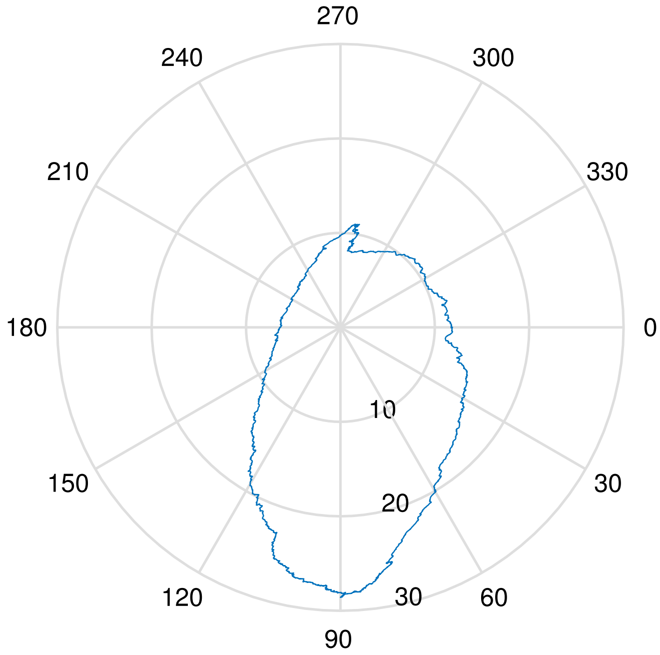

Figure 6.22: *Estimated trajectory using optical output of probes 1 and 3*

Estimated trajectory of the shaft center by using clearance curves of probes 1 and 4 is shown in Figure 6.23.

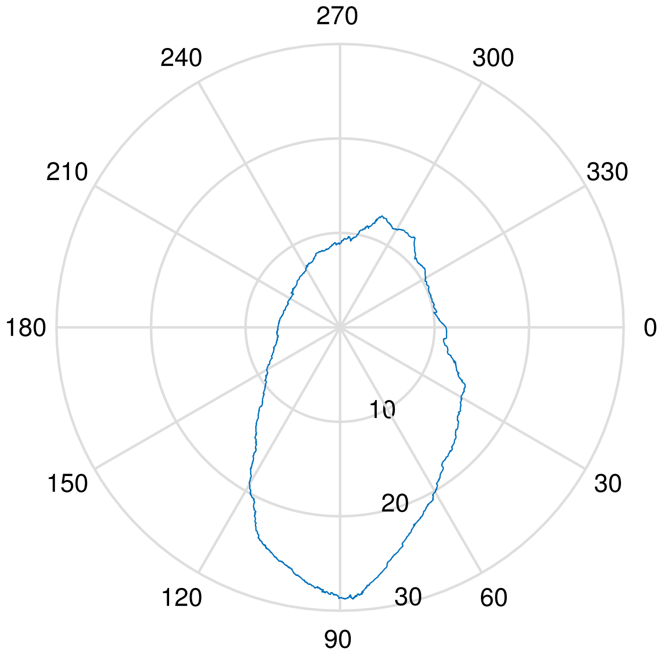

Figure 6.23: *Estimated trajectory using optical output of probes 1 and 4*

Estimated trajectory of the shaft center by using clearance curves of probes 2 and 3 is shown in Figure 6.24.

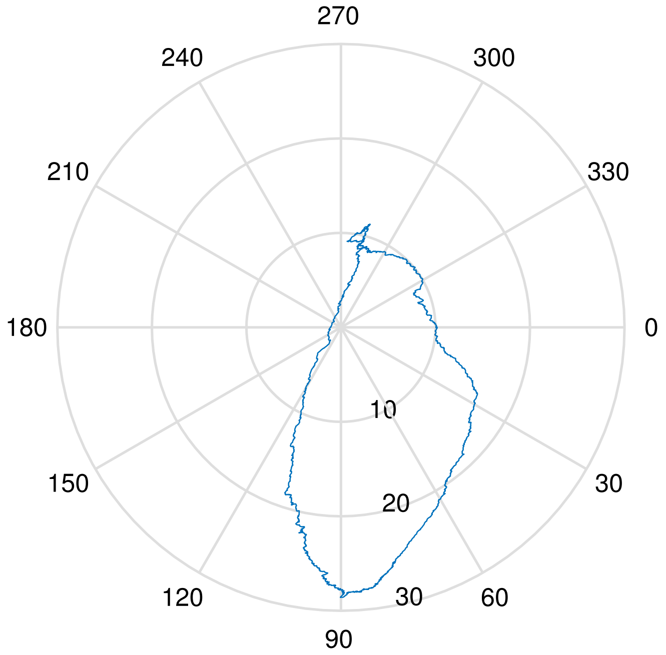

Figure 6.24: *Estimated trajectory using optical output of probes 2 and 3*

Estimated trajectory of the shaft center by using clearance curves of probes 2 and 4 is shown in Figure 6.25.

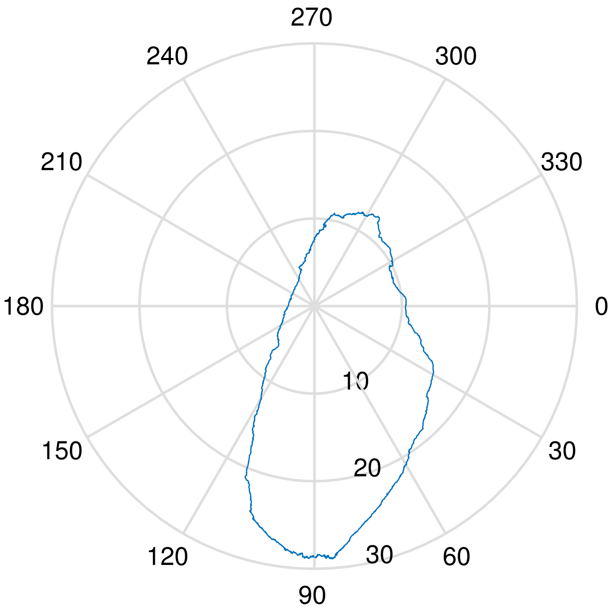

Figure 6.25: *Estimated trajectory using optical output of probes 2 and 4*

Estimated trajectory of the shaft center by using clearance curves of probes 3 and 4 is shown in Figure 6.26.

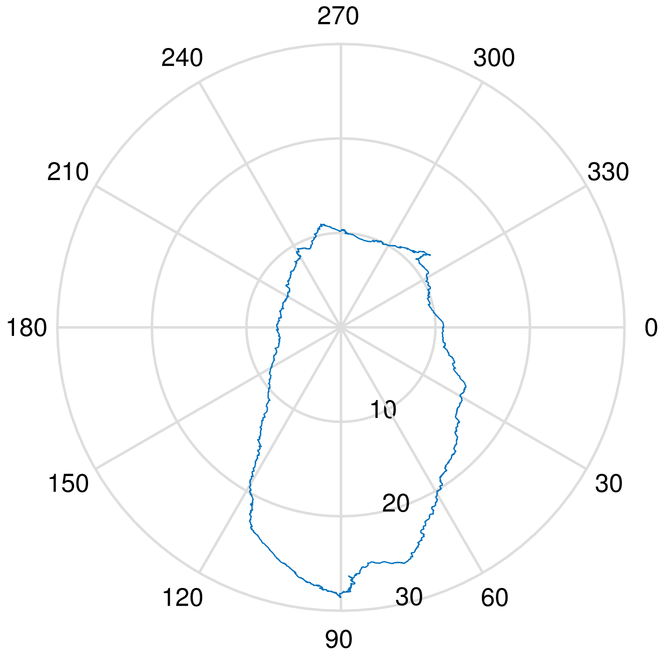

Figure 6.26: *Estimated trajectory using optical output of probes 3 and 4*

All estimated trajectories of the shaft center together are shown in Figure 6.27.

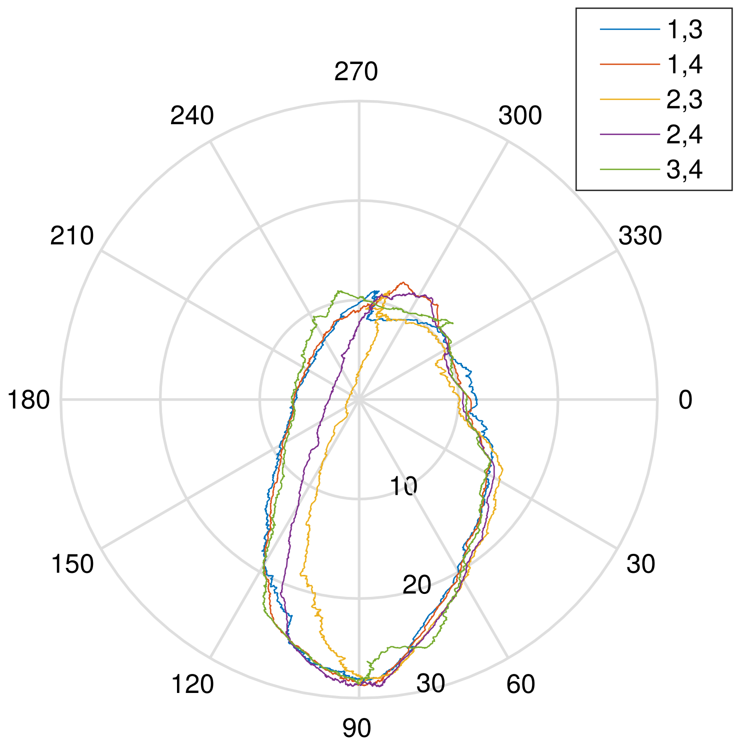

Figure 6.27: *All estimated trajectories*

It can be seen that the trajectories estimated by all pairs with the same initial absolute clearance and angular position values trace similar paths. There are no dominant forces acting on the journal bearing, except the inertia of crankshaft while it is rotating, and gravitational force. Therefore, it is expected that during successive cycles crankshaft follows the same trajectory. The effects of the electric motor on the journal bearing are minimum compared to other main journal bearings, since it is the farthest one from the electric motor. However, still an important factor that can change the trajectory is instabilities in rotation of the electric motor. During long tests, a drop in speed of the electric motor is observed. Also at the very beginning, when the motor starts rotating, it requires time to reach a steady speed. This can be due to motor's own dynamics, the inertia of crankshaft, gravitational force, and also due to the friction inside main journal bearings. This friction is especially high in the bearing subject to the tests, which does not contain any lubricant inside. This assumption is supported by spectral analysis of the optical output, where fringes of stationary points have a higher amplitude at high-frequency regions. This high-amplitude, high-frequency behavior is attributed to the presence of friction between the shaft and bearing wall. In some estimated trajectories a discontinuity is visible near angle 270°, which is one of the stationary points of the shaft. This discontinuity is believed to be due to the following factors: any minor uncertainty present in data acquisition, computational errors while converting optical data to clearance curves, and finally the combination of the errors while two clearance curves are used simultaneously to generate trajectory. Therefore it can be said that these discontinuities are results of uncertainties created by using two individual data simultaneously to generate the trajectory.

6.2.3 Addition of “encoder probe” to the setup

After acquiring signals from probes located at holes of bearing, the optical data must be divided into individual crankshaft cycles. For this, an indicator must be there physically in order to take a reference to divide the signal into cycles. In tests results presented in the previous section, this is done by the knowledge of locations of stationary points in the cycle. However, this method is not accurate and does not result in cycles with exactly equal sample sizes. Therefore one probe was dedicated to work as an encoder probe. It works as a tool to divide the cycles, and it also measures the rotational speed of the crankshaft. Any considerable speed change can be detected easily by looking at the optical data collected from the encoder probe. Working principle of encoder probe is explained in Chapter 4. The probe is located at top of one of the crankpins so that when the crankshaft rotates, during the cycle at some point the surface of that crankpin is very close to the probe, and at that time, optical data becomes maximum. Crankpin at this position can be seen in Figure 6.28.

Figure 6.28: *Crankpin at its closest location to the encoder probe*

Optical output of encoder probe, and optical output of probe located at point 3 at the bearing is shown in Figure 6.29. Peaks of encoder probe can easily be seen in this figure.

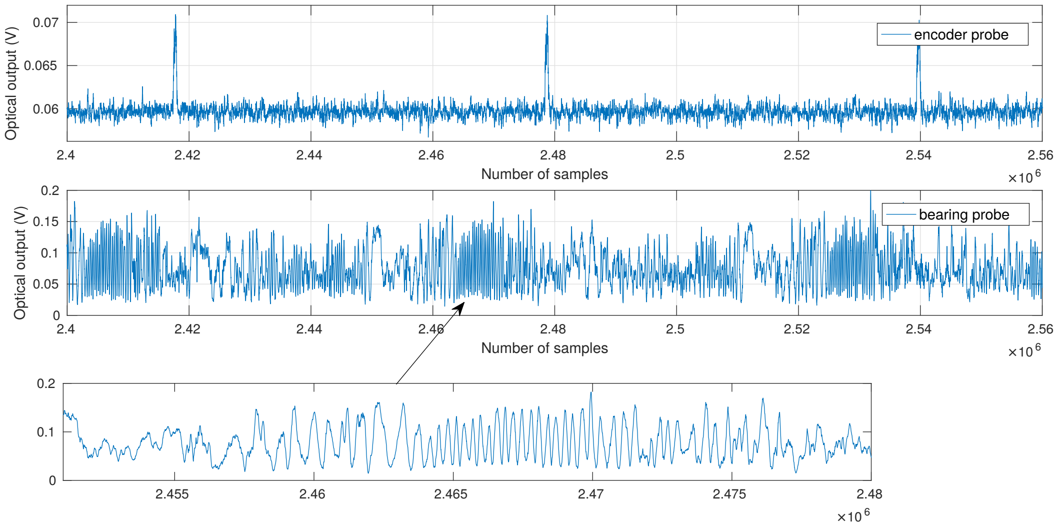

Figure 6.29: *Optical data of encoder probe and a probe located at point 3 on the bearing cap*

In Figure 6.29 it can be seen that optical data obtained from bearing are acceptable to be converted to clearance curve, since distinct fringes can be detected. One peak of encoder probe can also be seen in Figure 6.30. Duration of start and finish of one peak depending on the rotational speed of the electric motor is in order of milliseconds. For the peak shown in Figure 6.30, total number of data points between start and finish of peak is approximately 500, and since sampling rate is 10^2 kS/sec, the duration of one peak is 5 milliseconds. Therefore it is acceptable to use maximum point of this peak as an indicator of starts and finish of every cycle.

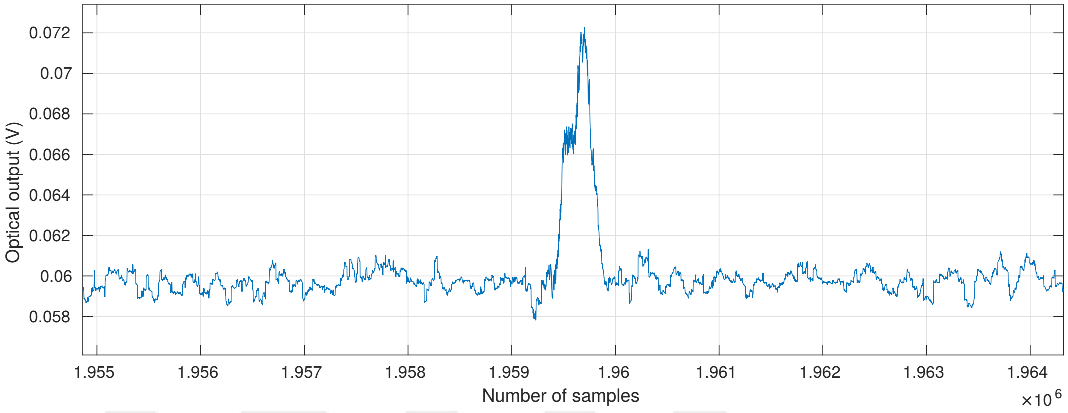

Figure 6.30: *One peak of encoder probe*

6.2.4 Initial tests with lubricated bearing

Next, the lubricant is injected into bearing, and new tests are done. The lubricant used in these tests is Shell Advance SX 2T. Because of the presence of the lubricant, it is expected that the trajectory of the shaft inside bearing may not always be repeatable due to factors such as air packets inside the lubricant, or impurities in it which can further complicate the trajectory. In these tests aim is to observe how certain patterns start to happen in optical data as crankshaft continues to rotate. For this, a series of optical data is acquired from the onset of rotation of the crankshaft. Every data acquisition session has a certain duration, and there is a waiting time between each session. During this waiting time crankshaft continues to rotate at the same speed. In the test presented in this work, duration of each data acquisition session is 40 seconds, and waiting time between each session is 1 minute. The first session is started simultaneously with crankshaft's rotation. Variation of speed during Session 1 is given in Figure 6.31.

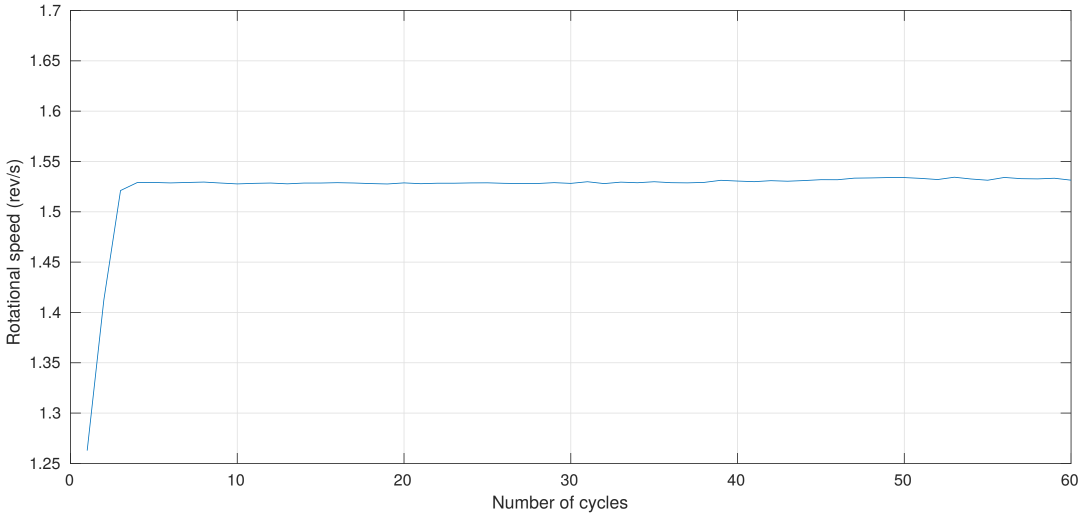

Figure 6.31: *Rotational speed of crankshaft during Session 1*

Variation of speed during Session 2 is given in Figure 6.32.

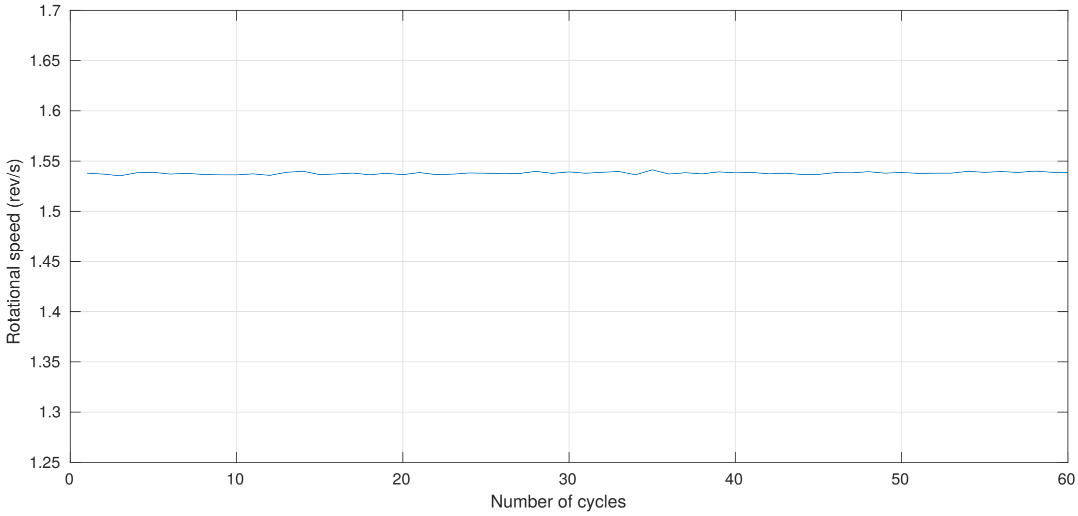

Figure 6.32: *Rotational speed of crankshaft during Session 2*

Variation of speed during Session 3 is given in Figure 6.33.

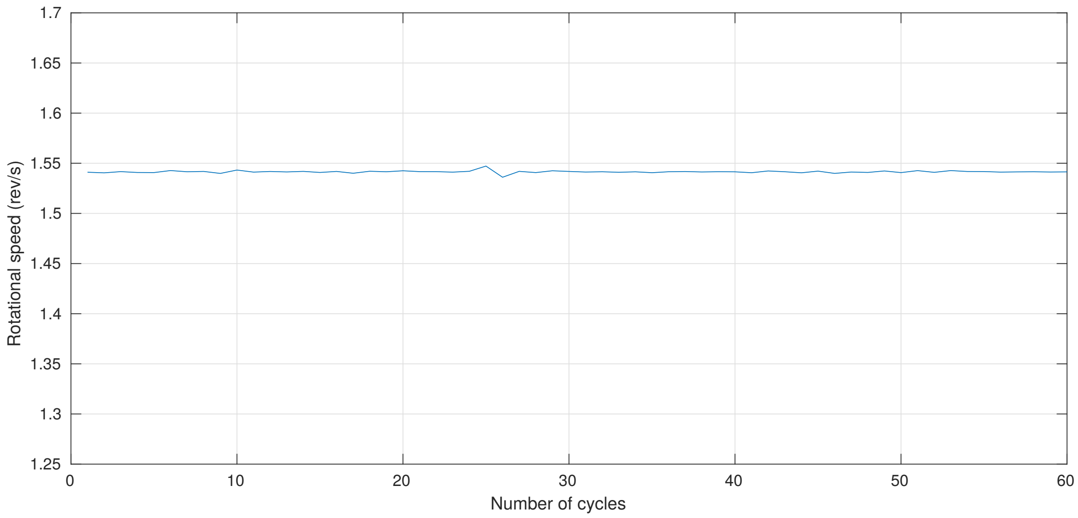

Figure 6.33: *Rotational speed of crankshaft during Session 3*

Variation of speed during Session 4 is given in Figure 6.34.

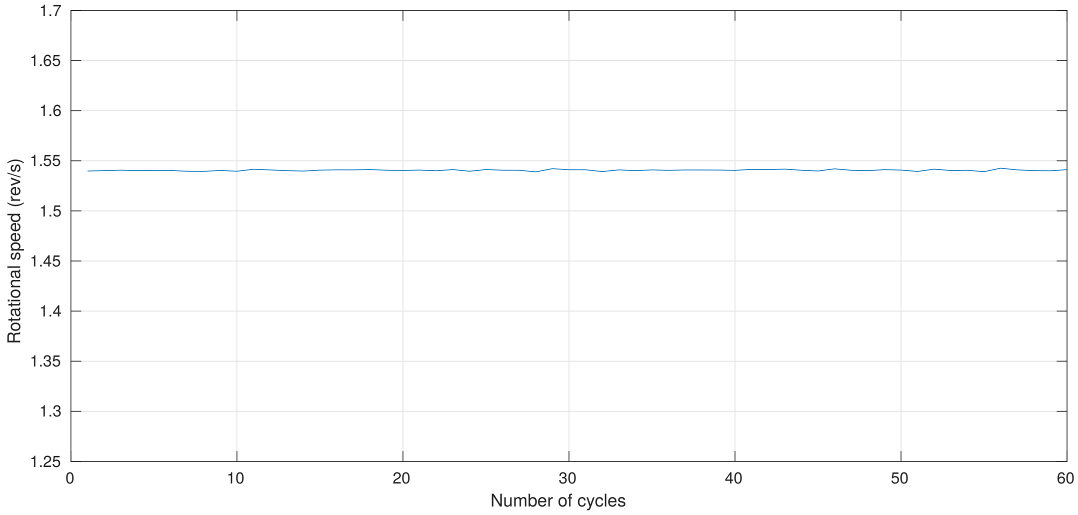

Figure 6.34: *Rotational speed of crankshaft during Session 4*

In order to better observe the changes in speed, curves given in Figures 6.31 to 6.34 are all shown in one plot in Figure 6.35.

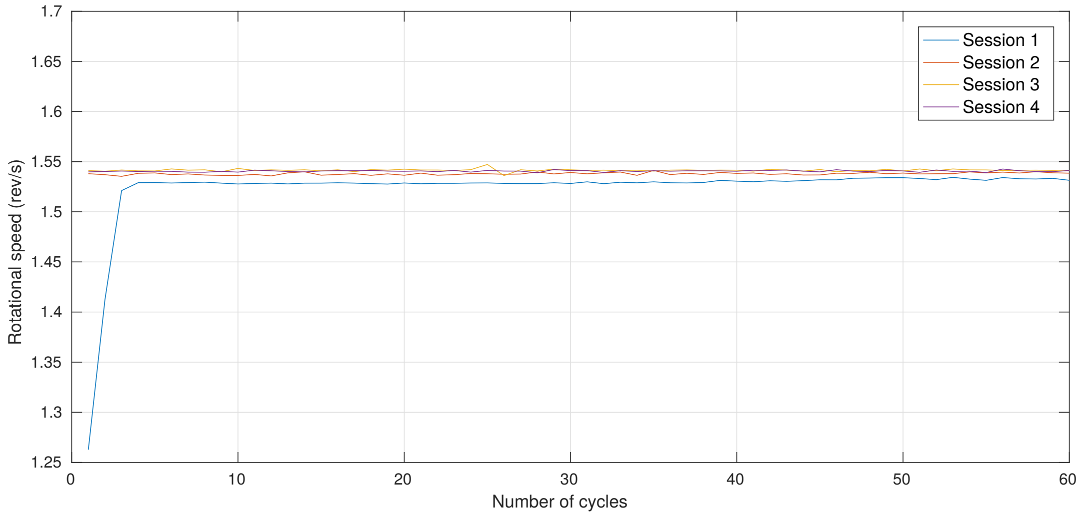

Figure 6.35: Rotational speed of crankshaft during Sessions 1, 2, 3, and 4

It can clearly be seen how speed increases during Session 1. In Session 2 speed continues to increase, but with a lower slope compared to Session 1. Finally speed in Sessions 3 and 4 is a bit higher than speed recorded during Session 2, and it does not increase. Therefore it can be said that after Session 3, and at Session 4 speed has reached a steady-state.

Optical data collected in each session must be investigated to see the effect of transition phase on formation of fringes. In order to do this, optical data corresponding to 10 cycles of crankshaft are presented. For Sessions 1, 2, 3, and 4 sample cycles are shown in Figures 6.36, 6.37, 6.38, 6.39 respectively.

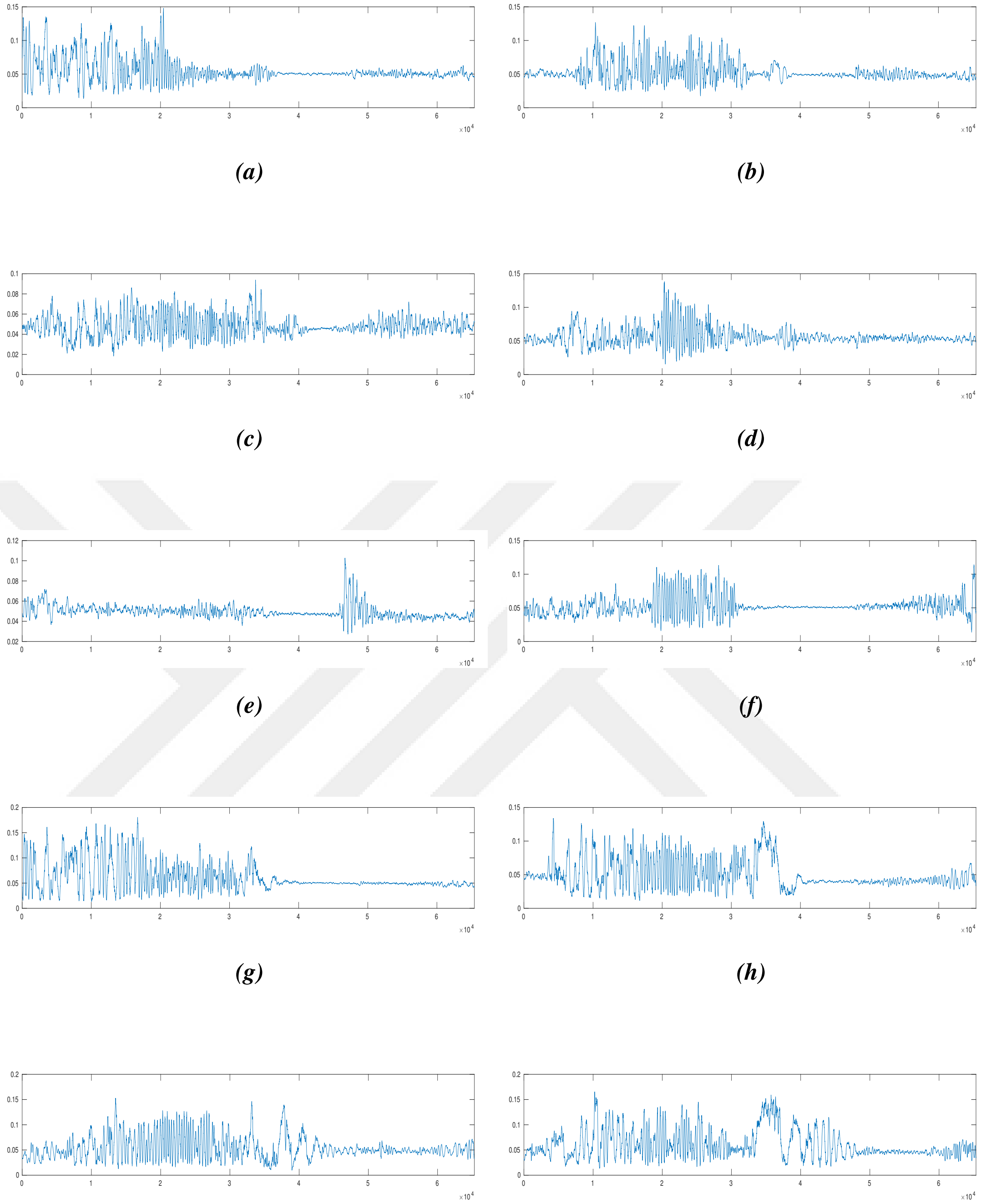

(a) *(b)*

(c) *(d)*

(e) *(f)*

(g) *(h)*

(i) *(j)*

Figure 6.36: 10 *sample optical data from cycles of Session* 1

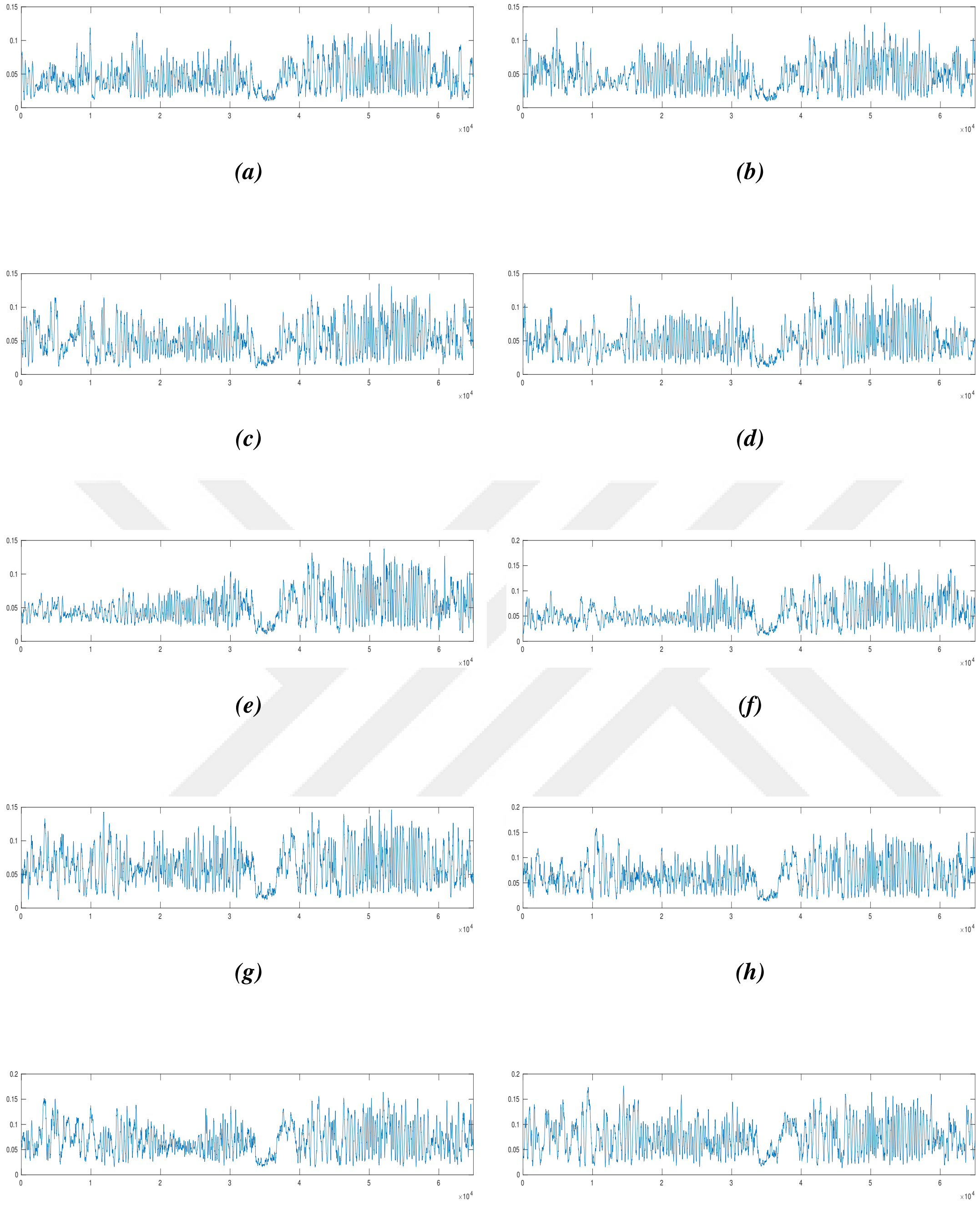

(a) *(b)*

(c) *(d)*

(e) *(f)*

(g) *(h)*

(i) *(j)*

Figure 6.37: 10 *sample optical data from cycles of Session* 2

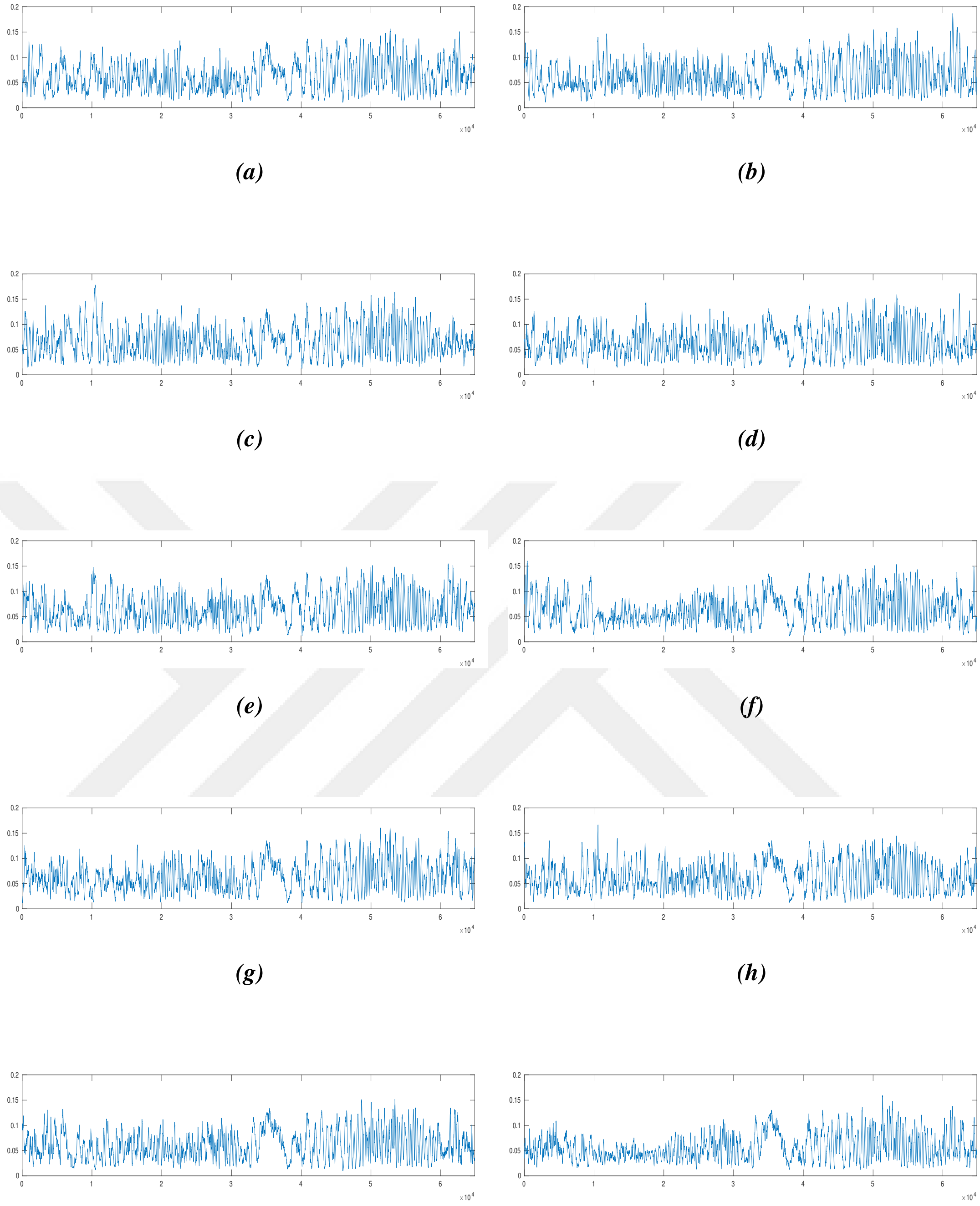

(a) *(b)* *(c)* *(d)* *(e)* *(f)* *(g)* *(h)* *(i)* *(j)*

Figure 6.38: 10 *sample optical data from cycles of Session* 3

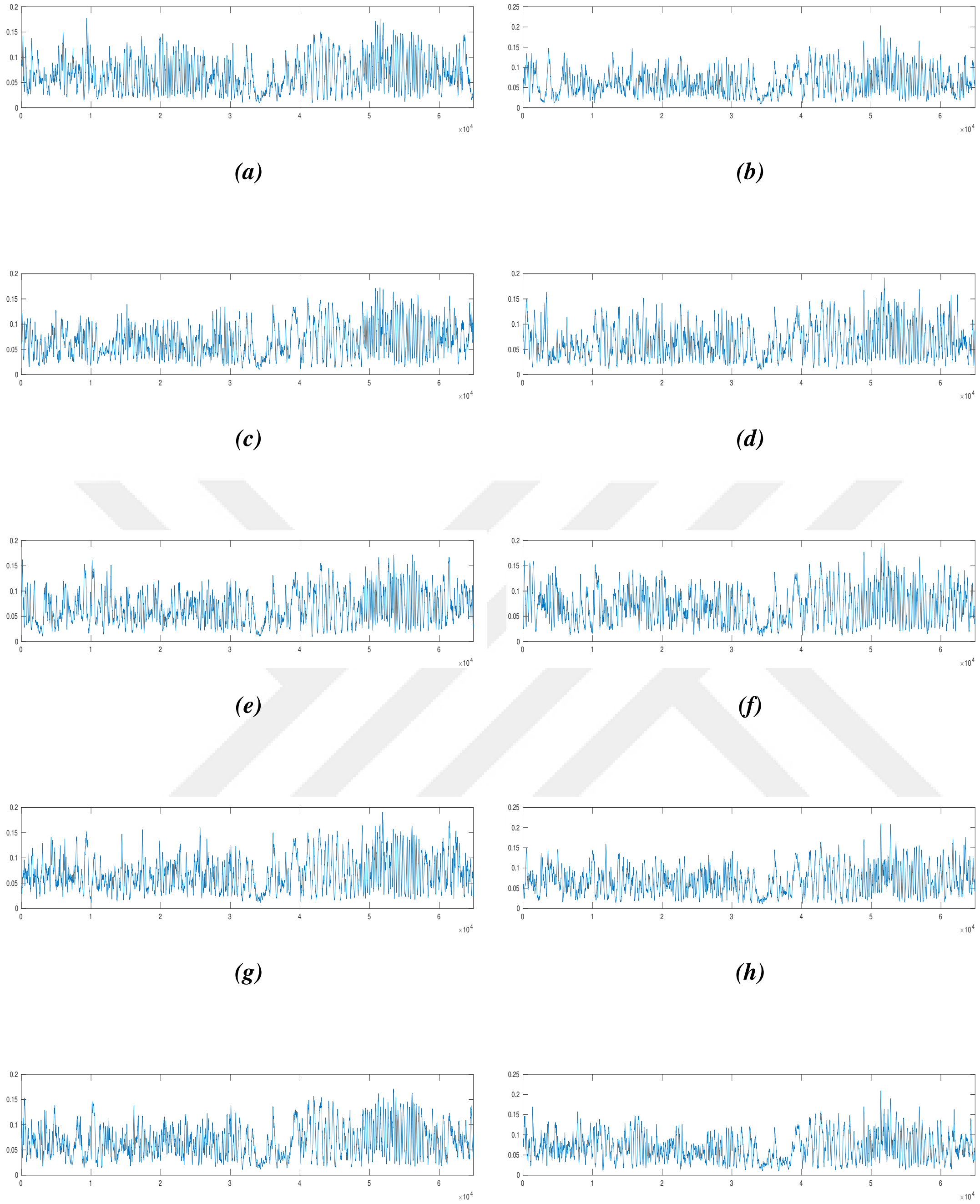

(a) *(b)*

(c) *(d)*

(e) *(f)*

(g) *(h)*

(i) *(j)*

Figure 6.39: 10 *sample optical data from cycles of Session* 4

From these figures the evolution of optical data to a more steady form can be seen, where successive cycles produce very similar fringe patterns. In Session 1, where speed is still increasing, fringe patterns are highly dissimilar in consecutive cycles. This shows that in every cycle, the shaft follows a different trajectory. There are fringes with high amplitudes, and there are fringes with very low amplitudes. These low amplitude fringes can be associated with the shaft not being able to rotate smoothly, and since the speed is low, the effect of the gravitational force acting on the shaft becomes important. This force causes the shaft to rotate mostly at the lower side of the bearing, away from point 3, where the probe is located. From Session 2 to Session 4, optical data of cycles follow more similar patterns, compared to other cycles in their own session. A noticeable similarity happens in the second half of the cycle, where a low-frequency region comes, which is believed to be one of the stationary points where the shaft changes its direction relative to the measurement point. After this region, the fringes have higher amplitudes, which is related to the high irradiance received from interference. This is attributed to the proximity of the surface of the shaft to the probe since it is known that closer the target surface to the probe, higher is the visibility. In this region, the fringes are more recognizable. On the contrary, in the first half of the cycle, fringes have smaller amplitudes and are less recognizable. This is believed to be an indication of the remoteness of the shaft to the probe. Another important point is that the low-frequency region in the second half of the cycle (interpreted to be “stationary point”) coincides with the passage of the closest crankpin to the bearing where measurements are taken from its top position. This situation was expected and was used as a basic assumption in previous analyses.

Optical data of 3 cycles from the same session are converted to clearance curves. These cycles are selected from Session 4. There are 60 cycles in total in this session, and the data of the ones converted to clearance curves are cycles 31, 32, and 33. These clearance curves are shown in Figure 6.40.

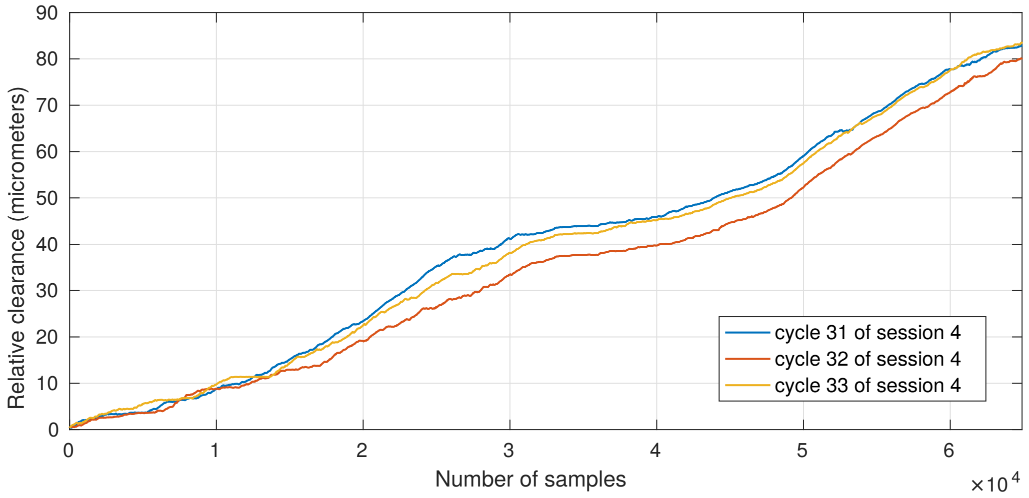

Figure 6.40: *Clearance curves generated by optical data of cycles* 31*,* 32*,* 33 *of Session* 4

In order to get the actual clearance curves, with increasing/decreasing trends, stationary points must be detected. Based on selection criteria, defined previously, the points shown in Figure 6.41 are selected.

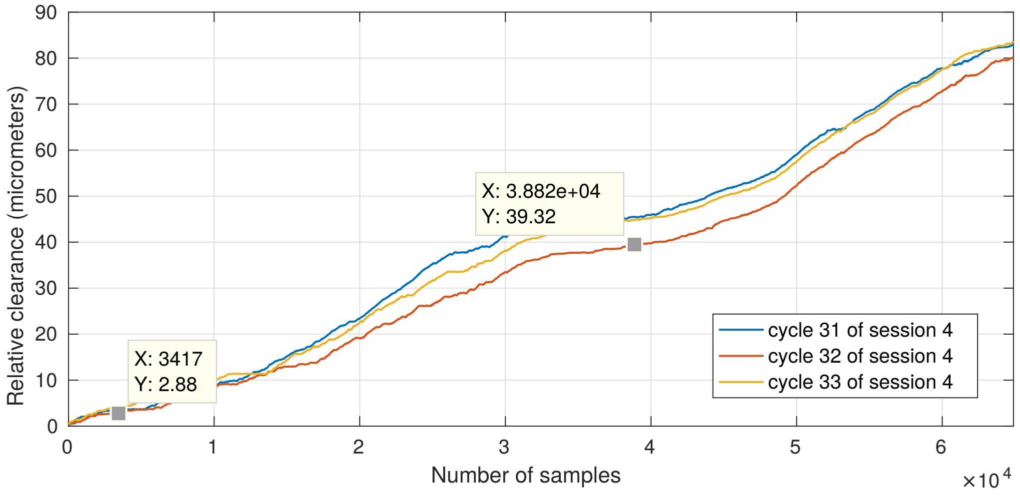

Figure 6.41: *Selection of stationary points of clearance curves*

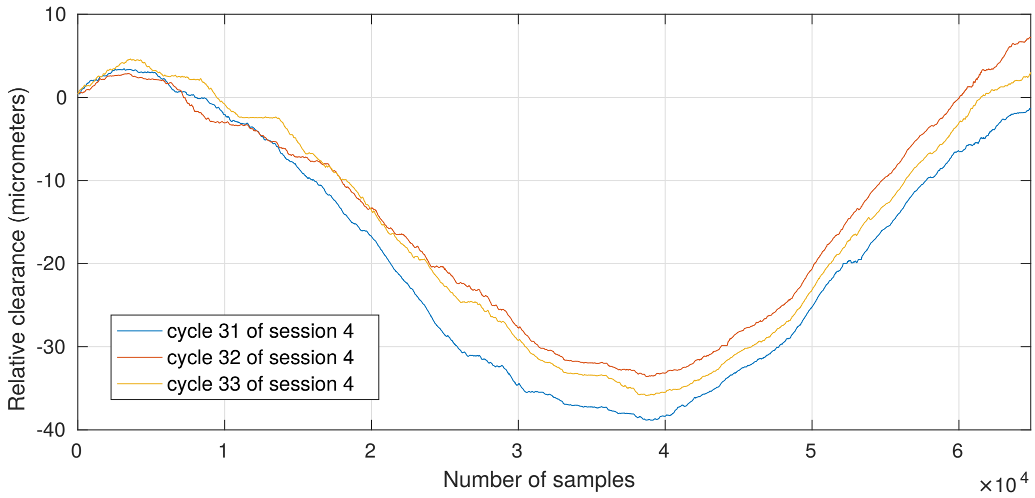

Figure 6.42: *Actual clearance curves*

As it can be seen, at the end of the cycle total deviation from zero is less than 10 μm. These deviations can be due to several reasons. One of the most important of them is the visibility of fringes. Presence of lubricant decreases the visibility and makes the task of detection of fringes harder.

6.3 Trajectory estimation for different rotational speeds

In this section, the tests done in the preliminary stage of the experiment are performed in more depth. 3 different set of tests are performed, where the electric motor is rotating at 3 different speeds. These 3 different speed levels are named as: “slow speed”, “medium speed”, and “high speed”. For each speed, 4 data acquisition sessions are performed. Duration of each session is 1 minute, with 1 minute waiting time between each. Finally, for each rotational speed level, two simultaneous cycles from two points on the bearing are selected to generate the estimated trajectory. Here, pairs of optical data acquired for three successive cycles are selected for each speed level and are converted into trajectory. The aim of estimating the trajectory of three successive cycles for each speed level is both to show the ability of the algorithm to give consistent results, and to also show the credibility of interferometric measurement technique in giving acceptable results even in presence of the lubricant. Also effect of rotational speed on trajectory of the shaft is sought.

Two points in which optic probes are located are points 2, and 3. As shown in Figure 6.17, with respect to the reference direction, these points are located at angles $(5\pi/4)$ and $(3\pi/2)$, respectively.

The inertia force acting on bearing can be approximated with the equation

$$F = k \times \frac{v^2/r}{g} \tag{6.1}$$

Where k is a constant which represents the effect of the equivalent mass of the crankshaft, v is the speed of the crankshaft, r is the radius of center of gravity, and g is the gravitational acceleration. From this equation it can be seen that an increase in speed will affect the force acting on the bearing with its square.

6.3.1 Slow speed

The mean speed in these tests is approximately 1.0 rev/sec. The optical data acquired from points 2 and 3 for the first cycle are shown in Figure 6.43.

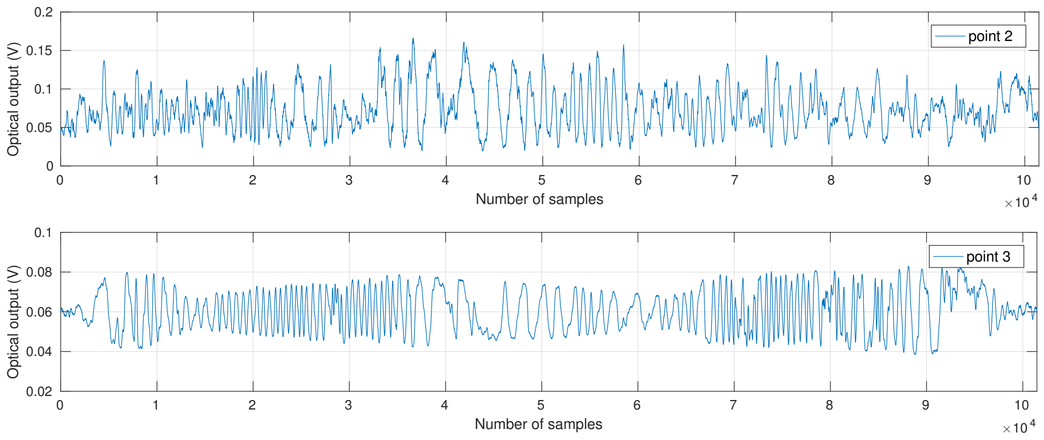

Figure 6.43: *Optical data of probes at points 2 and 3, for cycle 1, at slow speed*

The resulting trajectory obtained using the above optical data is shown in Figure 6.44.

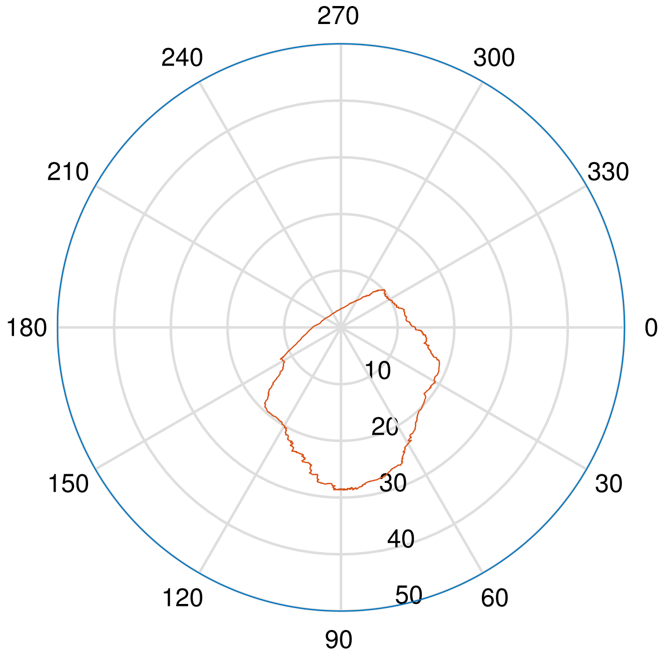

Figure 6.44: *Trajectory generated using optical data of probes at points 2 and 3, for cycle 1, at slow speed*

The optical data acquired from points 2 and 3 for the second cycle are shown in Figure 6.45.

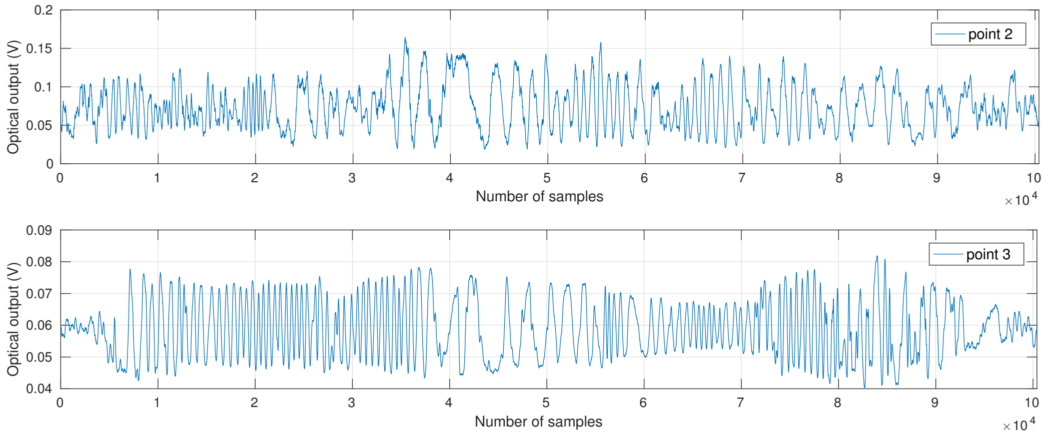

Figure 6.45: *Optical data of probes at points 2 and 3, for cycle 2, at slow speed*

The resulting trajectory obtained using the above optical data is shown in Figure 6.46.

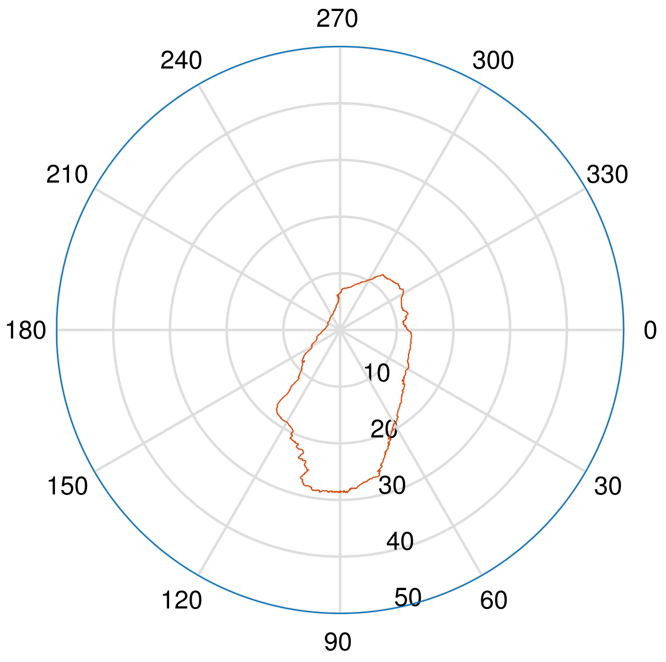

Figure 6.46: *Trajectory generated using optical data of probes at points 2 and 3, for cycle 2, at slow speed*

The optical data acquired from points 2 and 3 for the third cycle are shown in Figure 6.47.

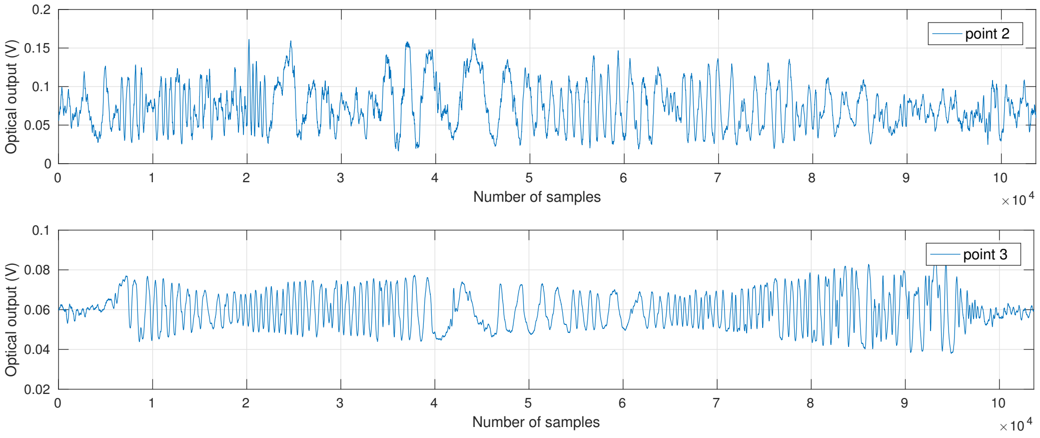

Figure 6.47: *Optical data of probes at points 2 and 3, for cycle 3, at slow speed*

The resulting trajectory obtained using the above optical data is shown in Figure 6.48.

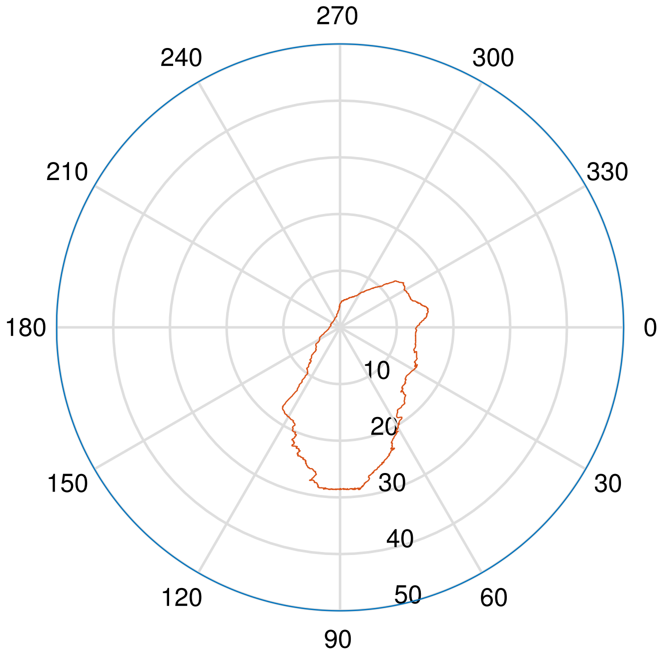

Figure 6.48: *Trajectory generated using optical data of probes at points 2 and 3, for cycle 3, at slow speed*

The successive trajectories can all be seen in Figure 6.49.

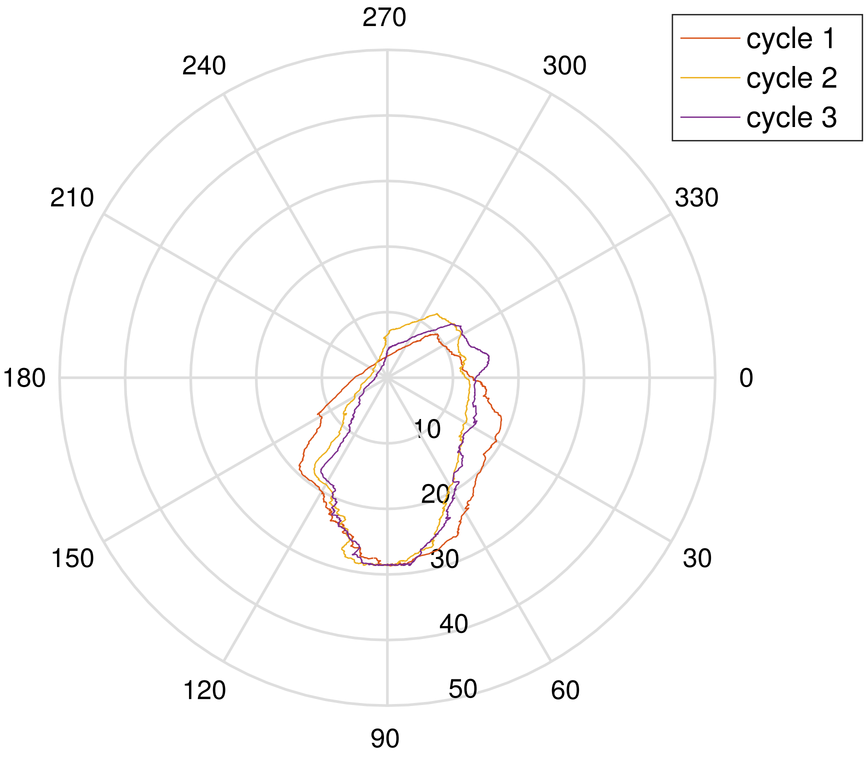

Figure 6.49: *All successive trajectories for different cycles, at slow speed*

6.3.2 Medium speed

The mean speed in these tests is approximately 1.6 rev/sec. The optical data acquired from points 2 and 3 for the first cycle are shown in Figure 6.50.

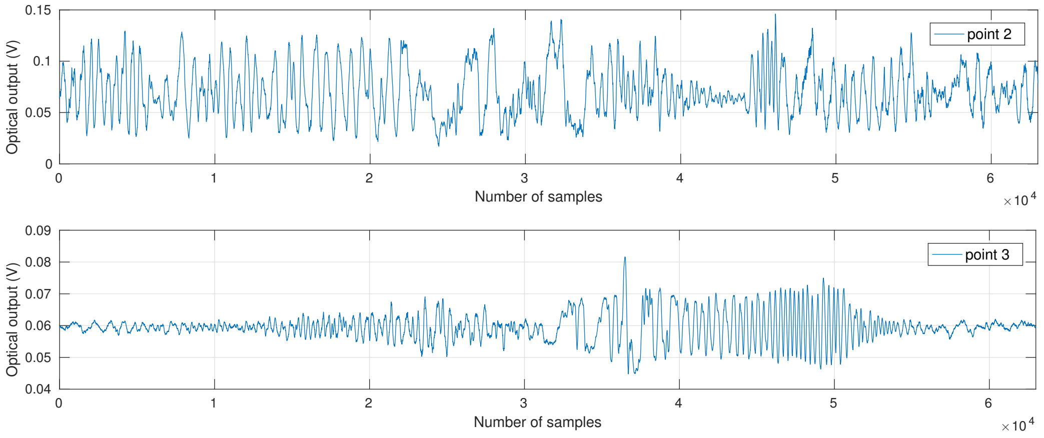

Figure 6.50: *Optical data of probes at points 2 and 3, for cycle 1, at medium speed*

The resulting trajectory obtained using the above optical data is shown in Figure 6.51.

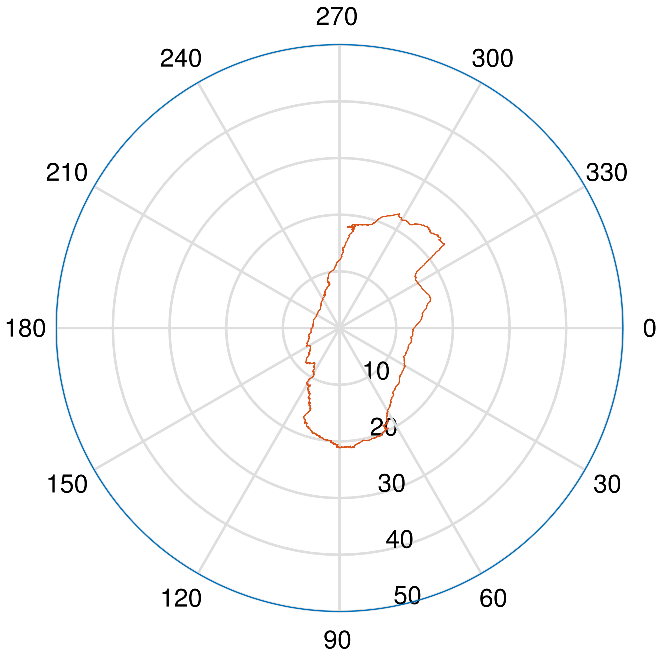

Figure 6.51: *Trajectory generated using optical data of probes at points 2 and 3, for cycle 1, at medium speed*

The optical data acquired from points 2 and 3 for the second cycle are shown in Figure 6.52.

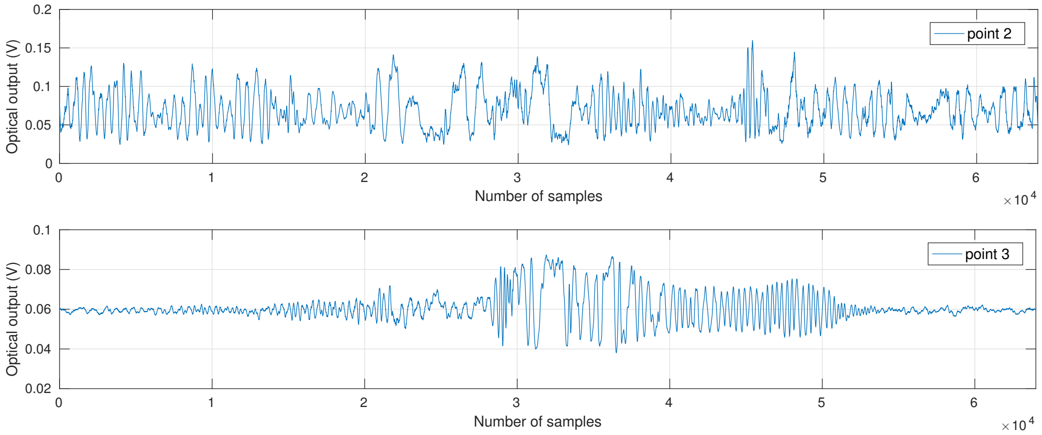

Figure 6.52: *Optical data of probes at points 2 and 3, for cycle 2, at medium speed*

The resulting trajectory obtained using the above optical data is shown in Figure 6.53.

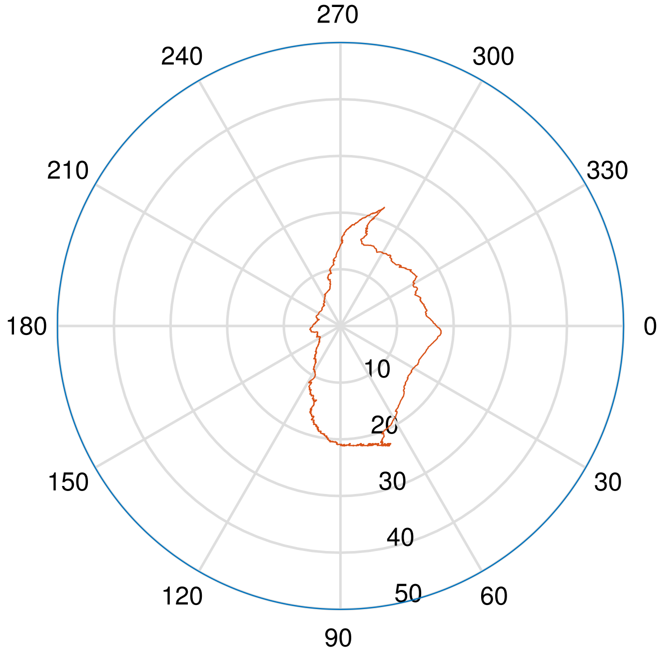

Figure 6.53: *Trajectory generated using optical data of probes at points 2 and 3, for cycle 2, at medium speed*

The optical data acquired from points 2 and 3 for the third cycle are shown in Figure 6.54.

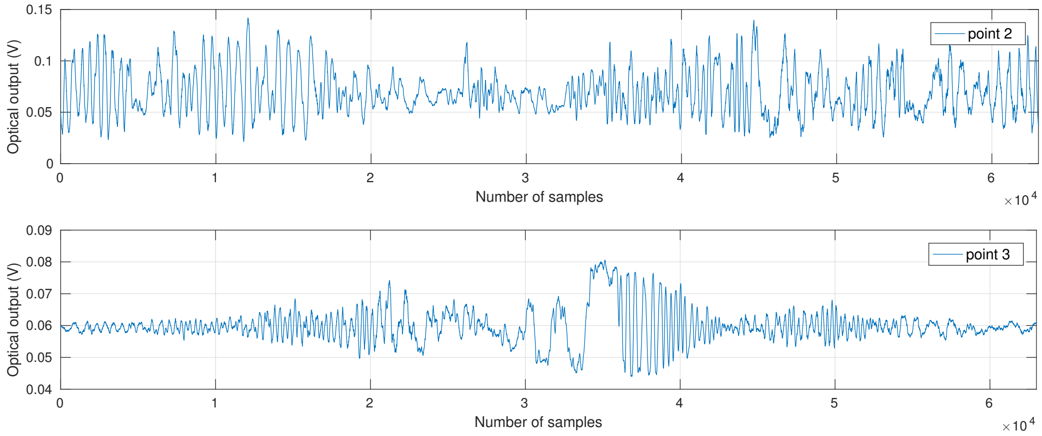

Figure 6.54: *Optical data of probes at points 2 and 3, for cycle 3, at medium speed*

The resulting trajectory obtained using the above optical data is shown in Figure 6.55.

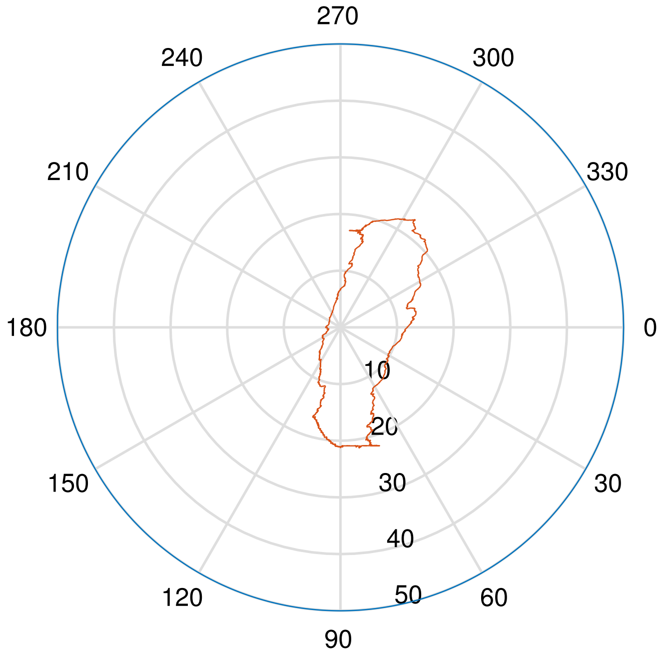

Figure 6.55: *Trajectory generated using optical data of probes at points 2 and 3, for cycle 3, at medium speed*

The successive trajectories can all be seen in Figure 6.56.

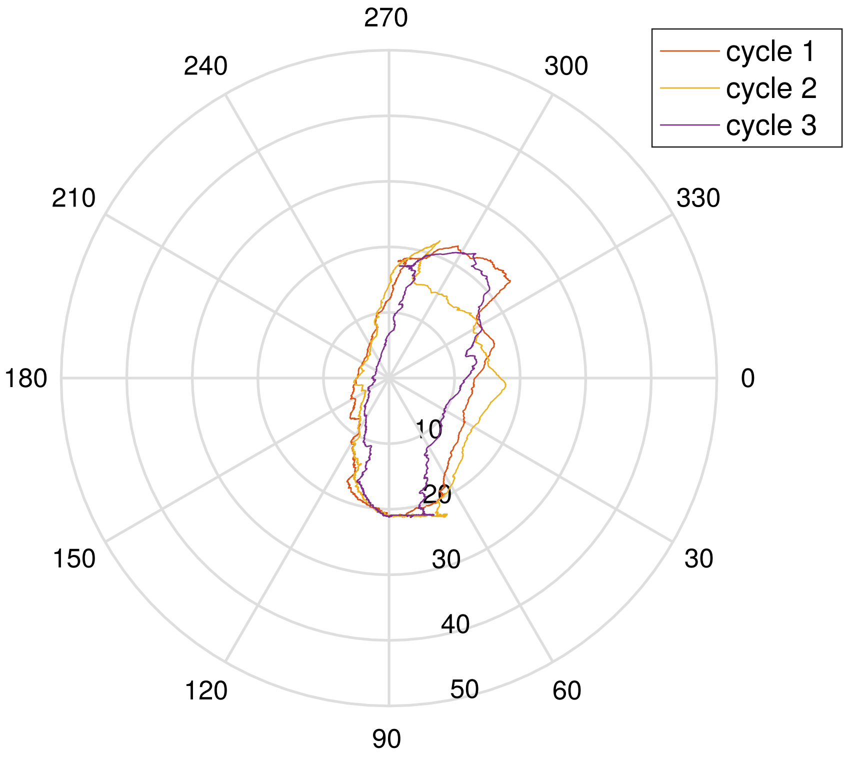

Figure 6.56: *All successive trajectories for different cycles, at medium speed*

6.3.3 High speed

The mean speed in these tests is approximately 2.3 rev/sec. The optical data acquired from points 2 and 3 for the first cycle are shown in Figure 6.57.

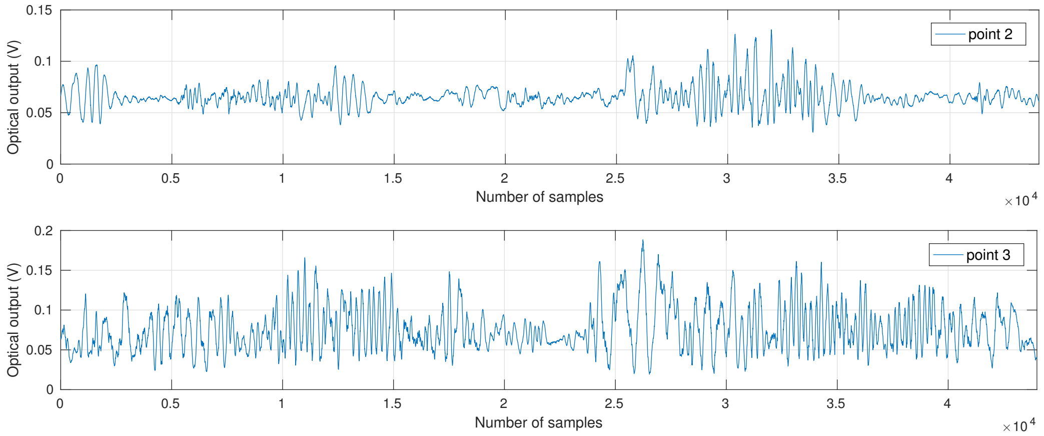

Figure 6.57: *Optical data of probes at points 2 and 3, for cycle 1, at high speed*

The resulting trajectory obtained using the above optical data is shown in Figure 6.58.

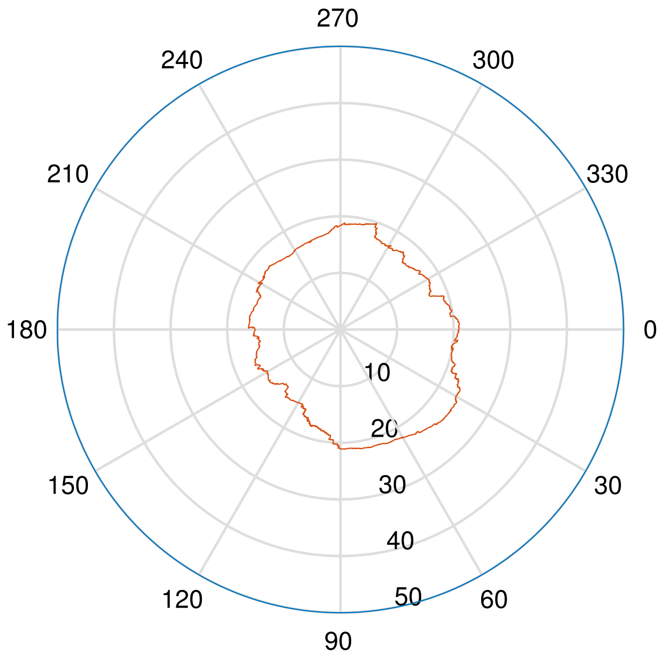

Figure 6.58: *Trajectory generated using optical data of probes at points 2 and 3, for cycle 1, at high speed*

The optical data acquired from points 2 and 3 for the second cycle are shown in Figure 6.59.

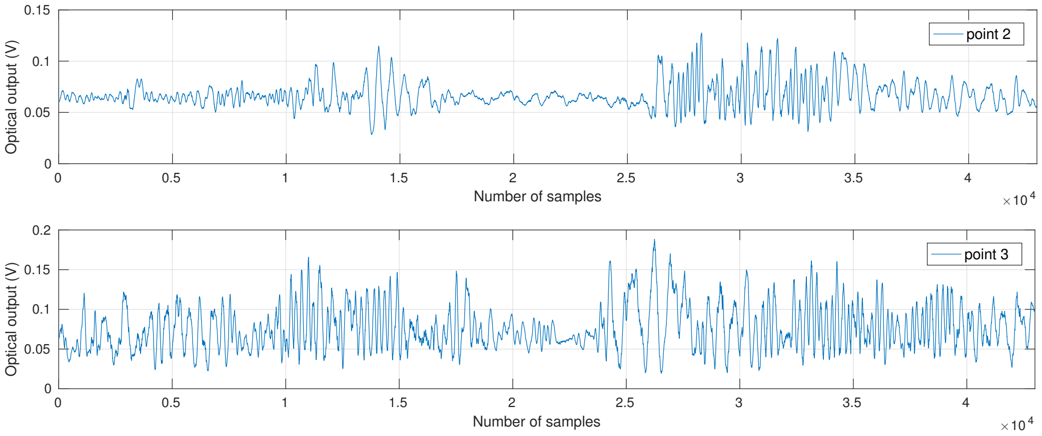

Figure 6.59: *Optical data of probes at points 2 and 3, for cycle 2, at high speed*

The resulting trajectory obtained using the above optical data is shown in Figure 6.60.

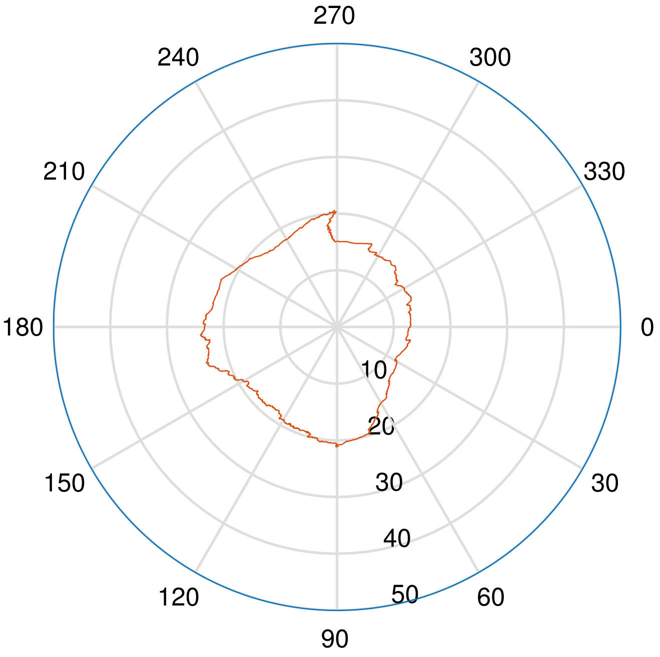

Figure 6.60: *Trajectory generated using optical data of probes at points 2 and 3, for cycle 2, at high speed*

The optical data acquired from points 2 and 3 for the third cycle are shown in Figure 6.61.

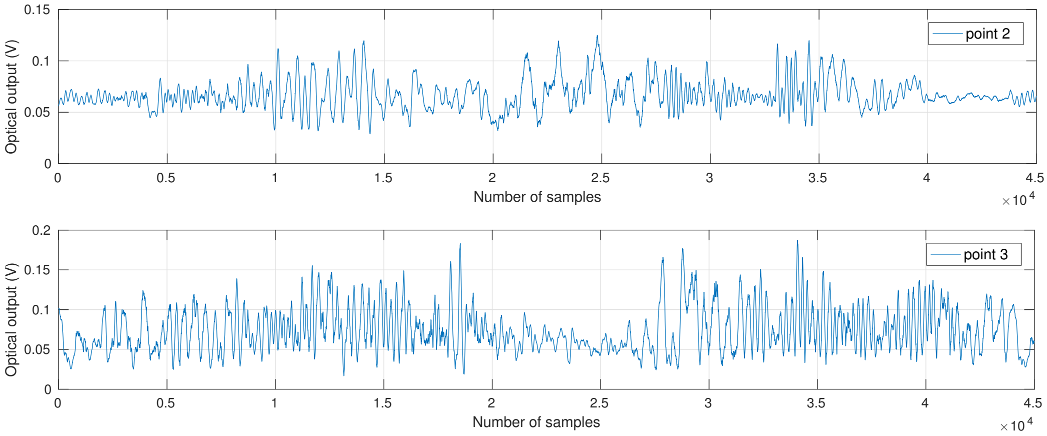

Figure 6.61: *Optical data of probes at points 2 and 3, for cycle 3, at high speed*

The resulting trajectory obtained using the above optical data is shown in Figure 6.62.

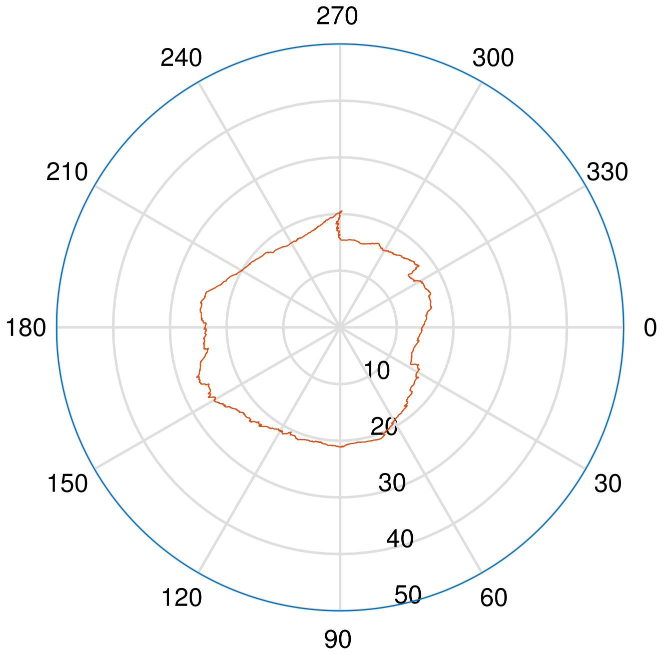

Figure 6.62: *Trajectory generated using optical data of probes at points 2 and 3, for cycle 3, at high speed*

The successive trajectories can all be seen in Figure 6.63.

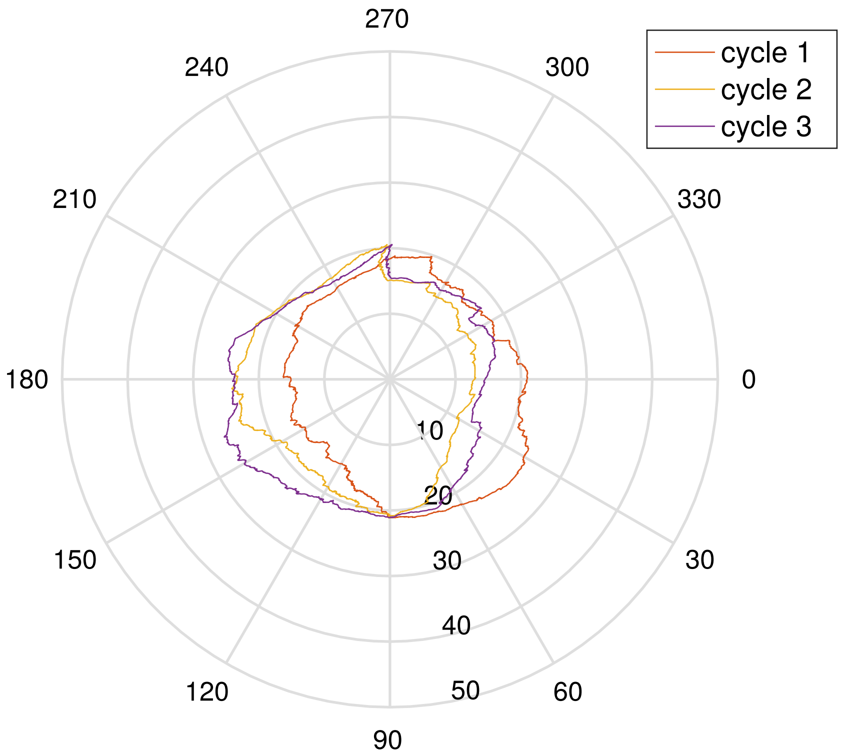

Figure 6.63: *All successive trajectories for different cycles, at high speed*

6.3.4 Discussion

Although there is lubricant inside the bearing, optical data acquired from probes have distinguishable fringes. However, there are still regions in signals where it is difficult to detect fringes. These difficulties result in errors, and deviations (although small, less than 10%) in the trajectories, as will be mentioned below. Two stationary regions in every cycle can easily be detected in the signals, especially when optical data are converted into clearance curves. Locations of these stationary regions in two measurement points complement each other, which also approves the measurement technique. However, in these stationary points, selecting the exact point when the clearance starts to decrease (or vice versa) requires a more delicate work. This is another source of error in estimating the trajectories. Criteria to select these points properly are given previously in this work. It must be noted that previous errors (such as errors made in counting the number of fringes) affect the process of selecting the stationary points, and this also adds more errors to the task.

In an actual crankshaft, there are two load sources: one is due to the inertia of rotating mechanical parts of the engine, and the other is due to gas combustion in the cylinder. In this work, the crankshaft is not connected to cylinders and connecting rods. Therefore the only loads acting on the crankshaft are inertia due to rotation of crankpins of the crankshaft, and gravitational force. Load due to the inertia is directly related to square of rotational speed and increases with engine speed. In high rotational speeds the gravitational force is negligibly small, however in this work, since crankshaft is rotated at slow speeds compared to the actual working speed of the engine, the effect of gravity is important. Having trajectory estimates for 3 different speed levels, the effect of the combination of inertia and the gravitational force on the bearing can be investigated. The bearing subject to tests is farthest from the electric motor, therefore it is assumed that any unwanted effect due to the electric motor, such as misalignment, is negligible. Trajectories of successive cycles at slow speed test (shown in Figure 6.49) have similar shapes. They have the shape of an ellipse, with vertices in the vertical direction. The reason for this shape is attributed to the effect of gravitational acceleration. The distance between two vertices of the ellipse is approximately 40 μm. There are deviations between trajectories of successive cycles, which do not exceed 5 μm. These deviations can either be due to an actual change in the trajectory of the bearing, or small errors in counting the number of fringes of optical data while converting them to clearance curve. A 5 μm deviation corresponds to approximately 6 fringes, since every fringe corresponds to a relative clearance change of 0.78 μm. In every cycle and optical data acquired from one point is composed of approximately 90-110 fringes, and the presence of lubricant in the media between the optical probe and target surface reduces the visibility, therefore this amount of error is regarded to be acceptable. Trajectories obtained at medium speed level (shown in Figure 6.56) have a more elliptical shape than those of slow speed level. The distance between vertices of the ellipse is more than 40 μm and is believed to be due to a higher speed, and a higher effect of inertia load. This time there are deviations in trajectories, with higher values; less than 10 μm, which corresponds to approximately 15 fringes. The same reasoning for the deviations of trajectories made in slow speed level tests can also be made here. Finally in the high-speed tests trajectories (shown in Figure 6.63) are more circular than the ones obtained for first two speed levels. This is believed to be because of higher inertia, as the rotational speed has increased resulting in a reduced effect of gravity. There are again deviations in trajectories of successive cycles, which can be explained with reasons given for previous speed levels.

CHAPTER 7

CONCLUSION

- In this thesis, an experimental setup is designed and constructed to measure micron-level clearances inside plain bearings. First, a piston and cylinder assembly used in compressors of refrigerators was selected to be used in experiments. Then, the setup was modified to apply the methodology to journal bearing of the crankshaft of a 5-cylinder diesel engine.

- Surfaces used as targets in interferometric measurements must have a high reflectivity as well as optically smooth finish. Reflectivity of the coated surface of the piston is lower than required. It was observed that using wet-and-dry sandpaper on its surface does not result in an acceptable optically smooth finish. However, polishing the surface of the piston in an industrial workshop resulted in a finish which had acceptable optical reflectivity, but it contained waves which were visible to the naked eye. These waves were high enough to disturb the clearance measured while the piston is making its reciprocating motion inside the cylinder.

- After operations done on the surface of the piston and observations made on the results of the experiments, it was concluded that it requires more sophisticated operations to produce a piston with optical quality surface finish.

- Surface of a piston pin of a reciprocating compressor used for automotive applications was investigated, because its surface contains same features with that of a journal bearing. By examining the data obtained, it was observed that this surface reflects the light, such that it is possible to measure micron-level clearances from it.

- In experimental setup constructed for the journal bearing measurements, the bearing selected to be used in tests is the farthest one from the electric motor which rotates the crankshaft. Electric motor rotates in lower speeds than the actual operation speed of the crankshaft. In the first set of experiments, the lubricant was removed from inside bearing. Reason for this is that the presence of lubricant reduces the visibility, affecting the quality of the optical data. In these tests, from the 4 optical data taken from 4 different points of the bearing, 5 trajectories for the center of the journal are estimated. All these trajectories are consistent with each other.

- When lubricant was added inside bearing, it was observed that initially optical data of successive cycles are not similar to each other, suggesting that when there is lubricant inside bearing, it takes some time for the shaft to follow a steady-state trajectory. Still, it was observed that there were differences in patterns of optical data collected with some minutes apart. This suggests that there is no steady-state condition for the journal while crankshaft rotates, and that it follows a trajectory which varies with time.

- With presence of lubricant inside bearing, optical data are obtained from two points on the bearing, while crankshaft rotates at 3 different speed levels. At each speed level, journal trajectory for 3 successive cycles are estimates. Results suggest that successive cycles follow similar trajectories. This way, the procedure of conversion of the optical data to the clearance curve is validated.

- Generally journal trajectories have a shape of an ellipse, where its vertices are on vertical axis. Comparing the journal trajectories at different speed levels, it was observed that at high speed level, journal trajectories have a more circular shape. This is attributed to the fact that when rotational speed increases, the inertia force of the crankshaft acting on the bearing increases, and it becomes more significant compared to gravity.

- In tests with the lubricant, it was observed that the visibility of the fringes are acceptable, and optical data can be converted to clearance curves. However, in some ranges the visibility drops, which is attributed to a high clearance between probe and journal's surface.

- After several tests, quality of lubricant degrades. This can be seen on the surface of the probe after tests (Figure 7.1). This also affects the quality of the optical data.

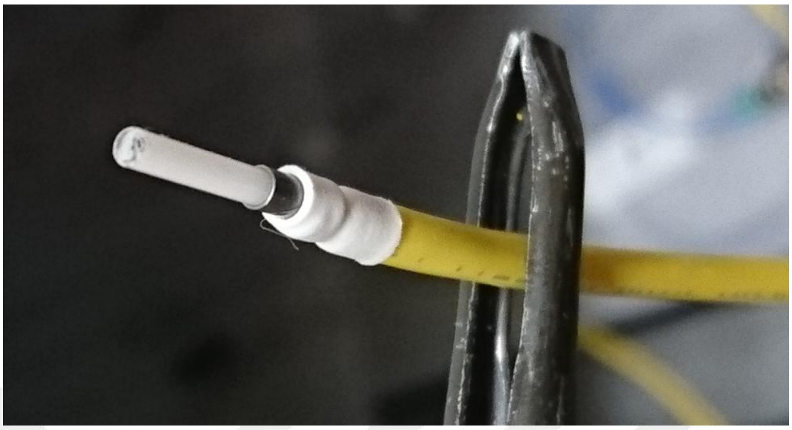

Figure 7.1: *Optic probe after being used in tests (diameter of the probe is 1.7 mm)*

REFERENCES

[1] Taylan Altan. *Sheet metal forming : fundamentals*. ASM International, Materials Park, Ohio, 2012.

[2] Michelson interferometer. `https://en.wikipedia.org/wiki/Michelson_interferometer`. Accessed: October 2017.

[3] Fabry-pérot interferometer interferometer. `ttps://en.wikipedia.org/wiki/Fabry%E2%80%93P%C3%A9rot_interferometer`. Accessed: October 2017.

[4] J Crisp. *Introduction to fiber optics*. Newnes, Amsterdam Boston, 2005.

[5] Fiber optic interferometer fabry-perot. `http://www.proton.rmutphysics.com/news/index.php?option=com_content&task=view&id=1218&Itemid=3`. Accessed: November 2017.

[6] 10 fundamentals of contact between solids. In G W Stachowiak and A W Batchelor, editors, *Engineering TriBology*, volume 24 of *Tribology Series*, pages 527 – 556. Elsevier, 1993.

[7] B Bhushan. *Modern tribology handbook*. CRC Press, Boca Raton, FL, 2001.

[8] Y-C Tan and Z M Ripin. Analysis of piston secondary motion. *Journal of Sound and Vibration*, 332(20):5162 – 5176, 2013.

[9] F L Pedrotti, L M Pedrotti, and S L Pedrotti. *Introduction to optics*. Pearson, 3 edition, 2014.

[10] Acoustic interferometer. `https://www.britannica.com/technology/acoustic-interferometer`. Accessed: October 2017.

[11] A J Lewis. *Absolute length measurement using multiple-wavelength phase-stepping interferometry*. PhD thesis, University of London, Imperial College of Science, Technology and Medicine, 11 1993.

[12] A Franks. Nanometric surface metrology at the national physical laboratory. *Metrologia*, 28(6), 9 1991.

[13] F Zhao. Picometer laser metrology for the space interferometer mission (sim). In *Conference on Lasers and Electro-Optics/International Quantum Electronics Conference and Photonic Applications Systems Technologies*, page CTuO5. Optical Society of America, 2004.

[14] T Shuldt, M Gohlke, H Kögel, R Spannagel, A Peters, and U Johann. Picometre and nanoradian heterodyne interferometry and its application in dilatometry and surface metrology. *Measurement science and technology*, 23(5), 3 2012.

[15] J Lawall and E Kessler. Michelson interferometry with 10 pm accuracy. *Review of Scientific Instruments*, 71(7):2669–2676, 2000.

[16] G de Vine, D S Rabeling, B J J Slagmolen, T T-Y Lam, S C, D M Wuchenich, D E McClelland, and D A Shaddock. Picometer level displacement metrology with digitally enhanced heterodyne interferometry. *Opt. Express*, 17(2):828–837, Jan 2009.

[17] C C Speake and S M Aston. An interferometric sensor for satellite drag-free control. *Classical and Quantum Gravity*, 22(10):S269, 2005.

[18] D T Smith, J R Pratt, and L P Howard. A fiber-optic interferometer with sub-picometer resolution for dc and low-frequency displacement measurement. *Review of Scientific Instruments*, 80(3):035105, 2009.

[19] D M Sykora and M L Holmes. Dynamic measurements using a fizeau interferometer, 2011.

[20] R Schödel, A Walkov, M Zenker, G Bartl, R Meeß, D Hagedorn, C Gaiser, G Thummes, and S Heltzel. A new ultra precision interferometer for absolute length measurements down to cryogenic temperatures. *Measurement Science and Technology*, 23(9):094004, 2012.

[21] B Shirinzadeh, P L Teoh, Y Tian, M M Dalvand, Y Zhong, and H C Liaw. Laser interferometry-based guidance methodology for high precision positioning of mechanisms and robots. *Robotics and Computer-Integrated Manufacturing*, 26(1):74 – 82, 2010.

[22] D Anderson, J Jarzynski, and R F Salant. Condition monitoring of mechanical seals: Detection of film collapse using reflected ultrasonic waves. *Proceedings of the Institution of Mechanical Engineers, Part C: Journal of Mechanical Engineering Science*, 214(9):1187–1194, 2000.

[23] R S Dwyer-Joyce, B W Drinkwater, and C J Donohoe. The measurement of lubricant–film thickness using ultrasound. *Proceedings of the Royal Society of London A: Mathematical, Physical and Engineering Sciences*, 459(2032):957–976, 2003.

[24] R S Dwyer-Joyce, P Harper, J Pritchard, and B W Drinkwater. Oil film measurment in polytetrafluoroethylene-faced thurst pad bearings for hydrogenerator applications. *Proceedings of the Institution of Mechanical Engineers, Part A: Journal of Power and Energy*, 220(6):619–628, 2006.

[25] J Jiao, Q Zhang, B Wu, and C He. Measurement of lubricant film thickness using normal incidence ultrasound. In *2008 IEEE Ultrasonics Symposium*, pages 836–839, Nov 2008.

[26] M Li, M Jing, Z Chen, and H Liu. An improved ultrasonic method for lubricant-film thickness measurement in cylindrical roller bearings under light radial load. *Tribology International*, 78(Supplement C):35 – 40, 2014.

[27] S I El-Sisiand G S A Shawki. Measurement of oil-film thickness between disks by electrical conductivity. *Journal of Basic Engineering*, 82(1):12 – 16, 1960/03/01.

[28] D E Richardson and G L Borman. Using fiber optics and laser fluorescence for measuring thin oil films with application to engines. In *SAE Technical Paper*. SAE International, 10 1991.

[29] O Marklund and L Gustafsson. Interferometry-based measurements of oil-film thickness. *Proceedings of the Institution of Mechanical Engineers, Part J: Journal of Engineering Tribology*, 215(3):243–259, 2001.

[30] S Costantino, O E Martínez, and J R Torga. Wide band interferometry for thickness measurement. *Opt. Express*, 11(8):952–957, Apr 2003.

[31] J M Bennett. Measurement of the rms roughness, autocovariance function and otherstatistical properties of optical surfaces using a feco scanninginterferometer. *Appl. Opt.*, 15(11):2705–2721, Nov 1976.

[32] H Kadono, T Asakura, and N Takai. Roughness and correlation-length determination of rough-surface objects using the speckle contrast. *Applied Physics B*, 44(3):167 – 173, Nov 1987.

[33] C Y Poon and B Bhushan. Comparison of surface roughness measurements by stylus profiler, afm and non-contact optical profiler. *Wear*, 190(1):76 – 88, 1995. Macro and Micro-Tribology and Mechanics of Magnetic Storage Systems.

[34] C Cheng, C Liu, N Zhang, T Jia, R Li, and Z Xu. Absolute measurement of roughness and lateral-correlation length of random surfaces by use of the simplified model of image-speckle contrast. *Appl. Opt.*, 41(20):4148–4156, Jul 2002.

[35] V V Alexander, M N Islam, F L Terry, H Deng, R B Pittman, and T Valen. Surface roughness measurement of flat and curved machined metal parts using

a near infrared super-continuum laser. *Optical Engineering*, 50:50 – 50 – 12, 2011.

[36] J Ramesh, B C Majumdar, and N S Rao. Thermohydrodynamic analysis of submerged oil journal bearings considering surface roughness effects. *Journal of Tribology*, 119(1):100 – 106, 1997.

[37] T Nagaraju, S C Sharma, and S C Jain. Influence of surface roughness effects on the performance of non-recessed hybrid journal bearings. *Tribology International*, 35(7):467 – 487, 2002.

[38] T Nagaraju, S C Sharma, and S C Jain. Influence of surface roughness on non-newtonian thermohydrostatic performance of a hole-entry hybrid journal bearing. *Journal of Tribology*, 129(3):595 – 602, 2007.

[39] C Sinanoğlu, F Nair, and M B Karamış. Effects of shaft surface texture on journal bearing pressure distribution. *Journal of Materials Processing Technology*, 168(2):344 – 353, 2005.

[40] J F Booker. Dynamically loaded journal bearings: Mobility method of solution.

[41] T M Jaloszynski and L W Evers. Dynamic film measurements in journal bearings using an optical sensor. In *SAE Technical Paper*. SAE International, 02 1997.

[42] H Moreau, P Maspeyrot, A M Chomat-Delalex, D Bonneau, and J Frene. Dynamic behaviour of elastic engine main bearings: Theory and measurements. *Proceedings of the Institution of Mechanical Engineers, Part J: Journal of Engineering Tribology*, 216(4):179–194, 2002.

[43] A Valkonen et al. Oil film pressure in hydrodynamic journal bearings. 2009.

[44] G F Simmons, M Cha, J-O Aidanpää, M J Cervantes, and S Glavatskih. Steady state and dynamic characteristics for guide bearings of a hydro-electric unit. *Proceedings of the Institution of Mechanical Engineers, Part J: Journal of Engineering Tribology*, 228(8):836–848, 2014.

[45] Optical interferometer. `https://www.britannica.com/technology/optical-interferometer`. Accessed: October 2017.

[46] J Hayes. *Fiber optics technician's manual*. Delmar, Cengage Learning, Clifton Park, NY, 2011.

[47] Coax cable. theory and application. `http://www.standard-wire.com/coax_cable_theory_and_application.html`. Accessed: November 2017.

[48] Moving average filters. `http://www.analog.com/media/en/technical-documentation/dsp-book/dsp_book_Ch15.pdf`. Accessed: November 2017.

[49] S Chapra. *Numerical methods for engineers*. McGraw-Hill Higher Education, Boston, 2010.

[50] M Yıldırım. Design and construction of an experimental apparatus for the interferometric measurement of micrometer level clearances. Master's thesis, Mechanical Engineering - METU, 2009.

[51] M Yildirim, T Okutucu-Özyurt, and Z Dursunkaya. A numerical algorithm to determine straightness error, surface roughness, and waviness measured using a fiber optic interferometer. *Optics & Laser Technology*, 85(Supplement C):19 – 29, 2016.

[52] T Thomas. *Rough surfaces*. Imperial College Press, London, 1999.

[53] K L Johnson, J A Greenwood, and S Y Poon. A simple theory of asperity contact in elastohydro-dynamic lubrication. *Wear*, 19(1):91 – 108, 1972.

[54] B Bhushan. Contact mechanics of rough surfaces in tribology: multiple asperity contact. *Tribology Letters*, 4(1):1–35, Jan 1998.

APPENDIX A

SPECIFICATIONS OF EXPERIMENTAL EQUIPMENT

Table A.1: *Specifications of laser source*

Wavelength	1550 nm
Wavelength accuracy	±1550 nm (nominal)
Bandwidth	1.5 nm
Optical power (mW)	0.8 – 1 mW (standard)
Optical power stability	±0.004 dB
Fiber optic cable end	FC/APC
Fiber optic cable type	Single mode
Power source	110/220 V AC 60/50 Hz
Dimensions (W × L × H)	260 × 209 × 90 mm
Operating temperature range (^{o}C)	0 to $+50$ ^{o}C
Storing temperature range (^{o}C)	-40 to $+70$ ^{o}C
Humidity	$<$ 70 %

Table A.2: *Specifications of isolator*

Wavelength	1550 nm
Bandwidth	± 10 nm
Maximum isolation (dB)	45
Minimum isolation (dB)	40
Typical insertion loss (dB)	0.5
Maximum insertion loss (dB)	0.6
Return loss (dB)	55
Fiber type	Single mode
Operating temperature range (^{o}C)	0 to $+70\ ^{o}C$
Storing temperature range (^{o}C)	-40 to $+85\ ^{o}C$

Table A.3: *Specifications of beam splitter*

Wavelength	1550 nm
Bandwidth	± 10 nm
Maximum isolation (dB)	45
Minimum isolation (dB)	40
Typical insertion loss (dB)	0.5
Maximum insertion loss (dB)	0.6
Return loss (dB)	55
Fiber type	Single mode
Operating temperature range (^{o}C)	0 to $+70\ ^{o}C$
Split ratio	1×4
Storing temperature range (^{o}C)	-40 to $+85\ ^{o}C$

Table A.4: *Specifications of circulator*

Wavelength	1550 nm
Extinction ratio (dB)	30
Insertion loss, forward direction (dB)	60
Insertion loss, reverse direction (dB)	60
Peak isolation (dB)	30
Power handling (mW)	250
Return loss (dB)	60
Fiber type	Single mode

Table A.5: *Specifications of fiber optic cable*

Wavelength	1550 nm
Bandwidth	±50 nm
Length	1 m
Outer diameter	1.8 mm PVC
Inner diameter	$9/125$ μm
Fiber type	Single mode
Fiber ends	FC/APC

Table A.6: *Specifications of fiber photodetector*

Detector	Ge PIN
Active area	$\varnothing$ 5 mm (19.6 mm^2)
Surface depth	5.1 mm
Wavelength range	800-1800 nm
Peak wavelength (λ_p)	1550 nm
Peak response	0.85 A/W at λ_p
Output voltage	0-10 V
Output impedance	50 Ω
Maximum output current	100 mA
Load impedance	50 Ω
Gain range	70 dB
Gain steps	8 × 10 dB
Gain switch	8 pos rotary
On/off button	Slide
Output	BNC
Optical head size	70.1 × 52.8 × 21.1 mm
Weight	0.15 kg

Table A.7: *Specifications of crankshaft*

Clearance of main bearings (1, 2, 3, 5, 6)	28–72 μm + swell
Clearance of thrust bearing (4)	32–76 μm + swell
Swell	5–10 μm

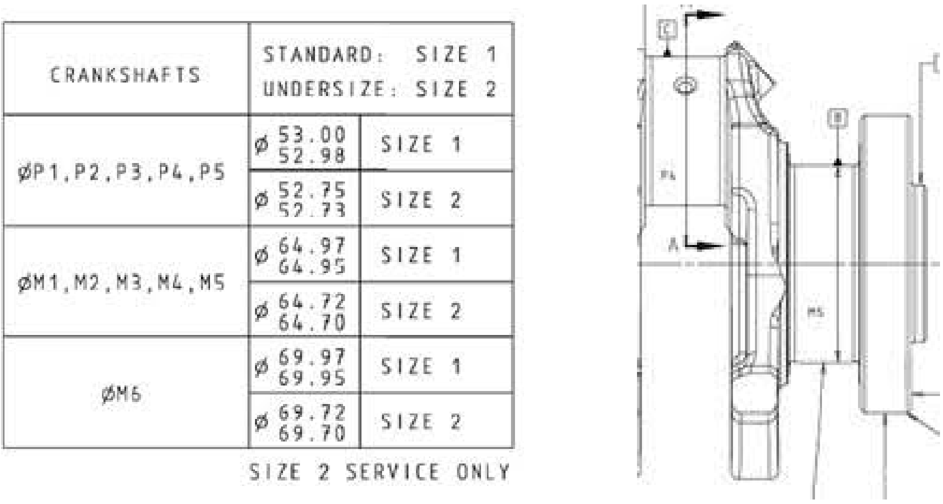

CRANKSHAFTS	STANDARD: SIZE 1 UNDERSIZE: SIZE 2	
ØP1,P2,P3,P4,P5	Ø 53.00 52.98	SIZE 1
	Ø 52.75 52.73	SIZE 2
ØM1,M2,M3,M4,M5	Ø 64.97 64.95	SIZE 1
	Ø 64.72 64.70	SIZE 2
ØM6	Ø 69.97 69.95	SIZE 1
	Ø 69.72 69.70	SIZE 2

SIZE 2 SERVICE ONLY

Figure A.1: *Diameters of the main bearing shafts and crankpins*

Table A.8: *Specifications of electric motor*

Type	Miksan 56 4B
Rated output (kW)	0.09
Voltage (V)	220/380
Connection	Δ/Y
Speed (rpm)	1390
Current (A)	0.06/0.35
Power factor ($\cos\phi$)	0.62
Current ratio (ls/ln)	3
Weight appx. (kg)	2.6

Table A.9: *Specifications of motor driver*

Type	ESKON ES400-007 C
Input voltage (V)	380-480 VAC $(+\%10/-\%20)$
Input current	10A
Output power	3kW
Input/output phase	3/3
Output current	6.8A
Output power	4HP
Operating temperature	0 40^oC

__Table A.10:__ Specifications of NI USB-4431 DAQ device

Analog input	
Input channels	4
Input connector	1 BNC per channel
PC communication	USB 2.0
Power consumption	2.5 W max
ADC resolution	24 bits
ADC type	Delta-sigma
Sampling mode	Simultaneous
Sample rates range	1 kS/s to 102.4 kS/s
Sample rates resolution	$\leq$ 2.10 mS/s
Internal frequency timebase accuracy	$\pm$100 ppm max
Input range	$\pm 10\ \mathrm{V_{pk}}$
FIFO buffer size	1,023 samples (shared between all channels)
Input coupling	AC or DC, each channel independently software selectable
Analog output	
Output channels	1
AO signal connection	BNC
AO frequency range	DC to 43.5 kHz
Internal frequency timebase accuracy	$\pm$100 ppm max
DAC resolution	24 bits
DAC type	Delta-sigma
Output signal range	$\pm 3.5\ \mathrm{V_{pk}}$
Output coupling	DC
Short circuit protection	Indefinite
Minimum working load	1 kΩ
Output impedance	50 Ω
DAC filter delay	63.3 samples max
FIFO buffer size	4,095 samples

Table A.11: *Specifications of NI BNC-2110 data acquisition connector block*

15 BNC connectors for analog input, analog output, trigger/counter functions, and user-defined signals
A spring terminal block with 30 pins for digital and timing I/O signal connections
A 68-pin I/O connector that connects to multifunction DAQ devices
Can be used on a desktop or mounted on a DIN rail

Table A.12: *Specifications of NI SHC68-68-EPM shielded data acquisition cable*

Terminated with VHDCI 68-pin male connector in one end, and 68-pin female 0.050 D-type connector in other end
Connects 68-pin X Series and M Series devices to 68-pin accessories
Features individually shielded analog twisted pairs for reduced crosstalk with high-speed boards

***Table A.13:** Specifications of NI 6321 data acquisition device*

Analog input	
Input channels	8 differential or 16 single ended
Sample rate (single channel maximum)	250 kS/s
Sample rate (multichannel maximum)	250 kS/s
Sample rate (minimum)	No minimum
Timing resolution	10 ns
Timing accuracy	50 ppm of sample rate
Input coupling	DC
Input range	±0.2 V, ±1 V, ±5 V, ±10 V
Maximum working voltage for analog inputs (signal + common mode)	±11 V of AI GND
Input bias current	±100 pA
Input FIFO size	$4,095$ samples
Scan list memory	$4,095$ entries
Analog output	
Output channels	2
Maximum update rate (1 channel)	900 kS/s
Maximum update rate (2 channels)	840 kS/s per channel
Timing resolution	10 ns
Timing accuracy	50 ppm of sample rate
Input coupling	DC
Output range	±10 V
Output current drive	±5 mA
Power-on state	±20mV
Power-on/off glitch	2 V for 500 ms
Settling time, full-scale step, 15 ppm (1 LSB)	6 μs

Table A.14: *Specifications of desktop computer*

Intel Q8200 3 GHz
250 GB HDD 720 rpm
4 GB DDR2 Ram Toshiba Intel® Centrino® Processor Technology
22" LCD Screen

Table A.15: *Specifications of laptop computer*

Brand and model	Lenovo® ThinkPad E470
Processor	Intel® Core™ i5-7200U
Operating system	ubuntu 16.04 LTS
Graphics	Intel® HD Graphics 620
Memory	8 GB DDR4
Storage	500 GB 2.5" SSD

APPENDIX B

MEASURABILITY LIMITS

This report explains the limitations in measurability of the apparatus which models the cylindrical surface of plain bearing as a Cartesian surface. This mechanism was designed and constructed as a Master's thesis finished in year 2009 by Murat Yıldırım supervised by Prof. Dr. Dursunkaya. For further information on how this mechanism works refer to [50]. Mechanical stage of this experimental setup considered in this report is different, but since the optical stage is the same, then some limitations on measurability defined here applies on the current experimental setup as well. Therefore results of this report helps in understanding the limitations in roughness of the target surface.

Physical limitations of the interferometer result in limitations in measurability. Major sources of these limitations are:

- Width of the optic probe: When the wavelength of the asperities are shorter than width of the optic probe, then distinction of every one of them is not possible, and probe takes a moving average of heights of asperities. The distribution of asperities on the surface also affects the quality of optical data. So that some criteria for the surface parameters must be met in order to be able to extract and interpret the fringes of the optical data.

- Motion of the stepper motor: Motor divides a full rotation into a number of steps, and while taking these steps it moves in a discrete manner. As a result shaft, coupling, lead screw mechanism connected to the coupling, and all other components behave as a mass-spring-damper system, and in every step a vibration is created in the system. These vibrations are transferred to the third plate which holds the optic probe. This phenomenon has a direct effect on the quality of the optical data.

Consequently two types of limitations on the measurability can be defined:

(i) Surface topography: Distribution of asperities must be such that probe can acquire meaningful optical data from the surface,

(ii) Minimum clearance: The vertical displacement of the probe with respect to the surface during the experiment must be so that phenomena such as vibration of stepper motor do not affect the quality of the optical data (although their presence cannot be fully removed).

These limitations are addressed in sections 1 and 2.

B.1 Surface topography

Surface roughness, and distribution of asperities on the surface affect the optical data. In fact surface must have certain characteristics, so that the light emitted from the optic probe can be reflected from it and be directed again towards fiber cable, without much loss. Therefore the surface must possess an “optical quality”, and this is directly related to the surface topography. Even if it is possible to emit and accept light from the surface and obtain meaningful optical data, still there are certain limitations on the topography of the surface. There are differences in interference of the light depending whether it strikes to a peak on the surface, or a valley. And effect of these differences are revealed when data are converted to clearance. But due to the reason that will be explained below, it is not possible to fully extract the surface roughness, but only an average of it can be obtained. And this problem can create an obstacle for interpreting the optical data.

The width of optic probe, which light is emitted from it, is 9 μm. As the probe moves on the surface while emitting light, at the same time it accepts light reflected from the surface, and perceives an average interference from a region equal to its own width. Therefore it constantly computes a running average with a width of 9 μm from the surface of test specimen. Therefore if there are asperities with wavelengths much shorter than the width of the optic probe, then probe is not able to detect them, they are filtered-out and it also affects the quality of the optical data. This fact imposes a limitation to the range of application of the interferometer. In what follows, the limits (in terms of surface roughness parameters) of measurability of the setup are studied. Based on the specification of the experimental setup, it is possible to set certain limits to the surface parameters of the test specimens. This enables to determine surfaces which are applicable to be used in the experiments.

As mentioned above, surfaces with acceptable quality can be defined using conventional parameters used to describe the surface topography. Two parameters are required to describe height, and spatial distribution of the asperities on a surface [52].

Height parameter: Most commonly used parameter in this case in RMS roughness, R_q, given in Equation B.1.

$$R_q = \sqrt{\frac{1}{L}\int_0^L z(x)^2 dx} \qquad \text{(B.1)}$$

Where $z(x)$ is the distance perpendicular to the plane of the surface from a reference plane, and L is the sample length, as shown in Figure B.1.

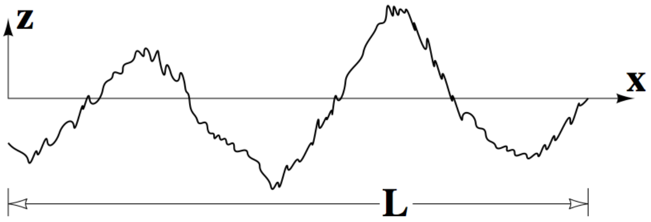

Figure B.1: *$z(x)$ and L[6]*

Spatial parameter: In order to describe how height varies on the surface profile the parameter called “correlation length” is used. Correlation length is the outcome of the autocorrelation function (ACF). ACF is a tool that is used to recognize patterns in a signal. It computes the correlation of a point with other points close to it and is very sensitive to periodic components of the surface and will detect these even when they are disturbed by random processes [52]. A positive ACF value means that there is a positive correlation between two points, zero means there is no correlation, and negative value means there is negative correlation. ACF is the normalized form of Autocovariance function (ACVF), given in Equation B.2. ACF is given in Equation B.3.

$$R(\tau) = \frac{1}{L-\tau}\int_0^{L-\tau} z(x)z(x+\tau)dx \tag{B.2}$$

$$p(\tau) = \frac{R(\tau)}{R(0)} \tag{B.3}$$

Where $z(x)$ and $z(x+\tau)$ are two height values separated by a delay τ, as visualized in Figure B.2. In Equation B.3, $R(0)$ is R_q^2 variance of height distribution.

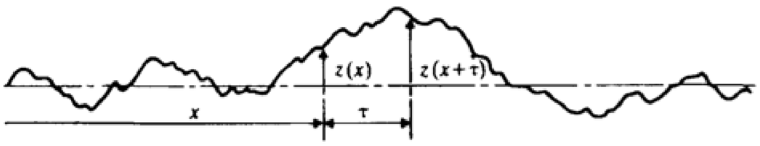

Figure B.2: *Constructing autocovariance and autocorrelation functions [7]*

Correlation length is the distance over which value of ACF decays to some fraction of its initial value (e.g., a tenth, or $1/e$). In this study this fraction is so small that it can be assumed that correlation length is distance at which value of ACF is zero. Two points which are far from each other by a distance larger than correlation length are statistically independent. In [53] it is pointed out that correlation length is a measure of the effective wavelength of the main surface texture. In this text, to follow the notation used in some literature, ([53], [33], and [54]) correlation length is defined with symbol β^*.

Therefore it can be said that a surface with shorter correlation length compared to another surface, will contain higher frequency (i.e. shorter wavelength) asperities.

Thus there exists a minimum value for correlation length which defines the limit of measurability of the experiments. Surfaces having correlation lengths longer than that minimum value can be used in the experiments. It is possible to determine this minimum correlation length with computer simulation. For this purpose a model of rough surface is required.

In order to model a rough surface, a synthetic signal is created in MATLAB. This signal is created by superposition of 28 sine waves with different frequencies, in order to simulate a rough surface. Amplitude and frequencies of these sine waves are tabulated in Table B.1. Note that RMS value of this signal is 0.011.

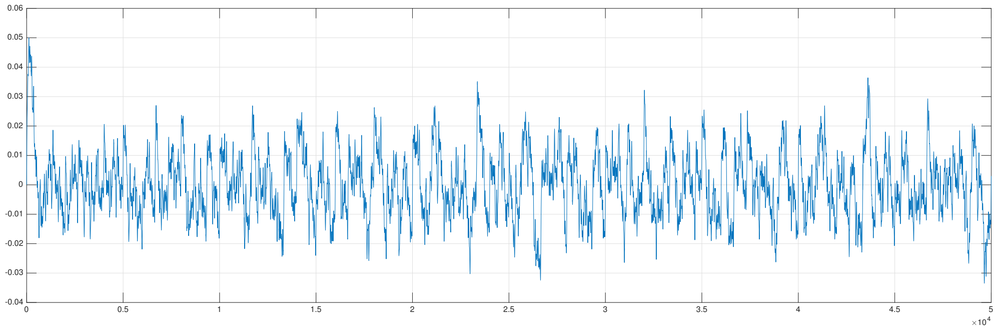

Figure B.3: *Synthetic surface profile*

During the experiments sampling rate is 10^4 samples/second. Synthetic rough surface is also created based on this sampling rate. This model simulates only one turn of the stepper motor, which its duration is 5 seconds. Therefore there are 5×10^4 samples in this signal. Also one turn of stepper motor is equal to 900 μm horizontal movement of the optic probe on the surface. Second column in Table B.1 refers to the wavelength of the sine waves in x-domain, which its range is 900 μm. And third column is about the frequency of these waves in time-domain. There is a linear relation between x-domain and time-domain, which is shown in Equation B.4.

$$x[\mu\text{m}] = \frac{900}{5} t[\text{sec}] \tag{B.4}$$

If sampling rate is changed in future experiments, then this equation will have to be

Table B.1: *List of sine waves used in constructing the synthetic surface*

Amplitude	Wavelength (μm)	Time-domain frequency (Hz)
0.05	60.000	3.0000
0.05	41.000	4.3902
0.05	35.000	5.1429
0.05	27.000	6.6667
0.05	23.000	7.8261
0.05	22.000	8.1818
0.05	21.000	8.5714
0.05	20.000	9.0000
0.05	19.000	9.4737
0.05	18.000	10.0000
0.05	17.000	10.5882
0.05	16.000	11.2500
0.05	15.000	12.0000
0.05	14.000	12.8571
0.05	13.000	13.8462
0.05	12.000	15.0000
0.05	11.000	16.3636
0.05	10.000	18.0000
0.05	9.0000	20.0000
0.05	8.0000	22.5000
0.05	7.0000	25.7143
0.05	6.0000	30.0000
0.05	5.0000	36.0000
0.05	4.0000	45.0000
0.05	3.0000	60.0000
0.05	2.0000	90.0000
0.05	1.5000	120.0000
0.05	0.9000	200.0000

updated accordingly. Computing the running average of this signal with a width of 9 μm will require a window size of 500 data points of the signal. Because according to Equation B.4 a distance of 9 μm corresponds to 0.05 seconds, and since sampling rate is 10^4 samples/second, this amount is equal to 500 samples in time-domain. The surface itself and its 9μm-running-average are shown in Figure B.4.

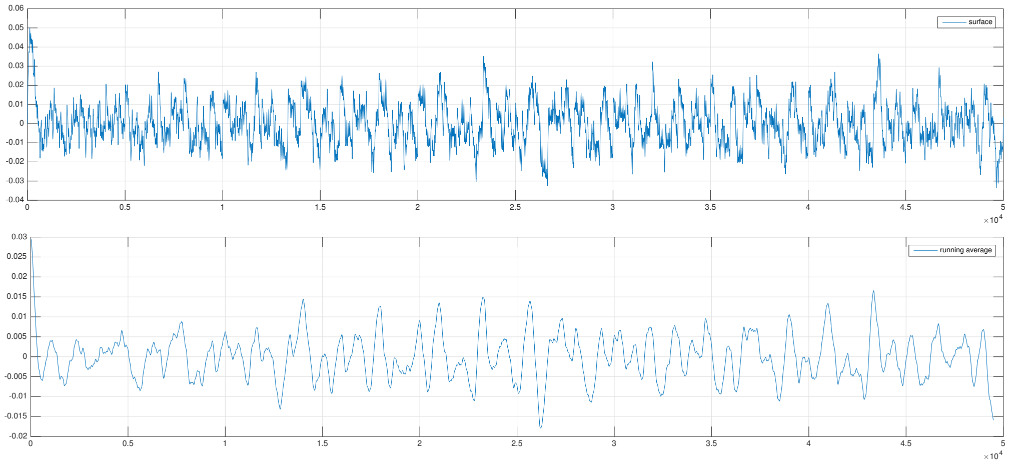

Figure B.4: *Synthetic surface and its running average*

In order to observe the frequencies lost during averaging, frequency spectra of the two signals are shown in Figure B.5.

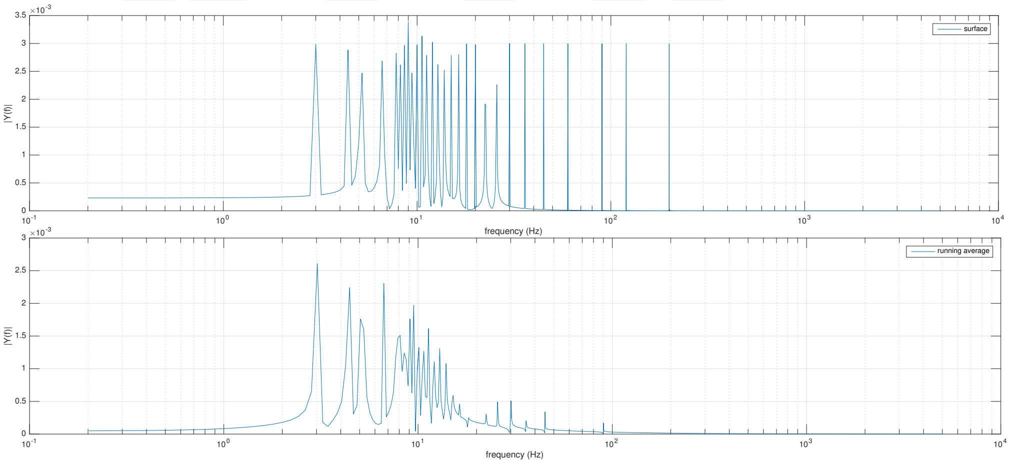

Figure B.5: *Frequency spectra of synthetic surface and its running average*

Note that frequency spectrum given in Figure B.5 is in time-domain. As from frequency of 10 Hz, amplitudes of the sine waves start to decrease, so that after 20 Hz waves are totally filtered-out. If converted to x-domain, from a wavelength of 18 μm amplitudes of waves start to decrease, and wavelengths lower than 9 μm are totally filtered-out. Higher wavelengths however are preserved. This simulation shows that if surface contains asperities with a wavelength lower than 18 μm, then the optic probe will not be able to catch the whole surface roughness information.

By taking a look at the frequency spectrum of the signal extracted from optical data of an actual experiment, the validity of results inferred from simulation shown above can be checked. The signal shown in Figure B.6 is the residual signal of the clearance data. It is obtained by subtracting the linear-fit, periodic trends due to stepper motor, and surface waviness from the clearance signal.

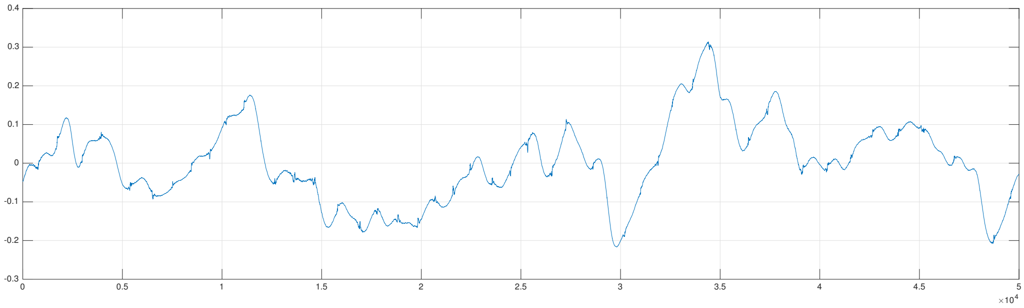

Figure B.6: *900 μm region from surface of a actual test specimen*

Frequency spectrum of this signal is shown in Figure B.7.

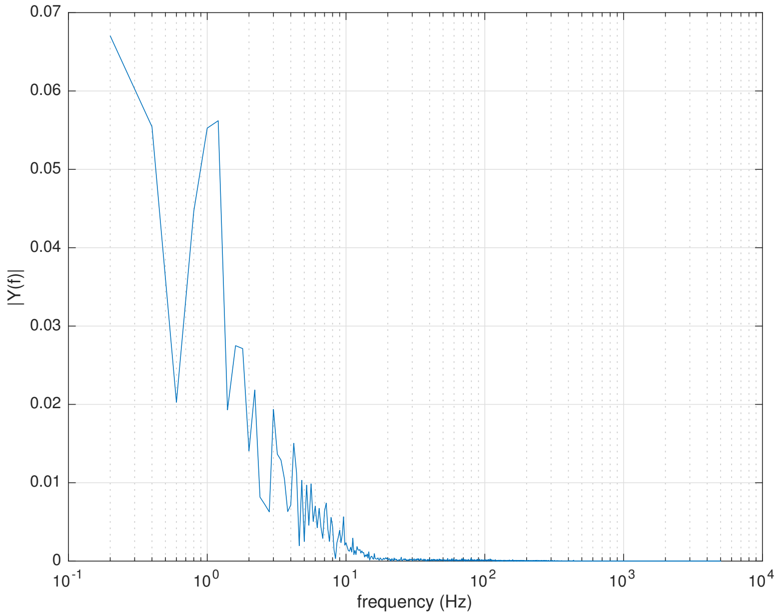

Figure B.7: *Frequency spectrum of 900 μm region from surface of a actual test specimen*

It can be seen in Figure B.7, as frequency increases amplitudes decrease so that there are no frequencies higher than 10 Hz. This might be either from nature of the surface, or that optic probe has filtered out the high-frequency asperities. This is in accordance with the simulation results.

Therefore the limit which asperities having a wavelength shorter than that create problems in the optical data is 18 μm. This minimum limit can also be defined in terms of correlation length.

It can be shown that ACF of a signal composed of a sine wave is a cosine wave, with the same frequency as sine wave. Therefore correlation length, at which the value of cosine wave is zero is the quarter of the wavelength of the sine wave, $\lambda/4$, λ being the wavelength. If a signal is not composed of just one sine wave, but of several sine waves with different frequencies (as it is the case for the model of rough surface defined above), then ACF of this signal can be constructed using Equation B.5.

$$R = \frac{\sum_{i=1}^{n} A_i^2 \cos(2\pi f_i t)}{\sum_{i=1}^{n} A_i^2} \tag{B.5}$$

Where A_i and f_i are the amplitude frequency of i^{th} sine wave, respectively.

Wavelengths of the sine waves in the signal have a direct relation with the correlation length of the signal. Therefore knowing that the minimum possible wavelength is 18 μm, the minimum correlation length is quarter of this value, that is 4.5 μm. In other words, surfaces that will be used in experiments must have a correlation length longer than 4.5 μm. By analyzing Equation B.5 it can be said that asperities (sine waves in model) with lower wavelength will tend to shorten the correlation length, while those with longer wavelength will tend to extend it.

This study clearly defines limits on the spatial distribution of asperities on the surfaces that are to be used in the experiments. Test specimens which their surface topography satisfy the imposed limitation can be used in the experiments. It is possible to collect meaningful optical data from their surface. Therefore the surface topography information of the test specimen must be known before-hand, in order to verify that its surface is within the measurability limits of the setup.

B.2 Minimum clearance

In the setup used for experiments, it is theoretically possible to detect relative clearance changes which are as low as half the wavelength of light coming out of laser. And since wavelength of the light emitting from laser source is 1550 nm, therefore it means a clearance change of 0.78 μm is possible to be measured. But in practice there are many factors which limit the performance of the setup.

In ideal case it is expected the optical data to be a pure sinusoidal wave (i.e., fringes) which when converted to distance data it forms a straight line, with time (or number of samples) as its x-axis and distance as the y-axis. However as the optic probe emits and receives light from the surface, there are three major sources of disturbance affecting the fringes: surface roughness, surface waviness, and motion of stepper motor. Effect of surface roughness is analyzed in previous section. Surface waviness shows itself as a very low frequency disturbance in distance curve, and can be modeled and eliminated with a 9th order polynomial. Effect of stepper motor shows itself as a constant periodic trend. Frequency of this periodic trend is the same as the speed of the stepper motor. In this section, with the knowledge acquired from initial experiments about the significance of effects discussed above, it is tried to estimate the minimum clearance that can be measured with the setup. This can help in determining the area of application of this setup.

For this purpose a parametric model of the clearance curve is constructed, in which all previously-mentioned effects are modeled. Then this curve is converted back to the optical data. With the help of this artificially generated optical data it is possible to monitor the quality of the fringes, and see how they are affected by modifying the parameters. It is known that quality of the optical data primarily can be found out by trying to visually detect and count the number of fringes. Therefore by observing the quality of the optical data, minimum acceptable clearance that can be measured is estimated.

Parameters of this model are listed below

- Straight line to model relative clearance change (slope of this line will determine the total clearance change),
- 9th order polynomial to model surface waviness,
- Periodic trend to model stepper motor,
- Synthetic noise to model surface roughness.

For this model it is assumed that surface of mirror has a length of 9000 μm. Based on the sampling rate of the data acquisition platform (which is 10^4 samples/second), since it takes 50 seconds for the probe to cover this distance (due to constant speed of stepper motor), number of data points in model is 5×10^5.

Below the procedure of constructing a clearance curve is explained. Relative clearance change is selected to be 20 μm. This line is shown in Figure B.8.

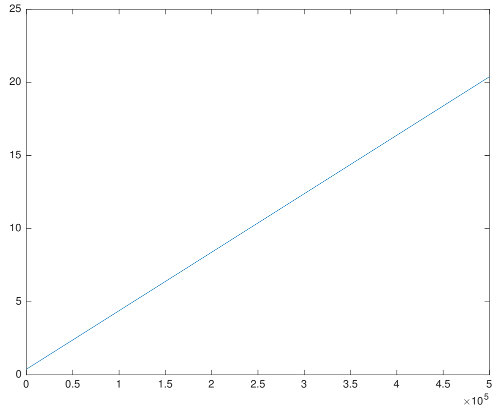

Figure B.8: *Relative clearance change*

Due to surface waviness of test specimen there is always a behavior in clearance curve that can be modeled best as a 9th order polynomial. This polynomial based on actual data is created and added to clearance curve. The created polynomial is shown in Figure B.9 After this addition clearance curve is updated in Figure B.10.

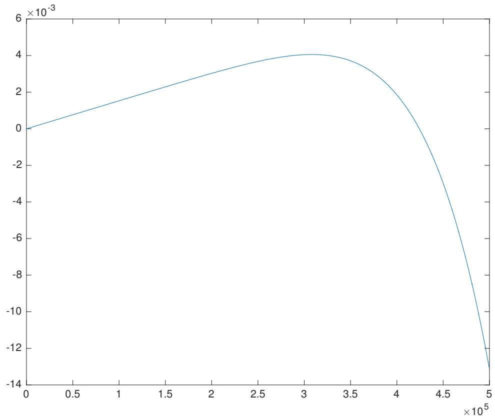

Figure B.9: *9th order polynomial*

As it can be seen in Figure B.10, 9th order polynomial does not cause a visible change in clearance curve. But in order to extract information about surface roughness, it must be detected and eliminated.

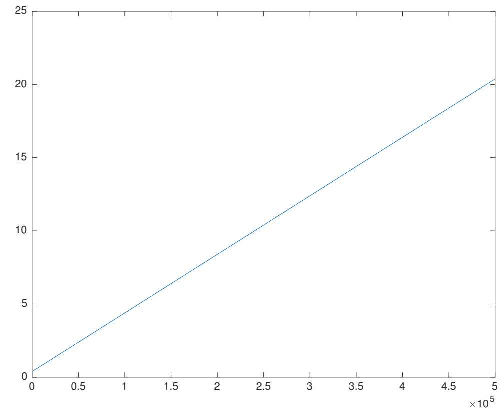

Figure B.10: *Relative clearance change, and 9th order polynomial*

Third parameter is the periodic trend imposed by motion of stepper motor. Frequency of this trend is 0.2 Hz, which is at the same time the turning speed of stepper motor. In this model amplitude of this effect is 0.15 μm. The periodic trend is shown in Figure B.11.

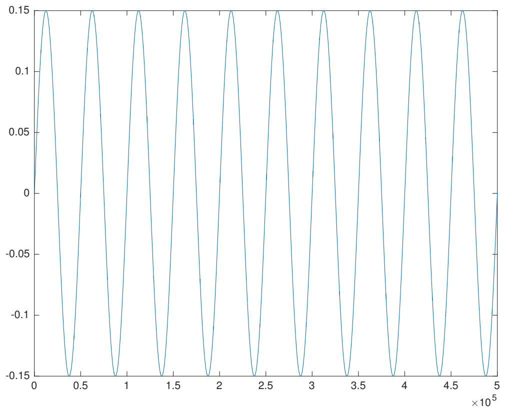

Figure B.11: *Periodic trend due to stepper motor*

After addition of stepper motor effect to the clearance curve, it is shown in Figure

B.12.

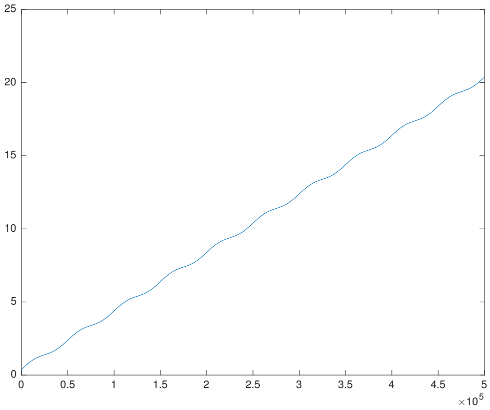

Figure B.12: *Relative clearance change, 9th order polynomial, and periodic trend due to stepper motor*

The final addition to the clearance signal is surface roughness of the test specimen. Constructing surface roughness model is explained in previous section. After addition of this effect to the clearance curve, its final form can be seen in Figure B.13.

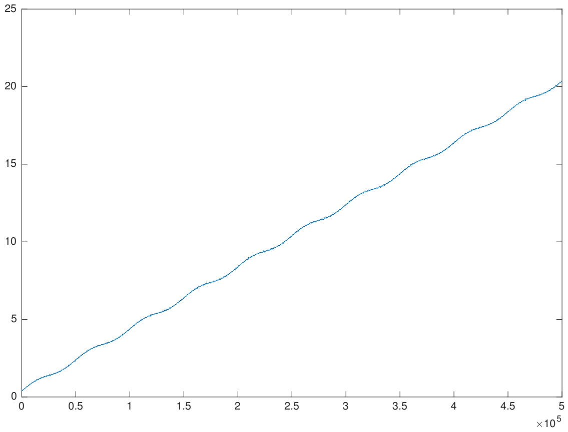

Figure B.13: *Final form of clearance curve*

After creating this synthetic clearance curve, by developing an algorithm it is possible to obtain the corresponding optical data.

Ability to construct and analyze the optical data based on the synthetic clearance creates an important ability. This makes it possible to clearly define limits to the capability of the experimental setup. This way the minimum possible vertical clearance change over a certain horizontal distance that is practically possible to be measured can be specified. And as a consequence the applications that this setup is valid to be used can be determined. Optical data which results in the clearance curve shown in Figure B.13 is shown in Figure B.14.

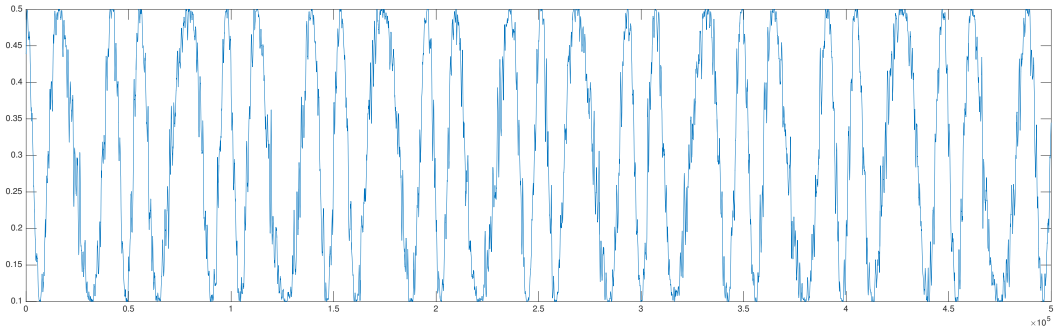

Figure B.14: *Optical data corresponding to clearance curve shown in Figure B.13*

In order to determine the limits for minimum clearance that is possible for the setup to measure, the model explained above is used. It is known that in typical piston-cylinders used in refrigerator compressors distance of one stroke is around 15 mm. It is known that the clearance over a stroke is approximately equal to 10 μm. Therefore over a distance of 9000 μm a clearance of 6 μm is expected to occur. Clearance slope is selected to reflect this prediction.

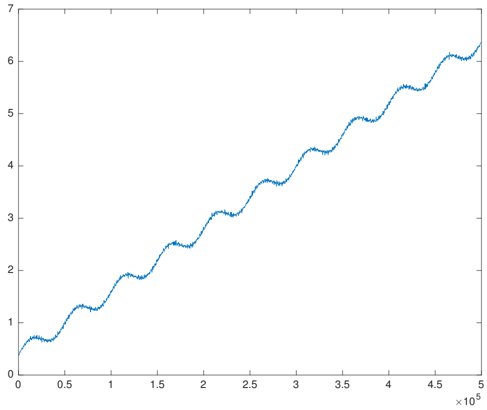

Figure B.15: *Expected clearance curve for a typical piston stroke inside cylinder of a refrigerator compressor, when actuated by stepper motor used in experimental setup*

Note that the clearance curve shown in Figure B.15 does not reflect the variation of clearance between piston and cylinder wall of a typical compressor. It is a simulation of the curve obtained from piston-cylinder mechanism actuated with current experimental setup. It contains all disturbances defined above, which are present in the experimental setup.

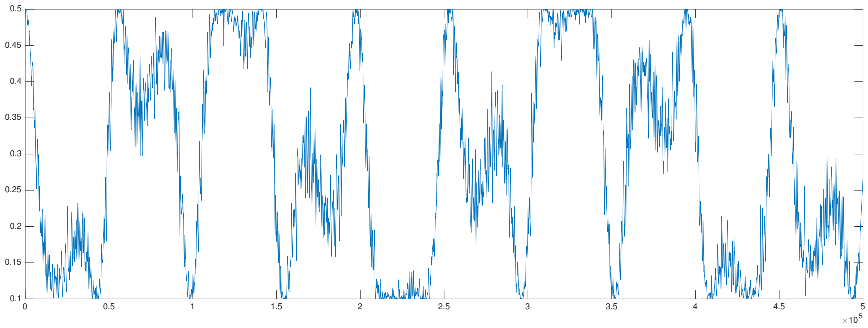

Figure B.16: *Optical data of an expected clearance curve for a typical piston stroke inside cylinder of a refrigerator compressor*

It can be seen in this case that the fringes cannot be detected easily. In order to identify each fringe, the local maxima and minima of the signal must be found. In signal shown in Figure B.16 this is not easy to find the local maxima and minima for some of the fringes. And due to other disturbances during the actual experiment, the collected signal will contain more noises. The distance between optical probe and surface causes some loss in visibility of the fringes, and this results in the effects of other noises to get amplified. Considering all these factors, it can be said that the minimum possible clearance that can experimental setup measure is higher than the typical clearances present in piston-cylinders of the refrigerator compressors. Therefore, for experiments it is necessary to increase the clearance between piston and cylinder such that it is within the limits of measurability.

APPENDIX C

PROFILOMETER DATA OF PISTON PIN

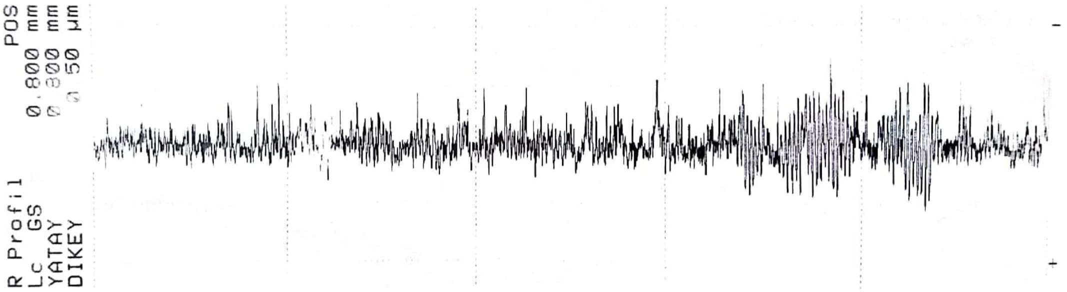

Figure C.1: *Profilometer data of piston pin, horizontal distance is 800 µm, vertical distance is 0.50 µm*